



DALHOUSIE
UNIVERSITY

DALHOUSIE-STRATHCLYDE RESEARCH PROPOSAL

Final Report

Darrel A. Doman, PhD, PEng

December 8, 2015

Revisions:

November 30, 2015

December 5, 2015



PERIOD	FEB-01-2013-OCT-31-2015
PROJECT#	OERA01
REPORT #	OERA01-03



TABLE OF CONTENTS

<i>Table of Contents</i>	<i>I</i>
<i>Executive Summary</i>	<i>II</i>
1 Introduction	1
1.1 Purpose	1
1.2 Scope	1
1.3 Background.....	1
2 Discussion of Objectives, Methodology, and Results.....	2
2.1 Objectives	2
2.2 Methodology	2
2.3 Results	2
3 Dissemination and Technology Transfer.....	3
4 Conclusions & Recommendations.....	5
4.1 Conclusions.....	5
4.2 Recommendations	5
5 Publications.....	6
5.1 Articles published or submitted to refereed journals.....	6
5.2 Conference proceedings and publications.....	6
5.3 Media and invited speaker.....	6
6 Expenditures of OERA Funds	8
7 Employment Summary	9
8 Appendix A–Detailed Report.....	10

EXECUTIVE SUMMARY

The current project centered on the development of tidal energy device (e.g. turbine) technologies that passively control the loadings on the device. As the tidal flow speed increases, the loads on the device increase dramatically requiring very large structures and exotic materials. The motivation for this is the decosting of the devices via lower capital costs and less frequent maintenance, thus making tidal energy a more economically viable technology. The particular area of focus in this work is the control of both the turbine blade pitch (i.e. orientation into the tidal flow) and its high speed behavior. Traditionally, control is achieved through very expensive electrical motors within the turbine itself leading to frequent maintenance needs. The approach investigated here is the use of bend-twist blades which passively pitch and bend away from the flow as a result of their unique manufacturing design of the composite materials.

The current challenge is in the engineering of the bend-twist blade design, which is very complex and requires the coupling of the structural and hydrodynamic (i.e. tidal flow) loadings on the blade. To address this technology gap, a computational tool was developed that accounts for the structural strength as well as the hydrodynamic performance of a particular blade design. By coupling this novel design tool with a custom optimization software, a fully-feature design tool has been developed. The tool was validated by testing scale metal and composite blades in the tow tank at Strathclyde University.

Another facet of this project was to establish a technology and knowledge transfer between Dalhousie and Strathclyde. This has been accomplished, starting with signing a tidal energy research MOU, a bilateral doctoral student research exchange, and collaborative research work. This collaboration has produced three refereed journal publications, eight conference papers, and fostered the initiation of an international tidal energy research network which includes Strathclyde, Dalhousie, and Cardiff University.

1 INTRODUCTION

1.1 PURPOSE

This document constitutes the interim report for the Dalhousie–Strathclyde Research Proposal OEAR-funded project. This report builds upon the first interim report submitted for the time period covering February 1, 2013–October 31, 2015. The scientific objectives and purpose remain the same and the reader is referred to that report for details. The present document provides an overall picture of the description of progress, technology transfer, publications, funding, expenditures, and employment summary. Detailed scientific results and information may be found in the attached report entitled “Design tool for passively adaptive tidal turbine blades” in Appendix A.

1.2 SCOPE

The scope of the work includes analytical analyses, computer simulation, and experimentation testing. This document will report on all research methodologies and results as well as making some summarizing remarks and recommendations on future directions of research.

1.3 BACKGROUND

The objectives of the Dalhousie–Strathclyde collaborative project are to investigate two technologies which use fixed-pitch blades for passive feather power regulation (power regulation without the addition of mechanically complex moving parts), which requires the implementation of turbine blades specifically designed to enable “feathering” as flow speeds increase beyond the site design flow speed. As a blade feathers in relation to the tidal flow, its power capture efficiency reduces, regulating the peak level of power that the generator has to absorb. Compared to the complexity, capital expense, and potentially high maintenance costs associated with variable pitch mechanisms, fixed-pitch passive feather regulation requires no moving parts and is less structurally vulnerable at the blade root, potentially resulting in increased robustness and reduced maintenance. Each of these improvements could drive down the capital and operational costs of energy captured from the tide. The Dalhousie research team is focused on composite bend-twist blade technologies which passively regulate power in high-velocity tidal sites whilst the Strathclyde team is developing rotor overrunning techniques which are suitable for low-velocity tidal sites. The combination of both of these state-of-the-art research projects is a complete passive power control system for a tidal turbine.

2 DISCUSSION OF OBJECTIVES, METHODOLOGY, AND RESULTS

2.1 OBJECTIVES

The proposed work aims to meet several objectives:

- 1) Develop advanced tidal device technologies to specifically lower operational and initial device costs.
- 2) Initiate, foster, and facilitate international marine renewable energy research collaborations between the University of Strathclyde and Dalhousie University.
- 3) Implement a bilateral student exchange research program.

2.2 METHODOLOGY

In order to meet the above objectives, a series of technology and knowledge transfer activities were carried in a bilateral fashion with Strathclyde University. Specifically, computational design tools were developed and validated by extensive experimental testing carried out over the course of the project. Detailed methodologies, equipment, and infrastructure used for these design tools and experiments can be found in the detailed scientific report in Appendix A.

2.3 RESULTS

Key results obtained as a result of this work are:

- Bend-twist composite blades were manufactured at a testing scale for the first time in Canada.
- A computational design tool for bend-twist blades has been developed. The tool couples structural and hydrodynamic effects and estimates the strength of blade designs, thus enabling effective engineering of custom blades.
- Significant tow tank testing has been undertaken to accumulate a data set with which the computational design tool can be validated. Final testing will take place in January 2016 at Strathclyde University.
- It has been shown that bend-twist blades have the potential to limit power (i.e. thrust loadings) on tidal energy devices.

Refer to the Appendix A for detailed discussion of the results.

3 DISSEMINATION AND TECHNOLOGY TRANSFER

Table 1: List of activities where the research project has been disseminated are research knowledge transferred.

ACTIVITY	DATE	DESCRIPTION	ATTENDEES	OUTCOMES
MOU signing	Jul-05-2013	Dalhousie and Strathclyde sign MOU on marine renewable energy reseach	Ms. R.E. Murray Dr. D.A. Doman Dr. M.J. Pegg Ms. C. Gracie Mr. C. Johnstone DoE OERA	The first MOU of its kind in North America is signed setting the platform for the research project.
Student exchange	Aug-15-2013– Dec-15-2013	Ms. R.E. Murray will visit Strathclyde	Ms. R.E. Murray	Perform experiments in the tow tank. Visit Airborne Composites manufacturing facility. Develop blade design tools in conjunction with Ms. C. Gracie.
EWTEC 2013	Sep-02-2013– Sep-05-2013	10th European Wave and Tidal Energy Conference Series in Aalborg, Denmark	Ms. R.E. Murray Dr. D.A. Doman Dr. M.J. Pegg Ms. C. Gracie Mr. C. Johnstone	Strengthened a research collaboration with Airborne Composites. Hold progress meeting with Strathclyde team. Two very well-received conference papers presented.
Visit to Airborne	Sep-08-2013	Ms. R.E. Murray visited tidal blade manufacturing facility	Ms. R.E. Murray	Strengthened a research collaboration with Airborne Composites. Gained valuable insight into actual manufacturing challenges and constraints that will drive more practical, industrially-focused technology development.
British Pop-up Consulate	Mar-04-2014– Mar-07-2014	The British High Commission, UK Trade & Investment, British Council, and Scottish Development International trade mission to Halifax, Nova Scotia	Ms. R.E. Murray Dr. D.A. Doman Dr. M.J. Pegg Ms. C. Gracie Mr. C. Johnstone	Ms. R.E. Murray and Ms. K. Gracie gave a joint presentation of their research projects. Significant exposure to the research collaboration was achieved.
Nova Scotia Energy Research & Development Conference 2014	May-21-2014– May-22-2014	Joint OERA/DoE research conference in Halifax, Nova Scotia	Ms. R.E. Murray Dr. D.A. Doman Dr. M.J. Pegg Ms. C. Gracie Mr. C. Johnstone	Ms. R.E. Murray and Ms. K. Gracie gave a joint presentation of their research projects. Ms. R.E. Murray won the best poster award in the marine renewables category.
Student exchange	May-01-2014– Aug-31-2014	Ms. K. Gracie will visit Dalhousie	Ms. K. Gracie	Sensitivity study of rotor overrunning controlling parameter. Couple advance blade structural model to BEMT code with Ms. R.E. Murray.

DISSEMINATION AND TECHNOLOGY TRANSFER

ACTIVITY	DATE	DESCRIPTION	ATTENDEES	OUTCOMES
ICOE 2014	Nov-04-2014– Nov-06-2014	International Conference on Ocean Energy 2014	Ms. R.E. Murray Dr. D.A. Doman Dr. M.J. Pegg Ms. C. Gracie Mr. C. Johnstone	Present two conference papers.
EWTEC 2015	Sep-06-2015– Sep-11-2015	10th European Wave and Tidal Energy Conference Series in Nantes, France.	Ms. R.E. Murray Dr. D.A. Doman Dr. M.J. Pegg Ms. C. Gracie Mr. T. Nevalainen Mr. C. Johnstone	Present two conference papers. Solidified an international network of research collaborators including Strathclyde University, Cardiff University, and Dalhousie University.
Invited speaker	Oct-15-2015	Ms. R.E. Murray gave a talk on her doctoral research at the Annual Killam Celebration	Ms. R.E. Murray	Increasing profile of tidal energy research in Nova Scotia
Collaborative tow tank testing	Jan-13-2016– Jan-20-2016	Testing of 3 different blade designs, including composite bend-twist blades from Airborne Composites, and 2 metal blades manufactured by Dalhousie using a Cardiff university turbine at the Strathclyde tow tank	Ms. R.E. Murray Ms. K. Gracie Mr. T. Nevalainen Mr. C. Johnstone Dr. T. O’Doherty	The entire dataset will be collaboratively used to validate design tools and disseminated in an international journal.

4 CONCLUSIONS & RECOMMENDATIONS

4.1 CONCLUSIONS

The purpose of this continued research was to determine the applicability of bend-twist tidal turbine blades to the industry. This work has demonstrated the sensitivity of composite computational models to manufacturing effects such as ply angles and thicknesses. Through structural testing of bend-twist blades, it was shown that for thin laminates, the computational model requires a high level of accuracy for the thickness as well as the ply angles. At this point, smaller scale blades with thin ply layers are being used to demonstrate and prove the bend-twist concept. Therefore, at this stage of the research the thickness and ply angles need to be accurately known. However, for larger-scale blades the relative effect of thickness will become less important.

The iterative computational design tool was shown to be effective in predicting the deformation and performance of a bend-twist blade in a short computational time, making it useful for early stage design engineering where many design iterations are trialled. Based on a case study for a full scale turbine with bend-twist blades, it was found that designing a bend-twist blade with a pre-deformed geometry allows the turbine to operate optimally at design conditions, while reducing structural loads and power capture at flow speeds above design conditions. As well, a pre-deformed blade increases the overall power capture of the turbine between the cut-in flow speed and the design flow speed, increasing the overall annual energy capture. This increase in power within these flow conditions, as well as the decrease in structural loads, has significant effects on the overall cost of the turbine. For example, with lower peak power and thrust loads at extreme conditions, smaller, less expensive generators and support structures will be sufficient. As well, for existing turbine systems, bend-twist blades can be lengthened without altering or increasing the existing support structure size, resulting in increased power capture.

4.2 RECOMMENDATIONS

The current project is viewed to have accomplished all of its research objectives and based on the feedback from international collaborators and industry alike, the following recommendations can be made for the next steps of the research programme.

- 1) A research project should be undertaken to investigate the performance bend-twist blades at medium scales (~1 m). Results from this will facilitate the critical investigations into the on-going issue of understanding how tidal turbine blades are scaled from small (< 1 m) to full (> 3 m) scales.
- 2) A structural testing project should be undertaken to develop the infrastructure and knowledge to assess a large and full scale blade's strength and operational life. Building off of the research successes of the current project, it is felt that Dalhousie is ideally suited to develop this capability. **This is expertise that is current lacking in Nova Scotia and would have significant research and commercial benefits.**
- 3) **Nova Scotia should develop and train a tidal energy champion for the future.** It is suggested that a bilateral leadership collaboration between Strathclyde and Dalhousie be supported which would see Mr. C. Johnstone become a Visiting Professor at Dalhousie and Drs. D.A. Doman and M.J. Pegg similarly appointed at Strathclyde. This will complete the technology and knowledge transfer started with the MOU signed as part of this project. It will also ultimately allow the leadership team to train a Nova Scotia-based researcher to lead tidal energy efforts in the province.

5 PUBLICATIONS

5.1 ARTICLES PUBLISHED OR SUBMITTED TO REFEREED JOURNALS

- [1] Doman, D.A., Murray, R.E., Pegg, M.J., Gracie, K., Johnstone, C.M., and Nevalainen, T. (2015) Tow-tank testing of a 1/20th scale horizontal axis tidal turbine with uncertainty analysis. *International Journal of Marine Energy*. 11: 105-119
- [2] Murray, R.E., Doman, D.A., Pegg, M.J. (2015) Finite element modeling and effects of material uncertainties in a composite laminate with bend-twist coupling. *Composite Structures*. 121: 362-276
- [3] Murray, R.E., Nevalainen, T., Gracie, K., Doman, D.A., Pegg, M.J., and Johnstone, C.M. (2015) Passively Adaptive Tidal Turbine Blades: Structural Blade Testing and Design Tool Development. *International Journal of Marine Energy*. Submitted Sept 2015. Ref. No.: IJOME-D-15-00064

5.2 CONFERENCE PROCEEDINGS AND PUBLICATIONS

★ Oral Presentation at International Conference

- [4] Murray, R.E.★, Nevalainen, T., Gracie, K., Doman, D.A., Pegg, M.J., and Johnstone, C.M. (2015) Design Tool for Passively Adaptive Tidal Turbine Blades. *European Wave and Tidal Energy Conference*, Nantes, France.
- [5] Murray, R.E.★, Gracie, K., Doman, D.A., Pegg, M.J., and Johnstone, C.M. (2014) Design of passively adaptive rotor blades for horizontal-axis tidal turbines. *International Conference on Ocean Energy*, Nova Scotia, Canada.
- [6] Gracie, K.★, Nevalainen, T., Johnstone, C.M., Murray, R.E., Doman, D.A., and Pegg, M.J. (2015) Development of a blade design methodology for overspeed power-regulated tidal turbines. *European Wave and Tidal Energy Conference*, Nantes, France.
- [7] Nevalainen, T.★, Johnstone, C. and Grant, A. (2015) Characterizing Unsteady Eccentric Loads on Tidal Stream Turbines Using a Dynamic Blade Element Momentum Theory. *European Wave and Tidal Energy Conference*, Nantes, France.
- [8] Doman, D.A., Murray, R.E., Pegg, M.J., Gracie, K., Johnstone, C.M., and T. Nevalainen (2014) Dynamic testing of a 1/20th scale tidal turbine. *Asian Wave and Tidal Energy Conference*, Tokyo, Japan.
- [9] Murray, R.E.★, Gracie, K., Doman, D.A., Pegg, M.J., and Johnstone, C.M. (2014) Passively Adaptive Rotor Blades for Horizontal-Axis Tidal Turbines: Blade design and baseline performance data. *Offshore Energy Research Association of Nova Scotia, Research and Development Conference*, Halifax, Canada.
- [10] Murray, R.E.★, Gracie, K., Doman, D.A., Pegg, M.J., and Johnstone, C.M. (2013) Design of a passively adaptive rotor blade for optimized performance of a horizontal-axis tidal turbine. *European Wave and Tidal Energy Conference*, Denmark.
- [11] Murray, R.E.★, Pegg, M.J., Murphy, B. (2011) Energy from the Ocean around Nova Scotia: Past, Present and Future. *KoGreen Tech Seminar on Tidal Energy*, South Korea.

5.3 MEDIA AND INVITED SPEAKER

- [12] Dalhousie University Annual Killam Celebration, Invited speaker (October, 2015)
- [13] British High Commission “Pop-Up Consulate” Science Salon & Reception, Guest speaker, March

PUBLICATIONS

4th (2014) Citadel Hill, Halifax

- [14] Invited speaker at the International Conference on Ocean Energy, plenary session hosted by INORE (November 2014)
- [15] American Society for Engineering Education (ASEE) TV promotional Dalhousie University video, shown internationally (2013)
- [16] Article on Robynne Murray's work in tidal energy St. FX Alumni Magazine (2013)
- [17] "Harnessing the tides" article on Robynne Murray's work in tidal energy, Dalhousie Alumni Magazine (2013)
- [18] Invited speaker, OERA R&D Conference

7 EMPLOYMENT SUMMARY

Table 3: Employment summary directly related to the project.

NAME	POSITION	STUDENT?	TYPE	CONTRIBUTIONS	WORK MONTHS
R.E. Murray	Student	PhD	full-time	doctoral research	32
K. Gracie	Student	PhD	full-time	doctoral research	32
M. MacDonald	Technician	No	part-time	machining support	8
A. MacPherson	Technician	No	part-time	machining support	1
I. Finlayson	Engineer	No	part-time	design support	2

8 APPENDIX A–DETAILED REPORT

Design tool for passively adaptive tidal turbine blades

by
Robynne Murray

Department of Mechanical Engineering
Dalhousie University

PO BOX 15000
Halifax, NS
CANADA B3H 4R2

Submitted to **OERA**

Please keep confidential.



**DALHOUSIE
UNIVERSITY**

Inspiring Minds

TABLE OF CONTENTS

List of Figures	II
List of Tables	IV
1 Introduction	1
1.1 Background	2
1.2 Objectives.....	5
2 Structural testing.....	7
2.1 Laminate plates	7
2.2 Turbine blade.....	12
3 Hydrodynamic testing.....	22
4 Structural model	35
4.1 Laminate plate	35
4.2 Composite blade.....	38
5 Hydrodynamic model	46
5.1 Batten and Pinon verification.....	46
5.2 NREL S814 verification.....	48
6 FEM-BEMT Design tool.....	53
6.1 Procedure.....	53
6.2 Stress analysis	55
7 Case study- 4 m blades HATT	57
7.1 Blade element convergence study	57
7.2 Pre-deformed blade geometry	58
7.3 Design of experiment	61
7.4 FEM development	64

7.5	Results	64
8	Conclusions	67
8.1	Future work: Composite and Aluminum blades hydrodynamic testing.....	67
8.2	Acknowledgments	67
	References.....	69

LIST OF FIGURES

Figure 2-1	Experimental setup for static FEM verification	7
Figure 2-2	Laminate plate as viewed by optical tracking system: Visual output from DAQ for left) initial unloaded position, and right) fully loaded (25N) plate showing twisting	8
Figure 2-3	Laminate BT plate loaded in pure bending	9
Fig. 2-4	Thickness distribution for a [30°, 0°, 30°] test sample	10
Figure 2-5.	Twist vs. load for the experimental results	11
Figure 2-6.	Load vs. displacement for the experimental results	12
Figure 2-7	Experimental setup for static FEM verification	13
Figure 2-8	Tip displacement as viewed by optical tracking system	13
Figure 2-9	NREL S814 blade with 30° composite plies on working section of the blade.	14
Figure 2-10	Photograph of the three composite blades.	15
Figure 2-11	Blade CMM scan compared to actual NREL S814 airfoil.....	16
Figure 2-12	Tip of blade as loaded (1-4) as viewed by optical tracking system	19
Figure 2-13	Load vs. displacement for composite blades compared to FEM	20
Figure 2-14	Load vs. twisting for composite blades compared to FEM.....	20
<i>Figure 3-1.</i>	<i>Turbine rotor with the nose cone removed.</i>	22
Figure 3-2.	Towing tank carriage and turbine test setup	23
Figure 3-3.	Directions of blade bending moments.....	24

Figure 3-4 Left) blade root connection and strain gage location, Right) pin locator for pitch setting of blade root	25
Figure 3-5. $C_P - \lambda$ curve for varying inflow speeds.....	26
Figure 3-6. $C_T - \lambda$ curve for varying inflow speeds.....	27
Figure 3-7. $C_{M_y} - \lambda$ curve for varying inflow speeds.....	28
Figure 3-8. $C_{M_x} - \lambda$ curve for varying inflow speeds.....	29
<i>Figure 3-9. Thrust force on rotor as a function of inflow velocity and rotational velocity.</i>	30
Figure 3-10 Chord-Reynolds numbers.....	31
Figure 3-11. Combined uncertainty for calculated parameters.....	32
Figure 3-12 Percentage uncertainty for calculated parameters.	33
Figure 4-1. FEM of BT laminate plate bending displacement, with 25 N tip load	36
Figure 4-2. Twist vs. load for the experimental results	37
Figure 4-3. Load vs. displacement for the experimental results	38
Figure 4-14 Finite element convergence study: Computational time.....	40
Figure 4-15 Finite element convergence study: Bending displacement	41
Figure 4-16 Finite element convergence study: Longitudinal tensile stress.....	41
Figure 4-17 Blade mesh, 1.5 mm 2D quad elements.....	42
Figure 4-18 Load vs. displacement for composite blades compared to FEM	43
Figure 4-19 Load vs. twisting for composite blades compared to FEM.....	44
Figure 4-20 Aluminum blade displacement compared to composite displacement	45
Figure 5-1. $C_p - \lambda$ curves for Bahaj et al. experiment and BEMT.....	46
Figure 5-2. $C_T - \lambda$ curves for Bahaj et al. experiment and BEMT.	47
Figure 5-3. $C_p - \lambda$ and $C_T - \lambda$ curves for Gaurier et al. experiment (0.8 ms^{-1} and 5% turbulence) and BEMT results.	47
Figure 5-4 Thrust and torque on the turbine rotor as a function of number of blade elements	49

Figure 5-5 Computational time as a function of number of blade elements.....	50
Figure 5-9. $C_p - \lambda$ curve for NREL S814 blades (0.8 m/s) and Nevalainen BEMT, Swansea airfoil data.....	51
Figure 5-10. $C_T - \lambda$ curve for NREL S814 blades (0.8 m/s) and Nevalainen BEMT, Swansea airfoil data.....	52
Figure 5-11. Left) $C_{M_y} - \lambda$ curve, right) $C_{M_x} - \lambda$ curve, for NREL S814 blades (0.8 m/s) and Nevalainen BEMT.	52
Figure 6-1 Flow chart of coupled iterative FEM-BEMT design tool.	53
Figure 7-1 Blade element convergence for 4 m blade	58
Figure 7-2 Schematic of rigid blade (black), BT blade (red), and pre-deformed BT blade (blue), The * denotes the optimum α for design conditions.....	59
Figure 7-3 Flow chart for pre-deformed blade optimization	60
Figure 7-4 Original and pre-deformed blade pre-twist geometry.....	61
Figure 7-5 Induced tip twist and tip bending displacement of blade as a function of ply angle. 62	
Figure 7-6 Material safety factors in the transverse tensile and shear directions as a function of ply angle.....	63
Figure 7-7 Power coefficient for pre-twisted and original blade shape.....	64
Figure 7-8 Power coefficient for pre-twisted and original blade shape.....	65
Figure 7-9 SFs for original and pre-twisted blades with BT coupling.	65

LIST OF TABLES

Table 2-1. Material properties for laminate plates.....	9
Table 2-2. Uncertainty values for propagation	10
Table 2-3 Geometry of NREL S814 blade	15
Table 2-4: Composite and epoxy material properties [40, 43]	17
Table 2-5. Uncertainty values for propagation	17
Table 3-1. Precision uncertainty values, from calibration	31

Table 3-2. Bias uncertainty values 32

Table 3-3 - Results of the repeatability analysis. 34

1 INTRODUCTION

Power utilities are feeling the pressure to diversify their energy sources due to an increase in fossil fuel prices, decrease in the future availability of fossil fuels, and increased public pressure to lessen their environmental impact and reduce greenhouse gas emissions. Many governments are setting goals to have large percentages of their energy mix made up by renewable resources. For example, Nova Scotia's Renewable Electricity Regulations made under Section 5 of the Electricity Act state that by 2020 Nova Scotia utilities must supply their customers with at least 40% renewable electricity of the total amount of electricity supplied [1]. Of the renewable energy resources, tidal energy is a predictable and consistent energy source both spatially (in terms of location) and temporally (in terms of time of energy capture). Tidal energy development, particularly in Nova Scotia, has the potential to reduce the province's reliance on fossil fuels. Over the next 25 years, the tidal energy industry could create up to 22,000 full time positions and generate as much as \$815 million in labor income, according to a study commissioned by OERA [2].

There are two types of tidal energy extraction: devices that capture potential energy and devices that capture kinetic energy. Barrage type tidal energy systems are designed to capture the potential energy from the large tidal flux in shallow tidal estuaries, and in-stream tidal energy devices, or tidal energy converters (TECs), are designed to capture the kinetic energy from the movement of water. Tidal barrage technology has been around for decades, with one of the first systems located in Annapolis Royal, NS, Canada and coming online in 1984 [3]. Although there is great potential in terms of energy extraction, tidal barrages are damaging to local environment due to the dramatic change in tidal flow required to run a tidal barrage generator; furthermore, they have high capital costs [4]. For these reasons there is not significant continued development of this technology.

By contrast, TECs have comparatively low environmental impacts and efficient energy capture, but currently suffer large capital [5], installation and deployment [6], and maintenance costs [7, 8]. These costs, often referred to as capital and operating expenditures (cap-ex and op-ex), have a significant impact on the overall economic viability of TECs. For example, TECs with very high cap-ex requirements face significant barriers to entry given that investors are required to absorb considerable financial risk. This difficulty in raising investment capital often limits the advancement of tidal energy technologies [5]. Furthermore, a high op-ex will require an elevated feed-in tariff by electrical utility corporations for developers to be attracted to particular sites; the NS Utility and Review Board set rates of \$530 per megawatt hour (MWh) for projects producing less than 16,640 MWh per year or \$420 for projects producing greater than 16,640 MWh for developmental projects (15 year term), and \$575 for projects less than 3,330 MWh or \$455 for projects greater than 3,330 MWh (for 3 years) or \$495 for projects less than 16,640 MWh or \$385 for greater than 16,640 MWh (for 15 years) [9].

To become economically competitive, the cap-ex and op-ex must decrease by increasing power capture and/or decreasing device capital and maintenance costs, as well as increasing device reliability. This is a challenge in an emerging industry, as many developers are required to over-design devices (using more material and higher safety factors) to account for the uncertainty in the tidal environments [10]. For example, design increases of up to 30% have been reported to ensure the required durability [11], making devices larger and more expensive than necessary. As well, unreliable devices with high maintenance requirements result in turbine down-time as well as expensive un-planned device access.

To increase the cost effectiveness of TECs, continued work in the industry aims to increase the overall reliability of devices while minimising the cost per Megawatt of power [12]. The system reliability can be increased by identifying and improving the design of high risk components while maintaining structural and operational requirements. Turbine blades are predicted to be the component with the highest failure rates leading to turbine down-time [7]. Currently, a large percentage of turbine failures leading to unscheduled maintenance requirements are a result of blade failures and problems with variable pitch (VP) mechanisms. For example, Open Hydro's 16 m turbine installed in the Bay of Fundy, lost blades in 2010 [13], the two Verdant Power tidal turbines installed in the East River of New York City saw blade failures in 2006 [14, 15], and the Atlantis AR1000 turbine had blade fracture soon after its installation in the European Marine Energy Centre (EMEC) in 2010 [16]. As well, Marine Current Turbines lost blades when the VP mechanisms malfunctioned in Strangford Narrows, Ireland [17].

This document investigates turbine blade design as a means for reducing the failure likelihood and increasing cost effectiveness of in-stream TECs. The goal of this work is to demonstrate increased cost effectiveness of in-stream tidal energy devices by designing and trialing tidal turbine blades which passively adapt their shape based on site conditions. The turbine rotor is the sole component that captures power from the fluid flow and is responsible for a large percentage of the structural loads that have to be withstood by the device. Therefore, design optimization of the rotor blades can result in a more cost effective tidal turbine. As well, although the blade cost represents a fraction of the total cost of a TEC, loads from the blades are transferred into other components of the turbine, and therefore the size and cost of many sub-components are dependent on the performance of the rotor blades [18].

1.1 Background

Systems need to be designed to regulate the turbine power and loads with the consideration of the environment for which they are intended to be used; a consideration of the range of flow velocities and associated available power at a specific tidal site is essential to appropriate turbine design. The flow velocities and corresponding power available at an ideal tidal energy site cycle sinusoidally

over approximately a 6 hour period. As well, the profile of flow velocities varies over each month, having two limits of velocity: the mean spring peak velocity and mean neap peak velocity. The mean spring peak velocity is the greatest velocity that occurs at the site, while the mean neap is a smaller local maximum velocity which occurs when the spring/neap cycle is at a trough [19].

The peak available power at any tidal site is proportional to the cube of the maximum velocity, and the maximum thrust loads on the rotor are proportional to the square of the maximum velocity at that site. To capture the maximum available power at the site requires generators and turbine components (support structures, blades, *etc.*) to be sized for the peak power capacity and corresponding peak loads. If the power extracted exceeds the capacity of the generator, there is a chance of generator melt-down, which occurs when the voltages and temperatures exceed what the generator can handle and results in expensive equipment repairs. Similarly, the loads on the blades and structure have to be regulated such that the support system and turbine device (blades, nacelle *etc.*) are able to withstand peak loads. However, this peak power capacity is only available a small fraction of the time at a tidal site, for example spring tides only occur twice a month. Therefore sizing components to meet this peak power results in components that are oversized [12, 20] and hence significantly more expensive operating at less than 100% capacity for much of the time [20]. This means that power and loads need to be regulated, limiting the power output to less than the site peak available power and shedding mechanical and structural loads at high flow speeds. This decreases the required size of the generator and other turbine components while achieving a higher utilization factor [8].

Power capture and blade loads of a HATT are related to the lift and drag coefficients, which vary with the Reynolds number and other operating conditions. The number of blades, B , the chord line, c , the fluid density, ρ , and the radial location, r , are fixed during normal turbine operation, however the relative inflow velocity, V_{rel} , and the lift and drag coefficients can be adjusted to alter the thrust loads and power captured. The inflow velocity and lift and drag coefficients are not independent, since the lift and drag coefficients are functions of α , which depends on the rotational velocity and inflow velocity at each blade element, as well as the pitch setting, β , of the blade.

Typically as α decreases (feathering) the lift and drag coefficients decrease, resulting in a decrease in power capture and thrust loads. However, when α increases the lift coefficient typically decreases but the drag coefficient increases, resulting in an increase in loads. The power and loads on the blades can therefore be controlled by altering either the β (either β at the root-hub connection, or the pre-twist geometry- β along the blade span), or by changing the inflow and rotational velocity vectors, both which affect α .

Horizontal axis tidal turbines can have either fixed or variable blade-hub connections. Fixed pitch (FP) blades are rigidly attached at the root of the blade to the hub, and hence have no moving parts,

are less expensive and require less maintenance, making them economically attractive for the harsh underwater environment. However, they lack the ability to adapt their pitch angle to site conditions and therefore the efficiency of the blades can only be optimized for one particular flow speed, called the design flow speed. This means they are exposed to increasingly high thrust loads as flow speeds increase, necessitating a more robust and costly structure.

A VP mechanism controls the power and loads on the rotor by altering β at the root-hub connection during operation, which alters α to maintain the optimum angle. This enables the blades to actively feather to limit the thrust loads and peak power produced by the rotor to prevent overpowering the generator and damaging equipment. In the wind industry, VP blades have become standard practice for large scale devices [21]. However, in the subsea environment there are issues with mechanical systems being exposed to corrosive salt water, having sealing issues making it more challenging and the significantly higher loads that the rotor and structure are subjected to. Therefore, while VP blades allow for optimization of power capture over a range of flow speeds, they are more expensive and have a higher risk of failure. As well, because of the high cost to access devices underwater, control system failures are costly to repair.

Methods of achieving conceptually similar blade optimization and control using passive techniques for FP blades introduces a potentially lower maintenance and lower cost alternative to VP blades. Blade designs which are tailored such that they passively optimize the angle of attack as a function of both the inflow conditions and the span-wise location could decrease the complexity and expense of the system while maintaining a high level of energy extraction and decreased structural loads [22]. These blades are called passively adaptive blades.

Passively adaptive blades have been shown to be advantageous because of their ability to adapt to operating conditions without the use of mechanical actuators. Rigid blades achieve optimal performance at the design operating condition, however, when the operating condition changes from the design values, the blade geometry becomes sub-optimal relative to the changed inflow. At sub-optimal operation, the blade efficiency decreases and the rotor may be subject to fatigue, vibration and stability issues [22]. Passively adaptive blades decrease the risk of overpowering the generator and overloading the structure by regulating the power and loads.

Passively adaptive blades are also less expensive than VP blades and have the potential for lower maintenance requirements due to their simplicity. An example of this is a bend-twist (BT) coupled composite tidal turbine blade which passively adjusts the blade twist as a function of the radius, changing the angle of attack of the blade. BT coupled composite materials are designed so that loading along one material axis causes deformation in another material axis. BT coupled composite turbine blades couple the flap-wise bending of blade due to thrust loads with span-wise twisting, and can therefore passively change their pitch angle. This results in reduced structural loads by

twisting toward feather (decreasing angle of attack) or increased power capture by twisting toward stall (increasing angle of attack).

From ongoing research in other industries such as the marine vessel industry [23] and wind energy industry [24], BT coupling of composite materials is a promising way to achieve this passively adaptive behavior for tidal turbine blades. In the wind industry, VP blades and stall regulated FP turbines have become standard practice [21]. However, in the subsea environment there are issues with mechanical systems being exposed to corrosive salt water, having sealing issues, and subject to significantly higher loads [25]. As well, because of the high cost to access devices underwater, failures are more costly to repair, increasing the necessity for mechanically robust components. Passively adaptive blades are seen as an economically feasible solution to the problem of load mitigation and power regulation.

BT blades that twist toward feather with increasing flow speeds can also potentially decrease the rotor power production past the design conditions to provide a more predictable peak level of power output to the generator. Reducing structural loads by feathering the blades also enables a smaller support structure to be used, which can considerably decrease the cost of the overall system since the support structure typically makes up a large percent of the device capital cost. For example, a report by the Carbon Trust suggested that the support structure made up 39% of the total capital cost of a tidal stream farm [26], and for offshore wind the cost of substructure is estimated to be around 20–30% of the capital cost of a device [27]. Lower loads also means that longer blades can be used with the same support structure, increasing the power capture of the device by increasing the rotor area [28].

SCHOTTEL developed a hydrodynamic blade design which minimizes the thrust forces using passive pitch adaptation to reduce the loads on the support structure. Based on full-scale testing of a 4 m diameter rotor on the front of a tug boat, a 50% reduction in thrust loading at a flow speed of 5 m/s was realizable [29]. Recently, Motley and Barber [30] applied an iterative 3-D potential-based boundary element method finite element method (BEM-FEM) solver (initially developed for marine propellers) to the problem of passive pitch adaptation to describe potential benefits of passively adaptive blades. These studies showed that passively adaptive blades could increase annual energy capture by delaying the onset of cavitation [31], thus enabling the use of larger blades operating at higher rotational speeds, increasing the annual energy capture [32].

1.2 Objectives

To effectively utilize composites for BT coupling in a tidal turbine blade, a blade design needs to be developed such that the span-wise twist behavior is realized, but the structural requirements (stiffness, strength, etc.) are met as well. The increased flexibility of BT turbine blades necessitates

a fluid-structural interaction design methodology, whereby the fluid regime and associated rotor performance is considered in the design.

This document outlines the development of a design tool that iterates between the structural performance (deformation and material stresses) and hydrodynamic performance (power and thrust loads) of passively adaptive blades. A finite element model (FEM), developed using the commercial finite element software Altair® Hyperworks RADIOSS® and verified through static bending tests, was used to predict the deformation and stress in composite BT blades, and a blade element momentum theory (BEMT) code, verified by experimentally testing rigid aluminum blades in a towing tank, was used to calculate the performance (thrust loads, power capture and blade material stresses). The coupling of the FEM and BEMT tools is a useful instrument for early stage blade design iterations as it is fast and computationally inexpensive, compared to commonly used computational fluid dynamics (CFD)-FEM coupled codes [33].

The development of the coupled FEM-BEMT design tool, structural and hydrodynamic testing of small-scale blades for model verification, as well as a full-scale BT turbine case study, are presented here.

2 STRUCTURAL TESTING

Laminate plates and composite blades were tested statically in bending to investigate the structural response of BT composite structures. This section outlines the experimental setup, data acquisition, uncertainty analysis, and results of these tests.

2.1 Laminate plates

Laminate plates were tested first as they are a less complex geometry than blades, increasing confidence in the accuracy of the ply layups and reducing uncertainties in a FEM upon verification, given in Section 0.

2.1.1 Experimental setup

A static bending test setup was designed to constrain the base of the plate and apply a single point load along the plate length. Figure 2-1 shows the test setup used to test the laminate plates.

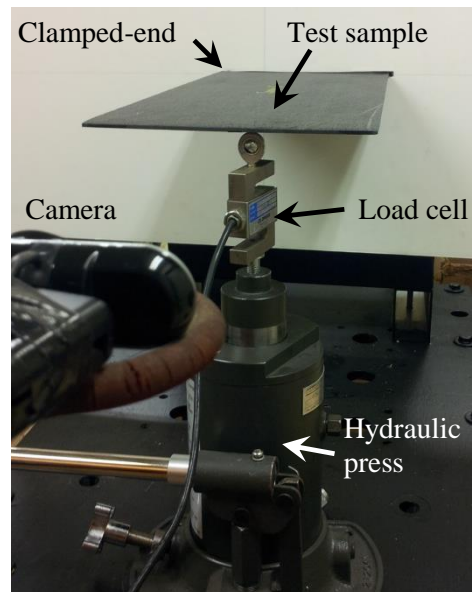


Figure 2-1 Experimental setup for static FEM verification

A Carver model 3912 Hydraulic ram press with a 5.125-in (0.130175 m) maximum ram stroke was used to load the free-end of the plate, half-way along the plate width. The load was applied using a 2 mm diameter ball. An LCCB-100 load cell with a 100 lb. (444.82 N) maximum load and a 10 V power source was used to measure the load applied with National Instruments data acquisition (DAQ) 9239. The load cell was calibrated following the procedure laid out in ITTC [34].

The twist of the tip of the plate was a function of the location of the free-end of the plate (Edge 1 and Edge 2 in Figure 2-2). Locations of the free-end (x and y coordinates as viewed front on) were obtained using LabVIEW Vision Development Module with an A4 Logitech® PK-920H-1 (1280

x 720p MJPG 30 fps) webcam. The edge matching function in LabVIEW was used to locate an edge feature in an otherwise grayscale image. LabVIEW recorded the image and converted (using a calibration with a known uncertainty) the pixel location of these features to x and y coordinates in millimeters. Figure 2-2 shows what the optical tracking system viewed as a laminate plate was loaded.

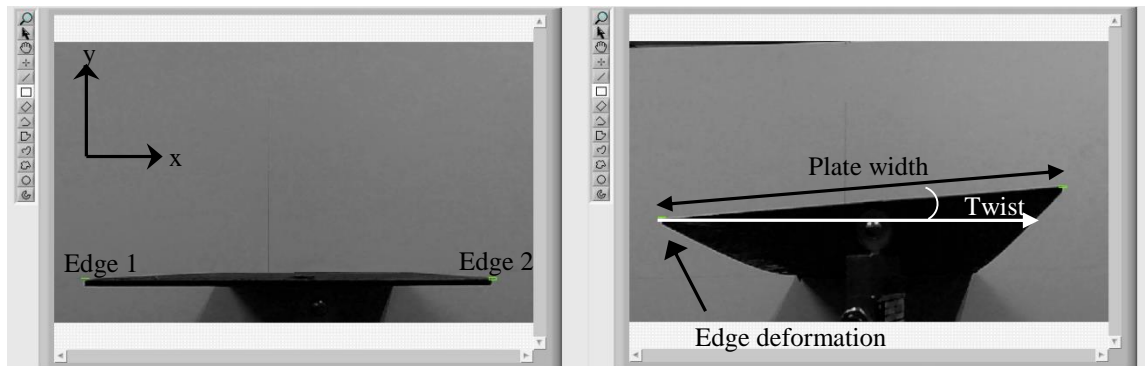


Figure 2-2 Laminate plate as viewed by optical tracking system: Visual output from DAQ for left) initial unloaded position, and right) fully loaded (25N) plate showing twisting

The plate twist was measured by taking the arcsine of the y -displacement difference between Edge 1 and Edge 2 divided by the plate width.

2.1.2 Laminate construction

A schematic of the laminate plate geometry and loading scenario is shown in Figure 2-3. Based on results of an analytical model based on CLT, as discussed in [35], the FEM and test samples were made with three ply layers and a layup of $[30^\circ, 0^\circ, 30^\circ]$.

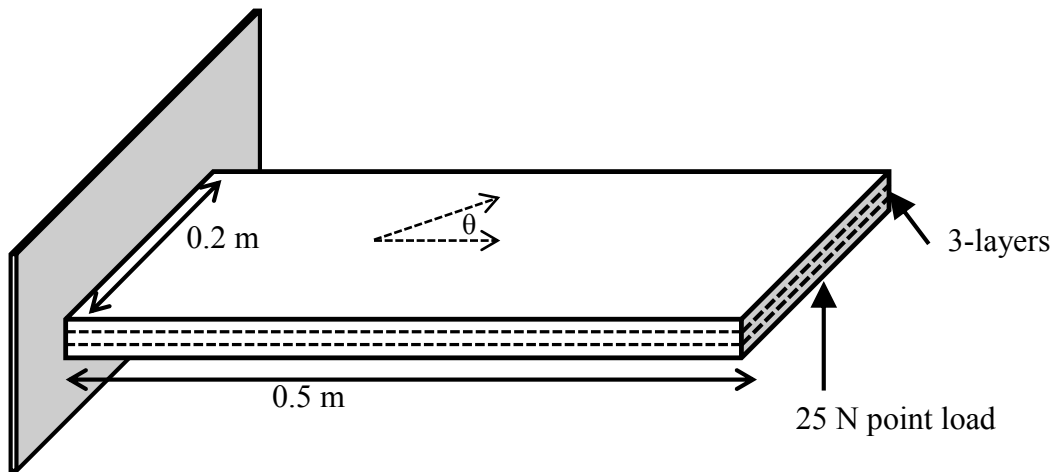


Figure 2-3 Laminate BT plate loaded in pure bending.

The laminate plate test samples were made by Airborne Marine (The Netherlands) out of Zoltek Panex uni-directional carbon fiber [36] and Gurit Prime 27 epoxy [37], for a typical Fiber Volume Fraction (FVF) of 55%, with material properties given in Table 2-1.

Table 2-1. Material properties for laminate plates

Material property	Value
Standard weight	342 g/m ²
Young's modulus, fibers (E11)	126 GPa
Young's modulus, matrix (E22/ E33)	7.7/7.7 GPa
Shear modulus (G12/G13/G23)	3.9/3.9/2.9 GPa
Poisson's Ratio	0.35

After the plates were manufactured, a coordinate measuring machine (CMM) machine was used to scan the geometry to measure the final thickness of the plate samples. The CMM has a resolution of 5 μm and a measurement probe diameter of 1.5 mm and was measured in 5 mm steps. Fig. 2-4 shows the thickness distribution for one test sample.

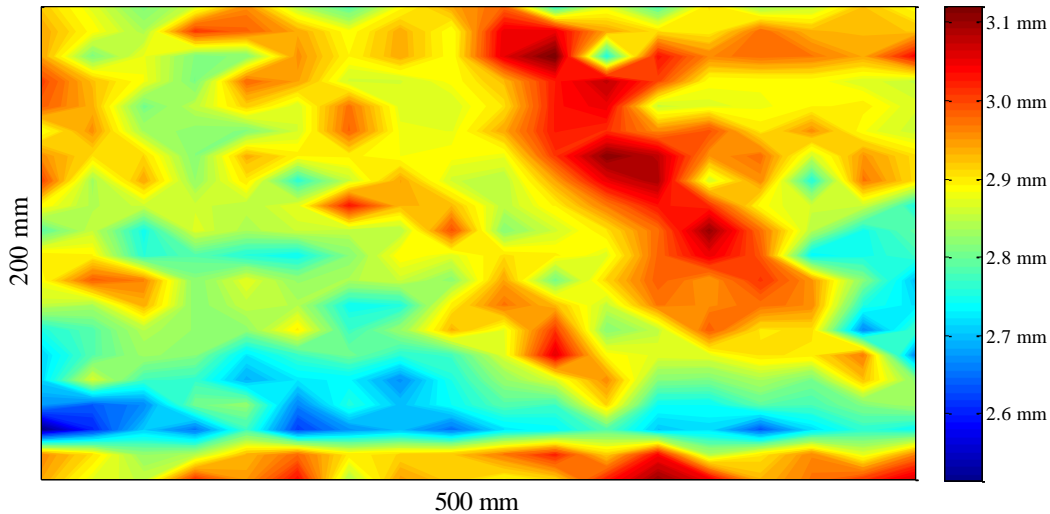


Fig. 2-4 Thickness distribution for a $[30^\circ, 0^\circ, 30^\circ]$ test sample

For this sample, the average measured thickness was $t_{\text{avg}} = 2.72$ mm with a standard deviation of 0.18 mm. The thickness of all of the 500 mm x 200 mm laminate test samples was found to vary similarly across the sample.

2.1.3 Uncertainty

Both random and bias uncertainties were propagated through the load measurements and calculations of displacement and twist. The combined uncertainty for each parameter based on a 95% confidence interval was determined. Table 2-2 gives the uncertainty values used in the propagation.

Table 2-2. Uncertainty values for propagation

<i>Variable</i>	<i>Uncertainty</i>
Load cell (N) –bias, given by manufacturer	0.22
Load cell (N) –precision, linear regression analysis	0.094
Displacement (mm) –precision, measurement tool	0.65

The uncertainty in the bending displacement was based on the calibration uncertainty and the uncertainty in the image sensing, which is an output from the vision software calibration; the calibration software produced an error map, with the error value, u_y , of the pixel coordinate indicating the largest possible location error for the estimated real-world coordinates. The total uncertainty in the image sensing was calculated by LabVIEW to be $u_y = \pm 0.65$ mm.

The bias uncertainty of the load cell, u_v , based on the manufacturer specifications, was $u_v = \pm 0.015$ mV. Calibration of the load cell was done by applying weights of a known mass and

measuring the voltage output. Based on the standard error of estimate of the measured data, the calibration uncertainty was $u_{\text{Calib}} = \pm 0.094$ N. This gave an overall uncertainty, for a 95% confidence interval, in the load measurement of $u_{\text{load}} = \pm 0.48$ N for a 25 N load. The uncertainty in all the components was found to be less than 5% for loads over 7 N, with error bars shown in the results plots (error bars for displacement are not visible behind the marker).

2.1.4 Results

Figure 4-2 and Figure 4-3 show results obtained for $[30^\circ, 0^\circ, 30^\circ]$ laminate test samples, with an average thickness of 2.72 mm. The tip displacement shown is the maximum displacement of free end of the plate, relative to the initially unloaded plate.

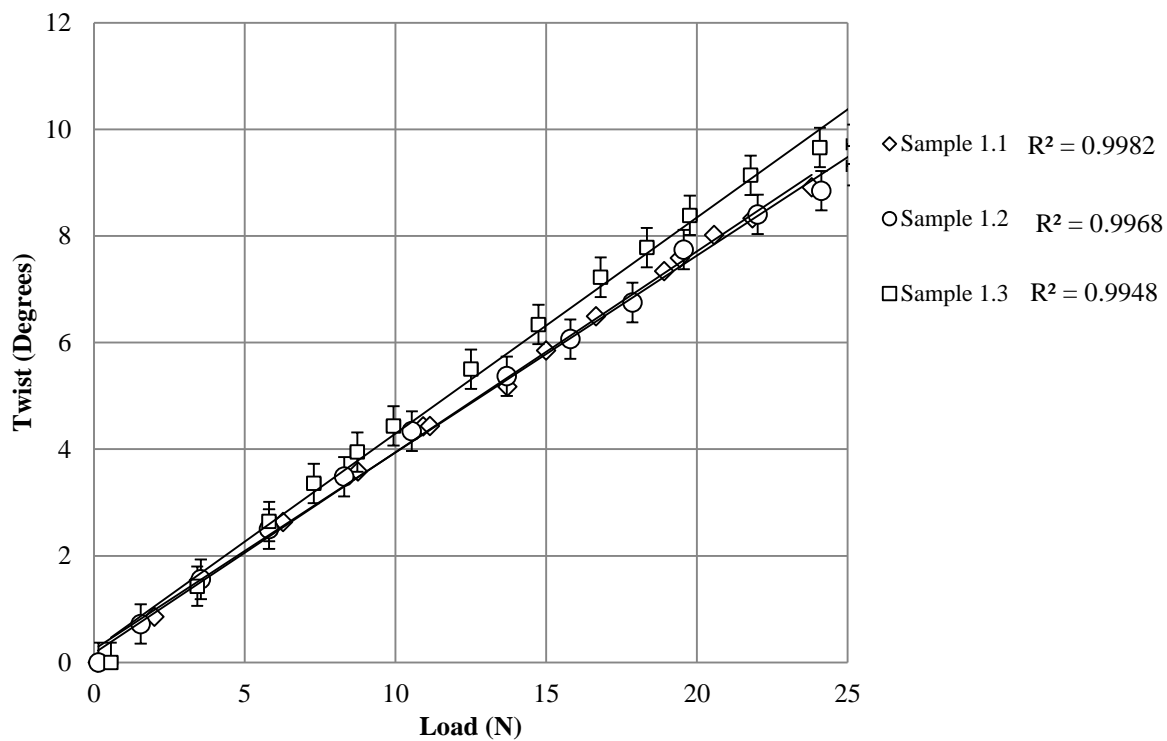


Figure 2-5. Twist vs. load for the experimental results

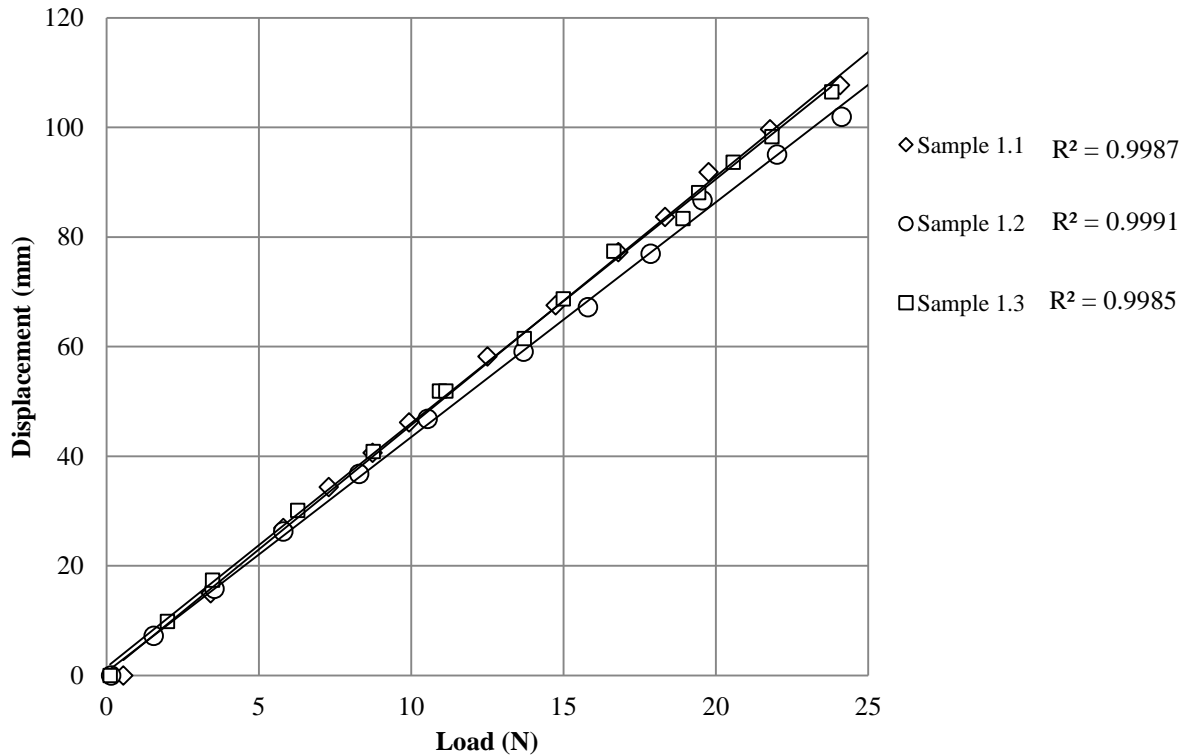


Figure 2-6. Load vs. displacement for the experimental results

The deformation of the test samples with increasing load was linear within the range of applied loads, with all coefficients of determination above 0.99. In a similar study, Makeev [38] showed non-linear load-twist trends, however, this is thought to be due to the high loads applied (over 1 kN for a 1.168 mm thick laminate). There was slight variance in the bending and twisting response between test samples, which is thought to be due to slight offsets in the ply angles and thicknesses.

2.2 Turbine blade

This section outlines the construction of three 360 mm long NREL S814 airfoil shape composite blades built by Airborne Composites, Netherlands, as well as static test results for these blades. Small-scale blades were used for pragmatic testing and manufacturing reasons, as is typically done for early stage device design [39]. Aluminum blades of identical geometry were tested as well to verify the assumption that they were rigid. Results for these tests are discussed in detail in Section 4.2.3.

2.2.1 Experimental setup

Figure 2-7 shows the test setup used for the blades, with a similar DAQ setup as outlined in Section 2.1.1 for the laminate plates.

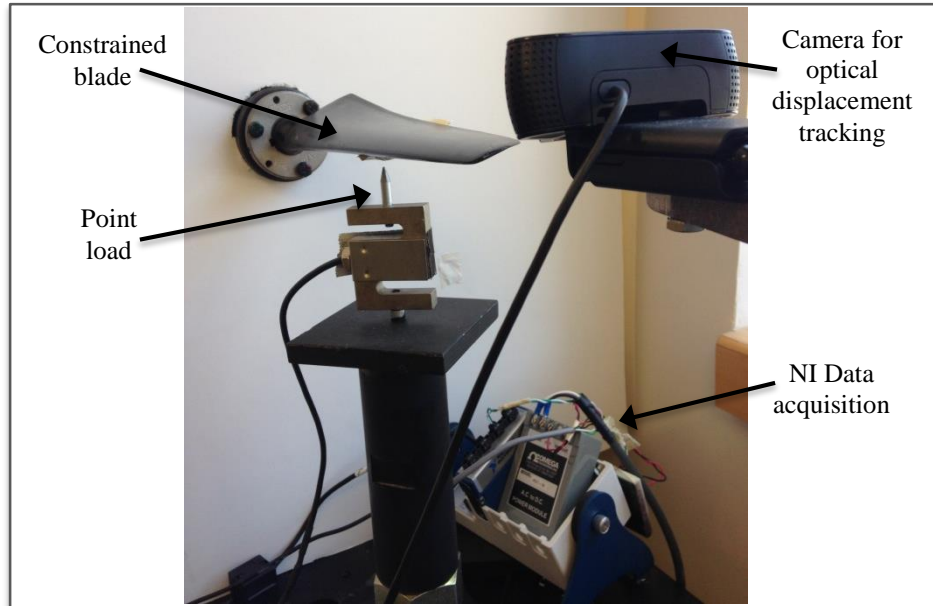


Figure 2-7 Experimental setup for static FEM verification

The experimental setup and DAQ described in Section 2.1.1 was used for the blades as well, with the exception of a screw press (maximum stroke of 0.15 m) replacing the hydraulic press for better stability in loading. A single point load was applied to the blade at 60% along the blade length and 25% along the blade chord line. The load was applied using a 1 mm diameter rounded tip applicator, as shown in Figure 2-7. A quick-disconnect taper-lock bushing was used to connect the circular root of the blade to the bending test platform.

Figure 2-8 shows the output view from the optical tracking system as a blade is loaded.

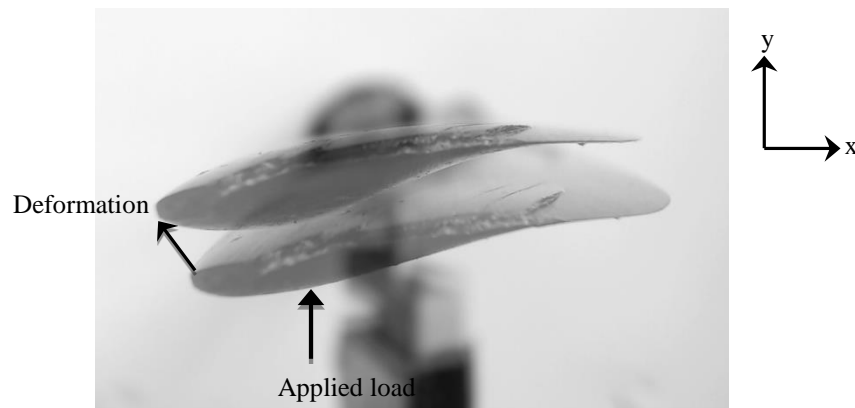


Figure 2-8 Tip displacement as viewed by optical tracking system

The blade twist was measured by taking the arcsine of the difference in the displacement of the leading and trailing edges of the blade divided by the chord line at the blade tip, similarly to the twist measurements of the laminate plate.

The crack at the blade tip visible in this figure was from the pressure change during air transportation of the blades. This crack was repaired and blade tests repeated with no difference in deformation response.

2.2.2 Blade geometry

Three 360 mm long NREL S814 airfoil shape blades, shown in Figure 2-9 and Figure 2-10, were manufactured by Airborne Marine, The Netherlands, and tested statically to verify the deformation predictions made by the FEM.

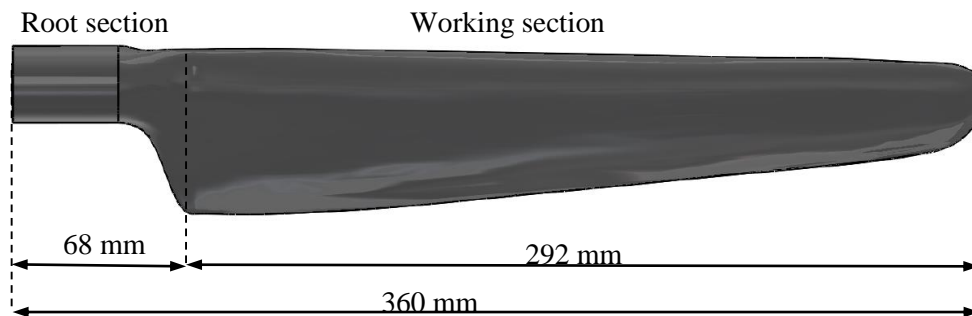


Figure 2-9 NREL S814 blade with 30° composite plies on working section of the blade.



Figure 2-10 Photograph of the three composite blades.

The working section of the blade (outer 292 mm) had radial chord and pre-twist distributions given in Table 2-3. The root section of the blade (from 0 mm to 68 mm, shaded grey in the table) is given as well.

Table 2-3 Geometry of NREL S814 blade

Blade length (mm)	Twist (Degrees)	Chord (m)	Airfoil shape
0	N/A	29	Circular root
39	N/A	29	Circular root
40	N/A	29	Circular root
50	N/A	N/A	Lofted (ellipse)
68	0	64.3	NREL S814
93	-4.38	62.9	NREL S814
128	-10.74	59.8	NREL S814
162	-14.8	56	NREL S814
195	-17.33	51.6	NREL S814
230	-18.91	47.3	NREL S814

265	-19.75	42.6	NREL S814
300	-20.39	38.1	NREL S814
334	-20.87	33.7	NREL S814
360	-21.11	24.9	NREL S814

The blade was lofted from a circular root cross section, 40 mm from the base of the blade, to the first NREL airfoil cross section at 68 mm. The circular root had a 1-inch diameter steel cylindrical insert for added strength in compression for a taper-lock bushing connection to the bending test platform. This steel insert was overlaid with composite to give a total outer diameter of 29 mm.

After the blades were manufactured, a CMM machine was used to scan the blade geometry to identify any features or effects that were not present in the original blade CAD. The CMM has a resolution of 5 μm and a measurement probe diameter of 1.5 mm. Measurements of the airfoil sections were taken at 17 span-wise locations, with 0.127 mm increments around the airfoil. Figure 2-11 shows the cross section of the composite blade at 68 mm from the base, compared to the actual NREL S8414 airfoil.

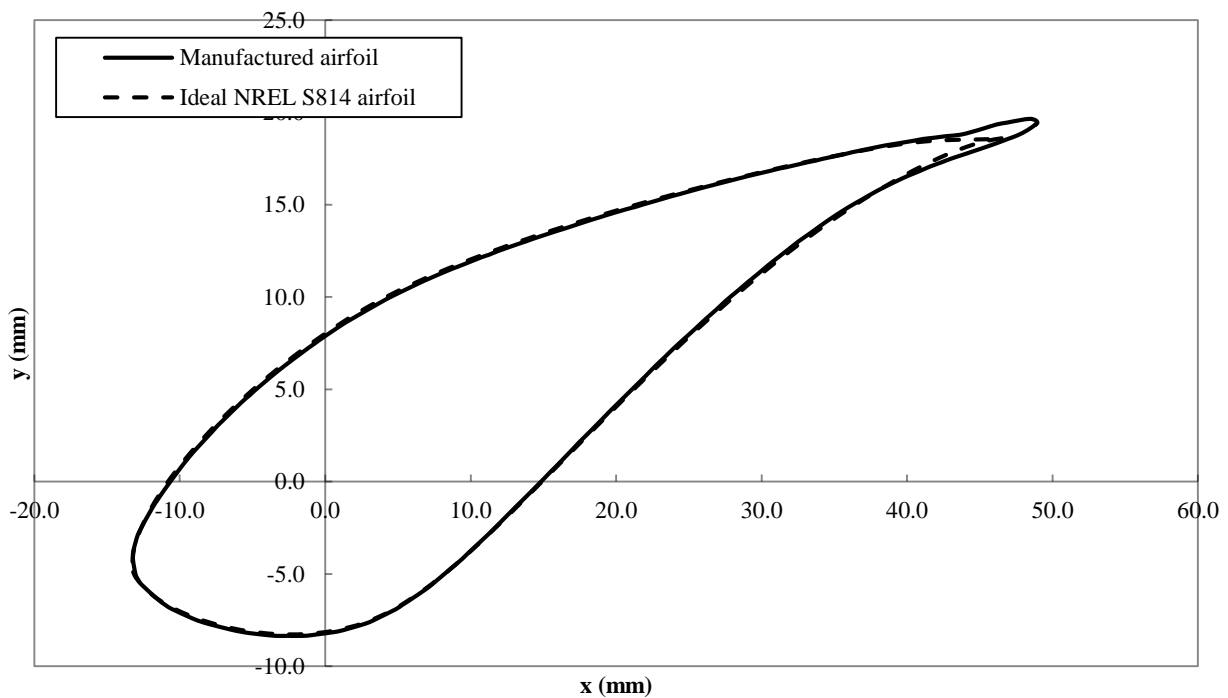


Figure 2-11 Blade CMM scan compared to actual NREL S814 airfoil

Figure 2-11 highlights the differences between the original airfoil and the blade after manufacturing, particularly showing the extended TE on the manufactured blade. Due to the small size of the blades and the required mirror layup preventing wrapping the composite around the

blade trailing edge (TE), an additional 5 mm section was required on the TE in order to bond the composite from the top and bottom surfaces of the blade. This additional TE length was considered in any FEM of these blades, but when compared to the original CAD, had little effect on the structural response of the blade (bending and twisting).

2.2.3 Blade construction

Blades were constructed of Sicomin PB 250 [40] epoxy closed cell foam core (for hydrodynamic shape and ease of manufacturing) and 0.2 mm thick uni-directional graphite-epoxy composite with fibers at a 30° angle from the long-axis of the blade to induce BT coupling. The upper and lower skin were laid up with a mirror layup, as detailed in [41]. The root section had continuous 30° plies from outer blade section with additional layers of $\pm 15^\circ$ plies for added strength.

Table 2-4 shows the material properties used in the blade manufactured by Airborne Composites, Netherlands. Graphite-epoxy ultimate strength values are stated in Table 2-4 for the laminate longitudinal (σ_{ult}), transverse (σ_{2ult}), and shear (τ_{12ult}) directions, in both tension and compression (superscript *T* and *C*) [42].

Table 2-4: Composite and epoxy material properties [40, 43]

Graphite-epoxy Properties		Sicomin Epoxy Properties	
Young's modulus, longitudinal	137 GPa	Density	250 kg/m ³
Young's Modulus, transverse	7.8 GPa	Compressive modulus	0.0189 GPa
Shear modulus	3.9 GPa	Shear modulus	0.0073 GPa
Poisson's Ratio	0.335	Poisson's Ratio	0.3
Longitudinal tensile strength	1.5 GPa		
Transverse tensile strength	0.04 GPa		
Longitudinal compressive strength	1.5 GPa		
Transverse compressive strength	0.246 GPa		
Shear strength	0.068 GPa		

2.2.4 Uncertainty

Table 2-5 gives the uncertainty values used in the propagation of uncertainty calculation.

Table 2-5. Uncertainty values for propagation

VARIABLE	Uncertainty
Load cell (N) –bias, given by manufacturer	0.22
Load cell (N) –precision, from calibration	0.14
Displacement (mm) –precision, from measurement tool	0.20

The uncertainty in the bending displacement was output from the vision calibration software. The bias uncertainty of the load cell, u_v , based on the manufacturer specifications, was $u_v = \pm 0.015$

mV, resulting in approximately ± 0.22 N. Based on the standard error of estimate of the measured data the calibration uncertainty was $u_{\text{Calib}} = \pm 0.37$ N. This gave an overall uncertainty in the load measurement of $u_{\text{load}} = \pm 0.26$ N for a 25 N load. For a 95% confidence interval, the combined uncertainty in the load was less than 5% for loads above 5 N.

Due to limitations in merging the vision software and load measurements, data was only recorded at a rate of 1 Hz, hence the blade was loaded slowly to capture a sufficiently large data sample. Each set of tests were performed a minimum of three times, with one set of tests being done 5 times, to ensure experimental repeatability.

Optical distortion was an issue during the LABVIEW vision tracking, as pixels further away from the center of the lens focus were slightly distorted, making the twist measurements, which were highly sensitive (within a few pixels) challenging to obtain. As a check on the actual “real-world” accuracy of the vision measurement, a non-contact visual measurement system integrating the LABVIEW optical tracking system with MATLAB® image processing was used to measure a cylindrical object of known length (60 mm) and diameter (0.7 mm) at the same focal length as the blade tip. Upon observation of the free-ends of the object in MATLAB®-processed images, the smallest apparent division was one pixel, therefore the uncertainty in the observation was estimated at half of the smallest division, so half of one pixel, equating to 0.06 mm based on an image calibration of 0.12 mm/pixel. Therefore, the 0.2 mm uncertainty in the vision tracking calculated in LabVIEW is a conservative estimate.

2.2.5 Results

Figure 2-12 shows the blade tip as viewed by the optical tracking system as it is loaded.

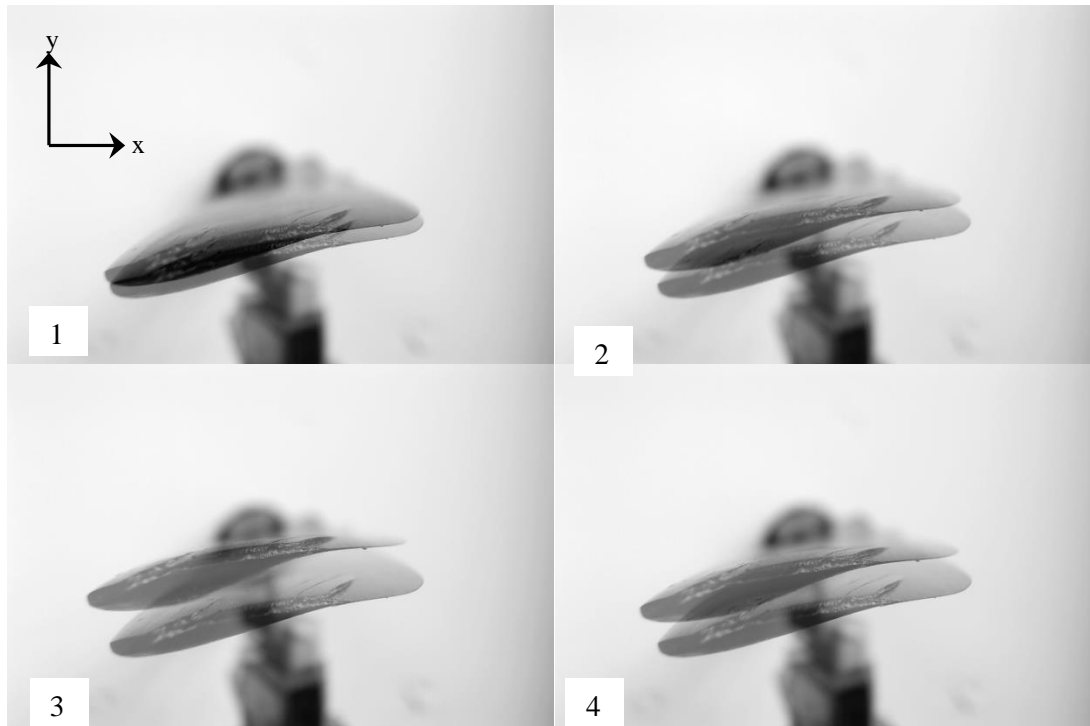


Figure 2-12 Tip of blade as loaded (1-4) as viewed by optical tracking system

As the blade was loaded, it mainly deformed in the y -direction, but there was also a slight deformation in the x -direction. Figure 2-13 and Figure 2-14 show the blade bending displacement in the y -direction (for the TE, which had the largest y -displacement) and tip twist, respectively, as a function of applied load.

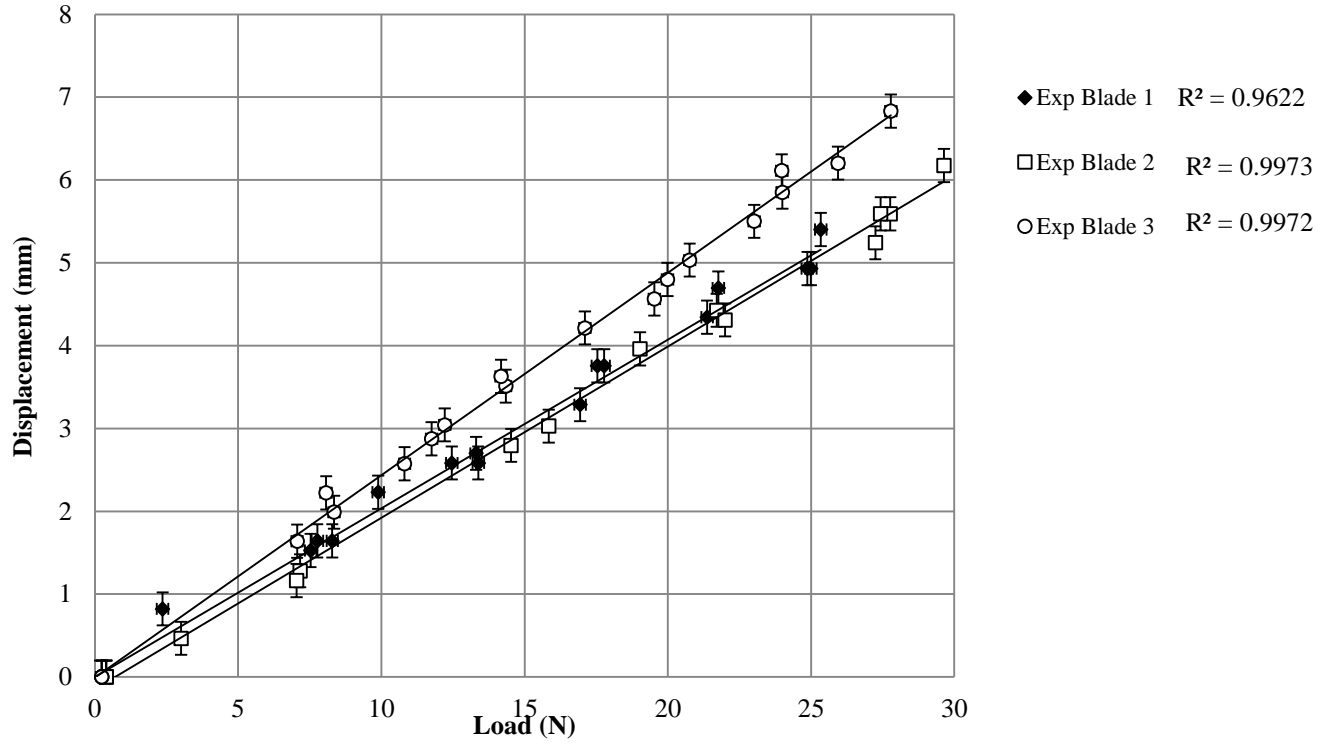


Figure 2-13 Load vs. displacement for composite blades compared to FEM

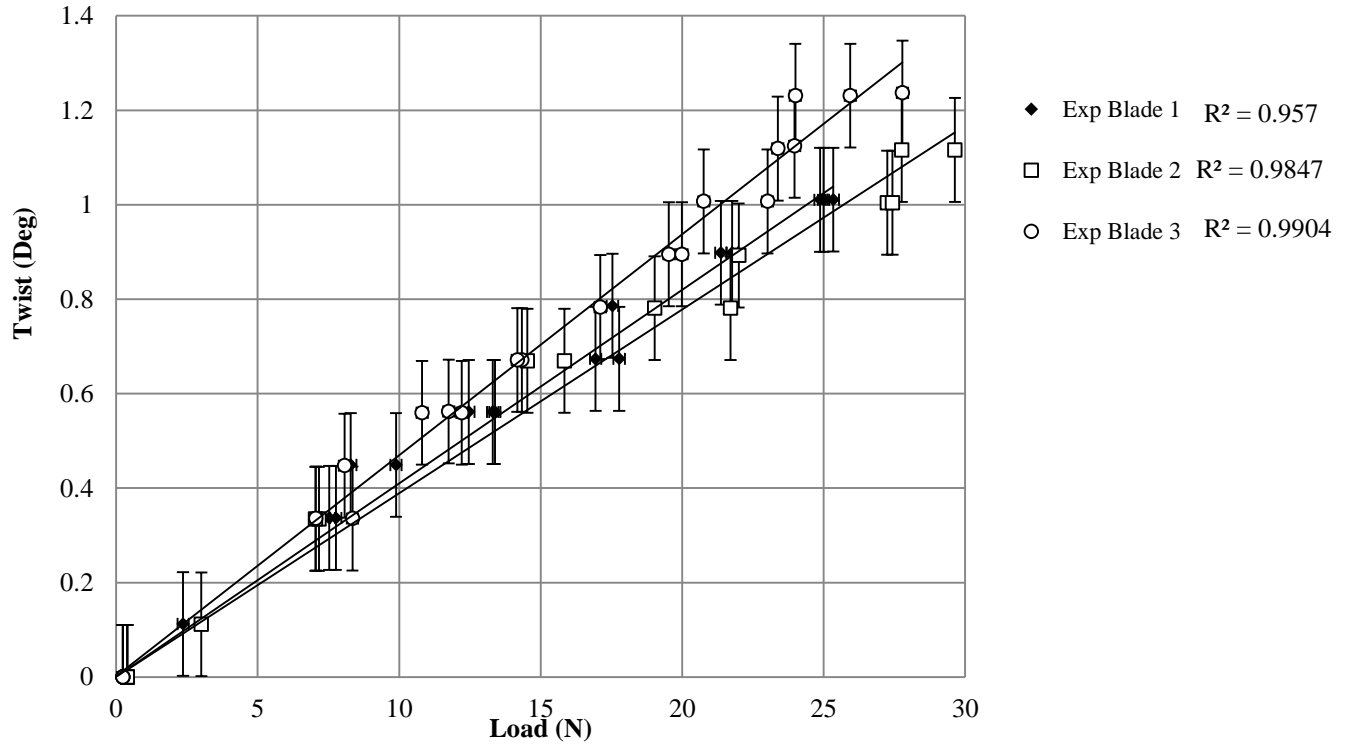


Figure 2-14 Load vs. twisting for composite blades compared to FEM

Both the bending displacement and twist were linear, with R^2 values shown on the plots. Figure 2-13 shows different load-displacement trends for each blade, highlighting the slightly different bending responses between the three blades. This is due to slight ply angle misalignments, whereby the three blades had differing fiber angles, with blade 1 having an overall fiber angle of 26° , blade 2 having a fiber angle of 26.5° and blade 3 having a fiber angle of 28° . Manufacturing small-scale blades is challenging due to the relatively high curvature of the surfaces, and these misalignments, along with the extreme sensitivity of the bending response to ply angle, are not expected to be an issue for larger scale blades.

3 HYDRODYNAMIC TESTING

A turbine with three aluminum blades was tested in the towing tank at Strathclyde University to be used for verification of a steady BEMT tool. This section outlines the experimental setup, data acquisition, uncertainty analysis, and results of these tests.

3.1.1 Turbine and blade configuration

Figure 3-1 shows the 0.762 m diameter turbine rotor with NREL S814 airfoil shape blades with the nose cone removed to show the blade root strain gages. During testing, the centre of the nose cone of the rotor was located 0.70 m below the free surface of the water.

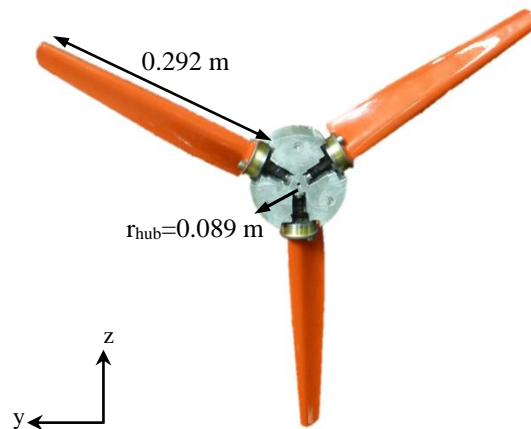


Figure 3-1. Turbine rotor with the nose cone removed.

The rotor had a radius of 0.381 ± 0.0005 m, blade length of 0.292 ± 0.0005 m, and root pitch setting of $28.00^\circ \pm 0.89^\circ$. The blade radial chord and pre-twist are given in Table 2-3. It should be noted that only the working section of the blades were tested, the root section outlined in the table was not manufactured for these blades. Instead, the blades had a flange with two bolts to attach it to the hub, as evident in Figure 3-1.

Figure 3-2 shows the experimental configuration tested in the 76 m by 4.6 m by 2.5 m towing tank at the University of Strathclyde. The maximum carriage speed for this facility is 5 m/s with speed control accurate to better than 0.3% [44].

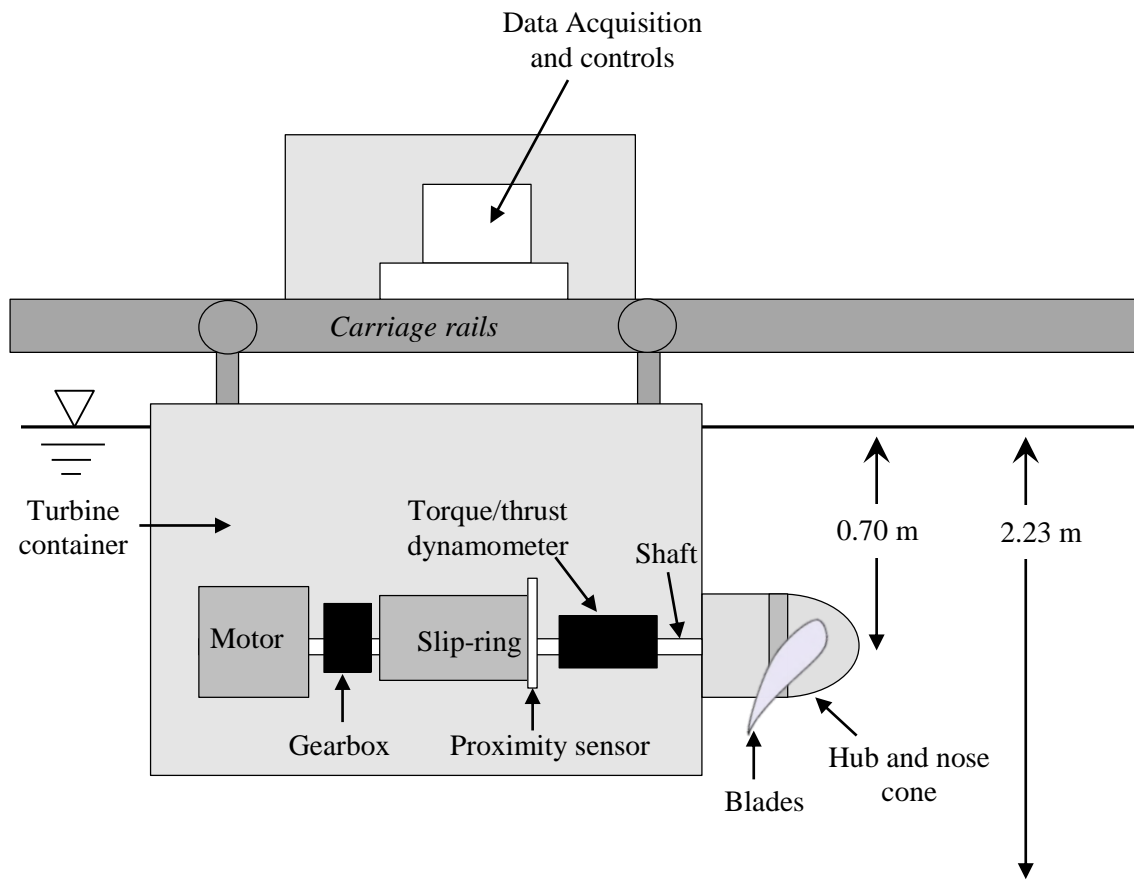


Figure 3-2. Towing tank carriage and turbine test setup

The rotor was driven at a constant rotational speed using a motor and a 10:1 gear box was used to step down the rotational speed of the motor. The thrust and the torque loads on the rotor system were measured using a Futek FSH00747 torque and thrust biaxial sensor, and the axial (blade 1 and 2) and radial (blade 3) blade bending moments were measured using strain gages attached to the blade root. The strain gages were located on a cylindrical steel root section of the blade internal to the hub, and were isolated from the water with waterproofing material, as shown in Figure 3-4. The direction of the measured bending moments is given in Figure 3-3.

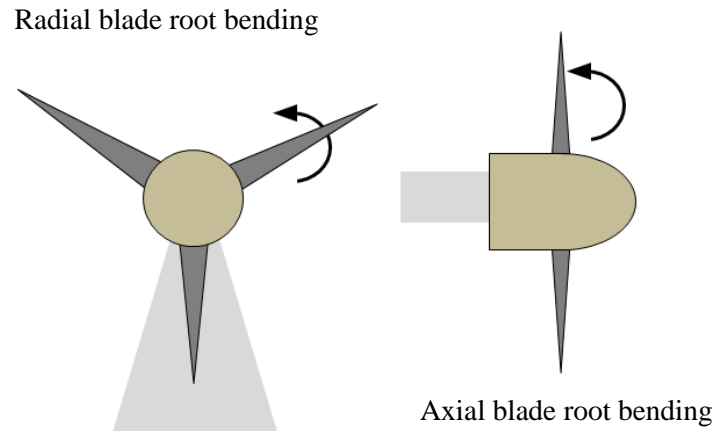


Figure 3-3. Directions of blade bending moments.

A IS 1163 SW 110/20 CAT slip ring was used to feed the electrical signal from the rotating dynamometer and strain gages to the DAQ. A proximity sensor was used as a pulse counter to measure the shaft rotational speed and to identify the shaft radial location at any time. The higher frequency motor encoder was also used as a backup to check the rotational speed measured by the proximity sensor. Data was logged using a Cambridge Electronic Design Power 1401 DAQ and the DAQ program, Spike, and exported as text files for post processing in MATLAB®.

Along with bolting the blade flanges to the hub, to ensure an accurate pitch setting between the three blades, a pin was slotted into a hole drilled on the bottom-side of the blades at a set point on the chord line, constraining the blades to one degree of freedom in rotation about the pin, shown in Figure 3-4. A high accuracy depth gauge fixed in the horizontal plane was used to measure the distance between the edge of the rotor hub and the trailing edge of the blade at the root, and insure this distance was the same for all blades. The blade pitch angle was then determined from the CAD model of the rotor system. The uncertainty in the blade pitch angle was calculated based on a machining tolerance of 0.005 m for each dimension of the blades, considering the method used to set and quantify the pitch angle.

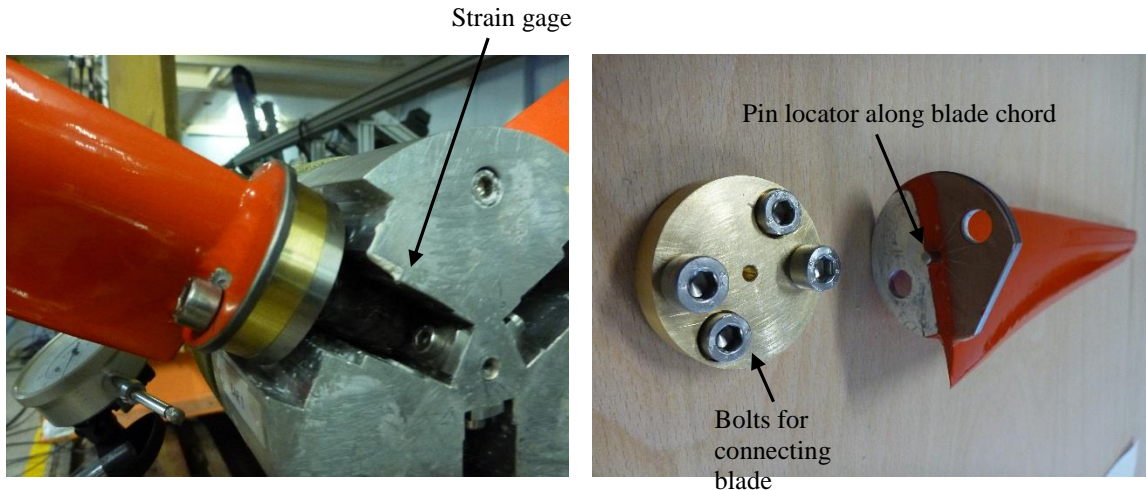


Figure 3-4 Left) blade root connection and strain gage location, Right) pin locator for pitch setting of blade root

A calibration process was undertaken both prior to testing and once the test period had been completed to ensure the measurements taken were reliable and could be processed with confidence. A series of calibration equations of the form $V_{\text{measured}} = sT_{\text{applied}} + a$, where s was the slope and a the offset constant of the calibration curve, were applied to convert voltage signals from the DAQ to engineering units for thrust sensor, torque sensor, and bending moment strain gauges. For each sensor, a linear regression analysis of the various applied loads (torques, bending moments and thrust forces) and resulting voltages showed a highly linear calibration curve with coefficients of determination, R^2 , above 0.99.

3.1.2 Design of Experiment

A range of inflow speeds (rotor inflow velocities) were used during the towing tank testing, from 0.5 m/s to 1.0 m/s. For each inflow speed, a range of rotational velocities, designed to cover λ from 2 to 7, were utilized to populate rotor performance curves. At higher inflow velocities, a slightly fluctuating torque signal was observed, thought to be due to the motor controller not able to maintain enough torque to counter the hydrodynamic torque and control the rotor, hence the maximum flow speed was 1.0 m/s.

To meet the testing requirements outlined in EquiMar Deliverable D3.4 [45], tests were run in a non-sequential order and were scheduled to avoid random errors such as time of day (affecting steadiness of tank), carriage operators (affecting data collection) and tank temperature (which can vary over the day). The carriage tow and rotor velocities of the tests were also chosen at random to ensure that any sources of uncertainty described as “nuisance factors” in the EquiMar Best Practices document [45] could be eliminated. A number of repeat runs were performed as well to

determine the repeatability of the tests. In particular one set of conditions, with an inflow velocity of 1 m/s and rotor velocity of 110.7 RPM, was repeated 5 times.

3.1.3 Results

Figure 3-5 and Figure 3-6 show C_P and C_T as a function of λ .

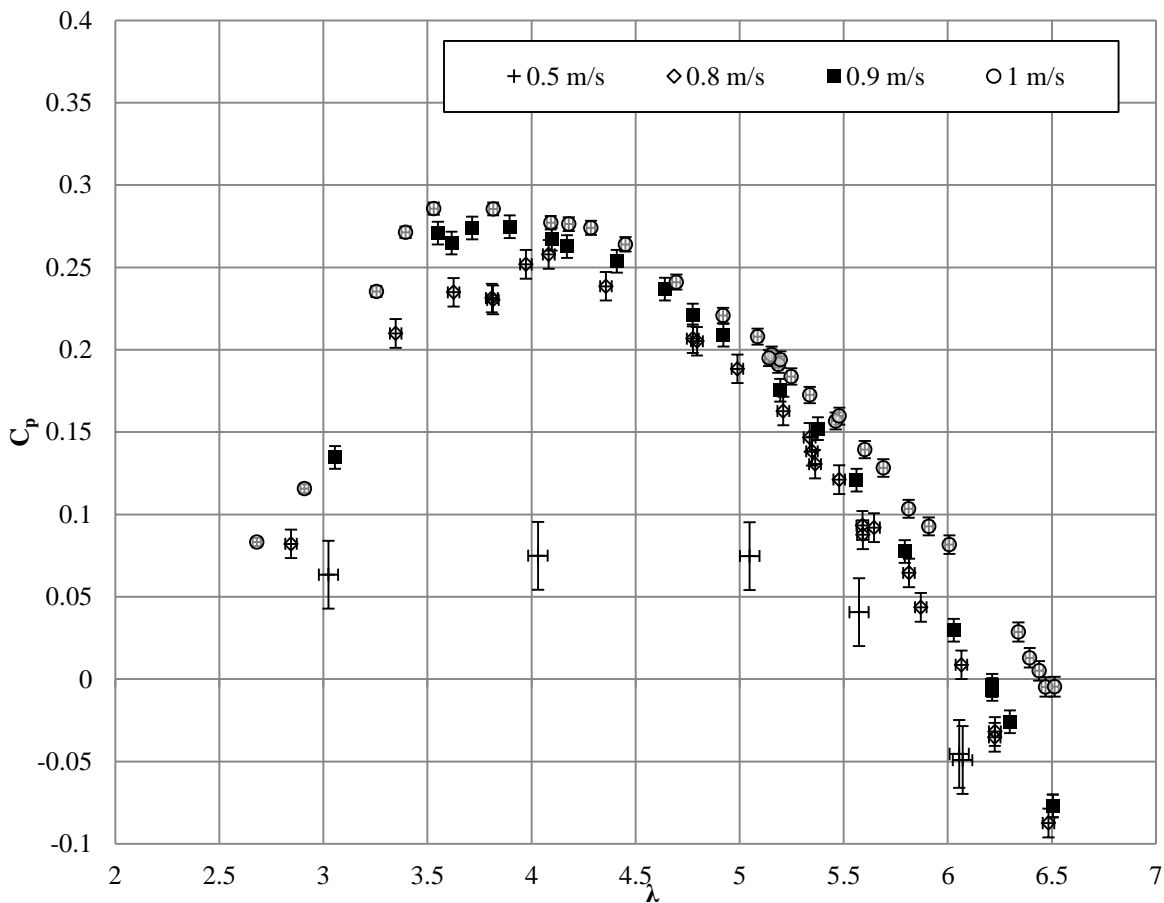


Figure 3-5. $C_P - \lambda$ curve for varying inflow speeds.

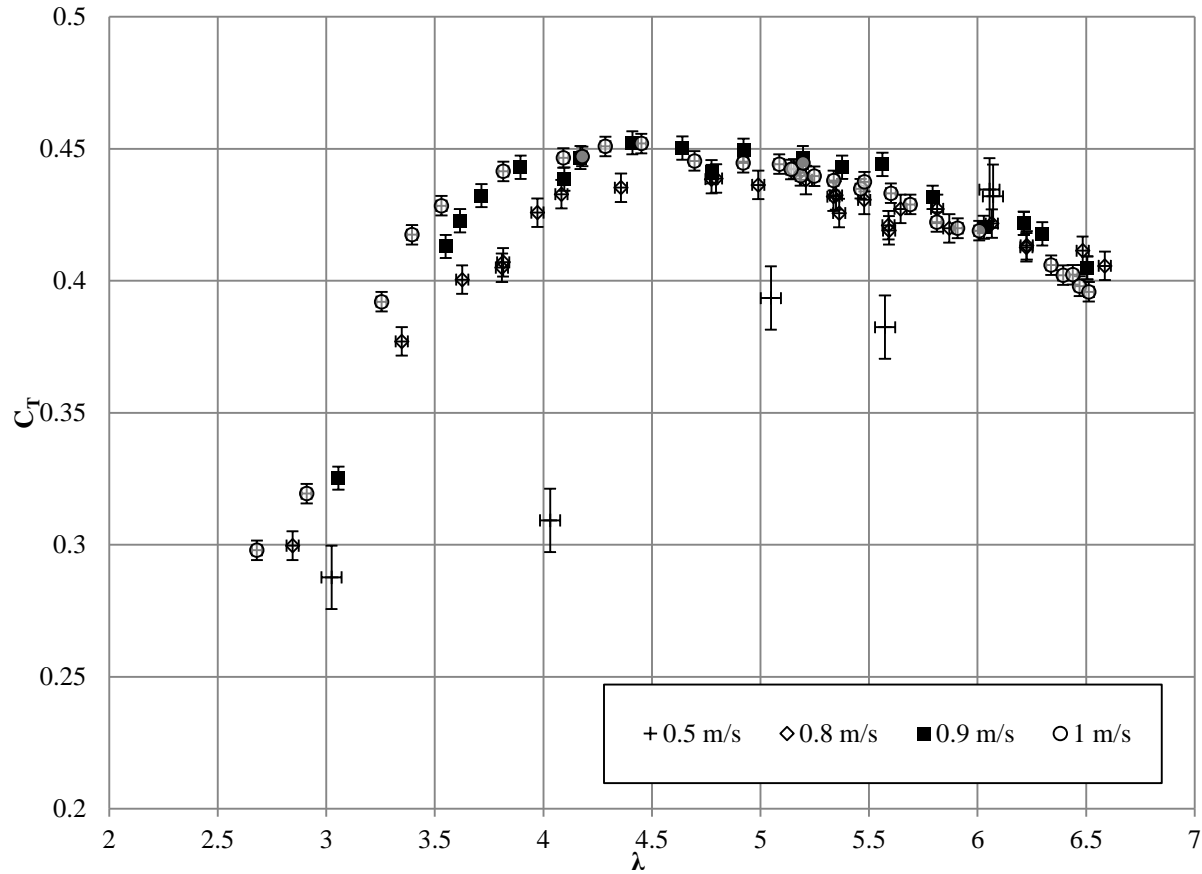


Figure 3-6. $C_T - \lambda$ curve for varying inflow speeds.

Figure 3-5 presents a general trend for each of the four tow velocities. In general, the efficiency (C_P) of the rotor increased with increasing λ and with increasing tow velocity, peaking around $\lambda = 4.08$ for the 0.8 m/s tests, 3.90 for the 0.9 m/s tests, and 3.53 for the 1 m/s tests. The efficiency of the rotor presented here is below Betz limit of 0.59 [46], which is thought to be due to the non-optimal pitch setting of the blades and the turbine operating at low Reynolds numbers. From Figure 3-6, C_T peaked at approximately $\lambda = 4.4$.

Figure 3-7 and Figure 3-8 show the axial and radial root bending moment coefficients, C_{M_y} and C_{M_x} , respectively.

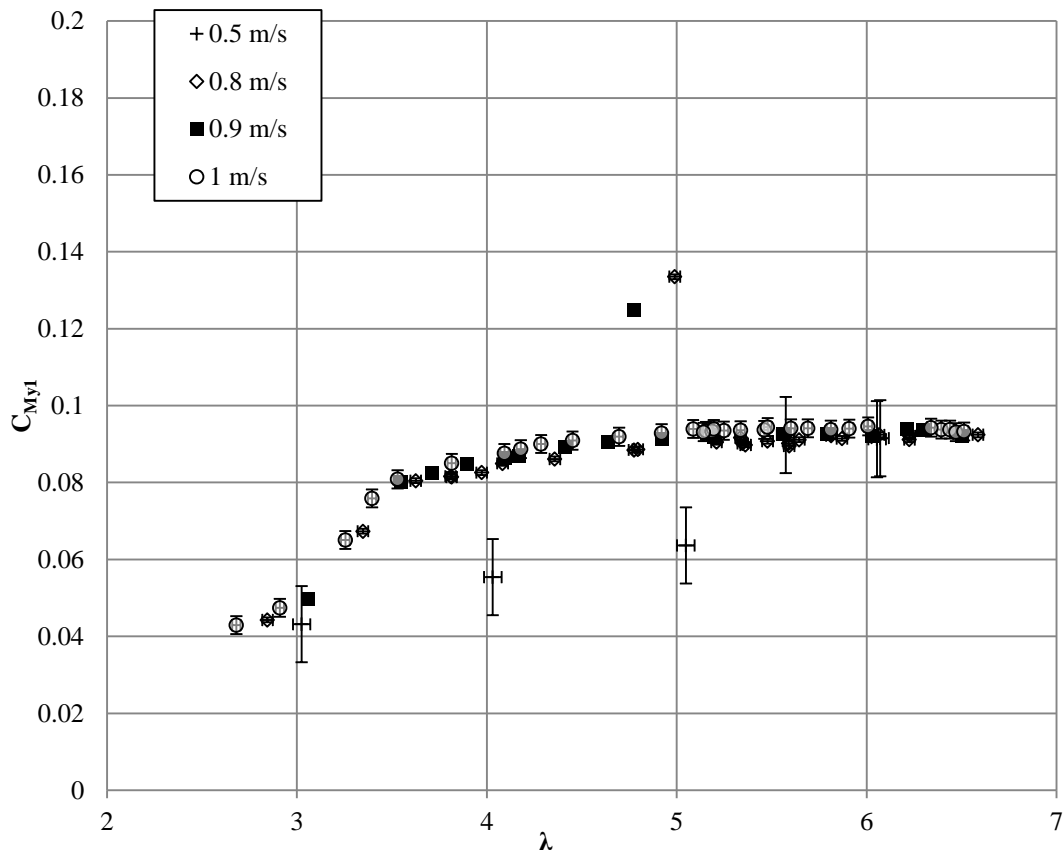


Figure 3-7. $C_{My} - \lambda$ curve for varying inflow speeds.

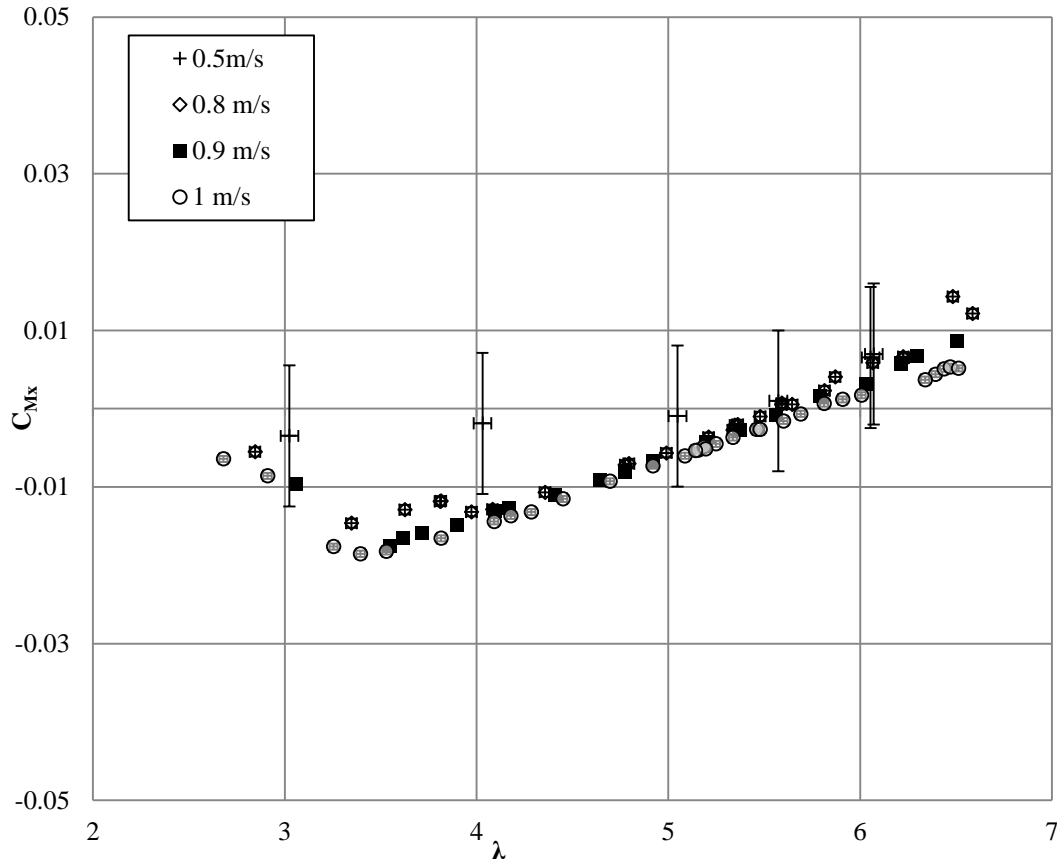


Figure 3-8. $C_{Mx} - \lambda$ curve for varying inflow speeds.

From Figure 3-7, the coefficient of axial bending moment followed a similar trend to the thrust coefficient, as expected, as it is a measure of the bending load in the axial direction at the blade root. From Figure 3-8, the coefficient of radial bending moment reached a maximum of 0.014 at a λ of 6.5. In this case, some of the C_{Mx} values were negative because the bending moment in the radial direction at the blade root was counter to the direction used in the instrument calibration, giving negative readings.

Figure 3-9 shows the thrust forces on the rotor as a function of both inflow velocity and rotational velocity.

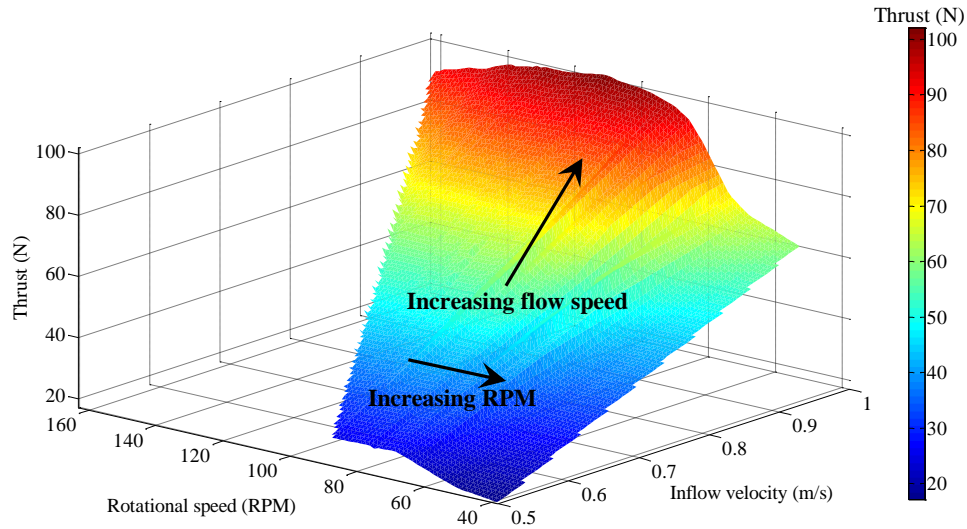


Figure 3-9. Thrust force on rotor as a function of inflow velocity and rotational velocity.

From Figure 3-9, the thrust loads are a strong function of inflow velocity, increasing from 20 N at a velocity of 0.5 m/s to over 100 N at an inflow velocity of 1 m/s, an increase of 80%. However, the loads do not appear to be as strongly influenced by the rotational speeds. For an inflow speed of 0.8 m/s the thrust loads increase from a minimum of 57 N at a rotational speed of 55 RPM to a maximum of 64 N at a rotational speed of 95 RPM, an increase of 11%. These trends are important in the consideration of influential design parameters for the structural design of BT tidal turbine blades.

The outlying data for the 0.5 m/s tests is thought to be due to low Reynolds number operation degrading the lift and making the airfoil more sensitive to flow phenomena. The consideration of Reynolds numbers during the tests is important, particularly when comparing these test results to those of a numerical performance prediction tool. Figure 3-10 shows the Reynolds numbers of the tests, taken at 70% chord.

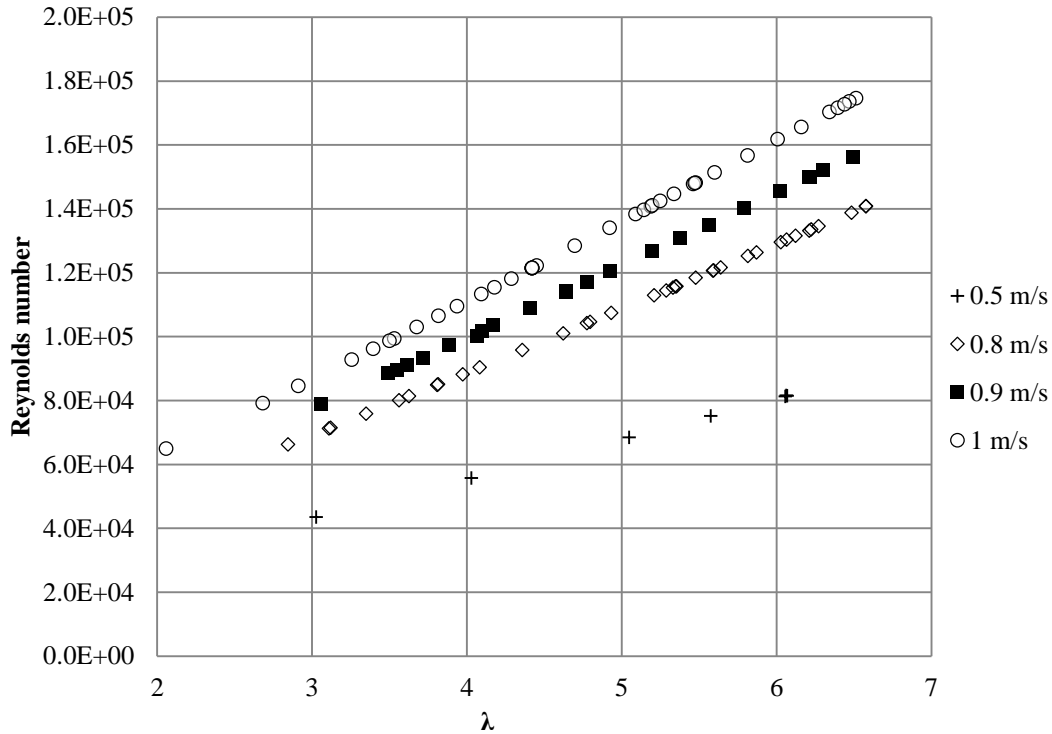


Figure 3-10 Chord-Reynolds numbers

As shown in Figure 3-10, for the 0.762 m diameter turbine tested at Strathclyde, operating at a constant 125 RPM over a range of flow speeds from 0.8 to 1.3 m/s, the chord Reynolds number ranged from 7×10^4 to 2.7×10^5 , based on blade span-wise chord lengths (maximum chord length of 0.0637m and minimum of 0.0317 m).

3.1.4 Uncertainty

The combined uncertainty for each of the performance metrics and the uncertainty in the measurements made with the calibrated instruments were quantified. The precision uncertainty values for each measured variable are given in Table 3-1. This section shows results for the 1 m/s test set, however, similar analysis was done for all tests.

Table 3-1. Precision uncertainty values, from calibration

Variable	Mean value	Uncertainty values		
		Precision	Bias	Combined
Q (Nm)	6.799	0.067	0.043	0.080
F_T (N)	83.98	0.680	0.029	0.681
M_y (Nm)	3.599	0.025	0.016	0.030
M_x (Nm)	1.987	0.025	0.020	0.032

Table 3-2 gives the bias uncertainty values used in the propagation of uncertainty for the performance metrics.

Table 3-2. Bias uncertainty values

Variable	Uncertainty
V_{inf} (ms^{-1})	0.003
W (rad/s)	0.022
Density (kgm^3)	0.021
Radius (mm)	0.5
Gravitational constant (ms^{-2})	0.001

Figure 3-11 shows the combined uncertainty in C_P , C_T , C_{My} and C_{Mx} as a function of tip speed ratio, λ , and Figure 3-12 shows the percentage uncertainty in C_P , C_T , C_{My} and C_{Mx} , for the 1 m/s test case.

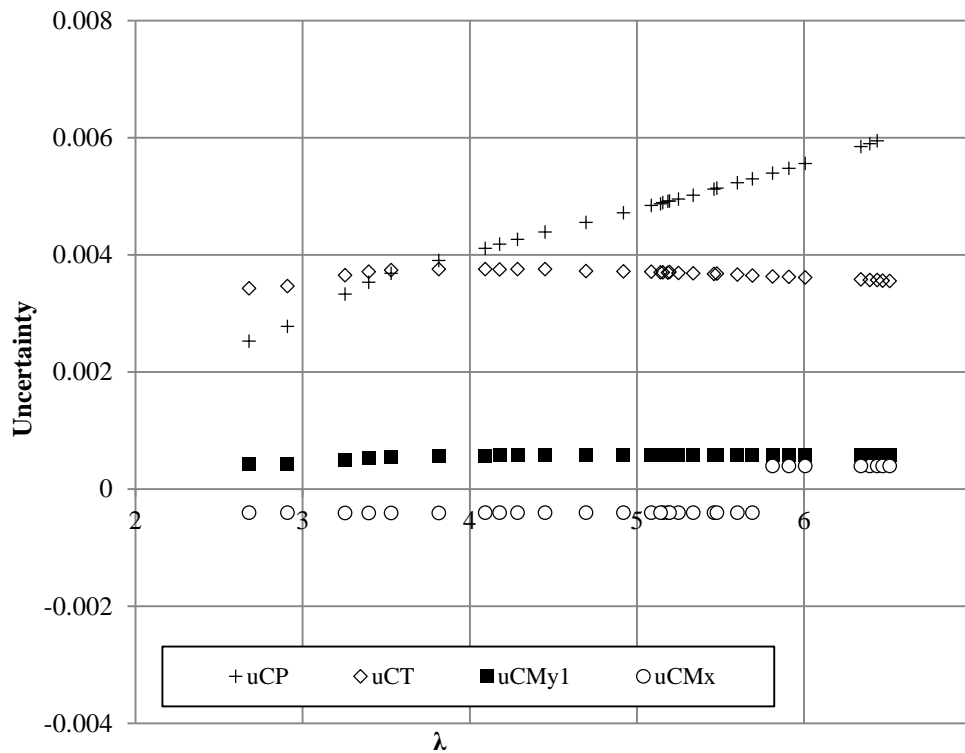


Figure 3-11. Combined uncertainty for calculated parameters.

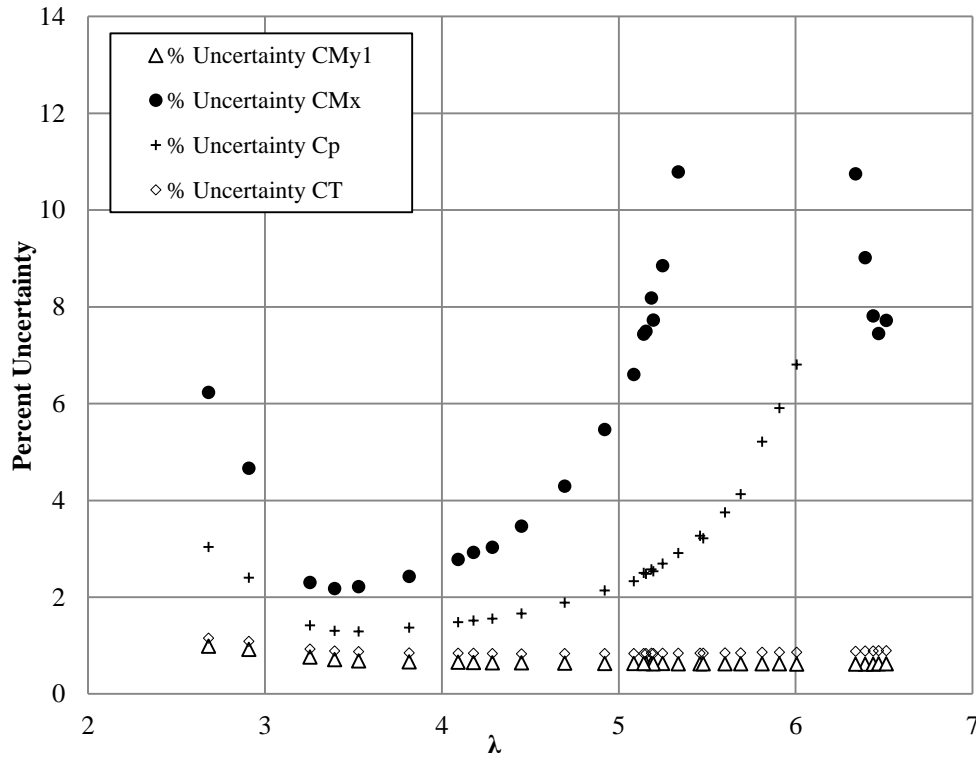


Figure 3-12 Percentage uncertainty for calculated parameters.

From Figure 3-11, the combined uncertainty in C_T , C_{My} and C_{Mx} were relatively constant. However, the combined uncertainty in C_P increased linearly with λ due to the linearly increasing rotational speed, which is multiplied by the measured torque to calculate the power capture.

The uncertainty in C_T was consistently under 1.7%, and the uncertainty in C_P was less than 5% for tests between $\lambda=3$ and $\lambda=5$. However, the percentage uncertainty in C_P was high at the extremes of the λ range, where C_P was small. The percentage uncertainty is estimated by dividing the combined uncertainty in C_P by the calculated C_P , therefore, as C_P approaches zero, the percent uncertainty approaches infinity. Although numerically this calculation of percent uncertainty is accurate, realistically, based on Figure 3-5 and Figure 3-11, the actual uncertainty in the calculated quantity did not increase drastically over the range of λ . A similar trend was found for C_{Mx} , where the percent uncertainty approaches infinity as the value of C_{Mx} approaches zero.

The uncertainty in C_{My} was less than 1.4% for over 93% of the tests done, however, C_{Mx} had an uncertainty of over 15% for 37% of the tests done. From Table 3-1, the combined uncertainty in the calibration of the radial blade root bending moment, C_{Mx} , and the axial blade root bending moment, C_{My} ; were of the same order of magnitude, however, the measured radial bending moments were small, making the percentage uncertainty high.

From Figure 3-5 to Figure 3-8, the error bars for the 0.5 m/s tests are significantly greater than those at higher flow speeds. This is because, from the propagation of uncertainty, the lower inflow velocity on the denominator of the equation equates to a greater error.

To investigate the repeatability of the test program, five test runs were repeated. The standard deviations of C_P , C_T , C_{M_x} , C_{M_y} and λ for 5 repeated tests, done with an inflow velocity of 1 m/s and rotor velocity of 110.7 RPM are given in Table 3-3, as well as the minimum uncertainty for each of the calculated parameter.

Table 3-3 - Results of the repeatability analysis.

Performance characteristic	Standard deviation	Minimum uncertainty
C_P	0.0013	0.0044
C_T	0.0017	0.0039
λ	0.0014	0.0077
C_{M_x}	7.5e-5	0.00038
C_{M_y}	1.7e-4	0.00063

The standard deviation of the repeated values was consistently lower than the minimum uncertainty. This indicated that the experimental scatter was within the uncertainty bounds of the experiment, providing confidence in the repeatability of these tests.

4 STRUCTURAL MODEL

Altair® Hyperworks RADIOSS® finite element software was used to develop structural models of the laminate plates and composite blades. These FEMs were verified by the static test results given in Section 0. Results of these verifications are presented in this Section.

4.1 Laminate plate

4.1.1 Model setup

The HyperLaminate module in Hyperworks was used to define ply orientations (fiber angles), ply thicknesses, and fiber and matrix material properties. COMPG first order 4-node CQUAD4 2D shell elements were assigned to the 2D laminate, each layer with a given ply thickness and fiber angle, and a MAT8 material model was used.

The following assumptions were made in all FEM models discussed herein:

- A. No inter-laminar shear between ply layers,
- B. Ply thicknesses and angles are perfect, meaning no manufacturing defaults are considered,
- C. 0% void content.

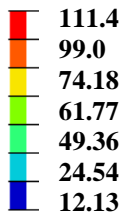
Material properties used in the laminate plate FEM are given in Table 2-1.

4.1.2 Mesh convergence study

Elements of 2 mm were used, chosen based on a mesh convergence study which showed this element size produced converging results within reasonable computational time. A total of 16200 elements were used, with edge lengths of 2 mm, which was chosen based on a mesh convergence study which showed that elements with edge lengths less than 3 mm long produced converging results within reasonable computational time.

4.1.3 Results of verification

Figure 4-1 shows the FEM displacement for the laminate plate with 3 layers, an average thickness of 2.72 mm as measured by a CMM, and a layup of $[30^\circ, 0^\circ, 30^\circ]$ with a 25 N tip load.

Contour Plot Displacement (z) in mm

Max= 111.4
Grids 674667
Min= 0.0

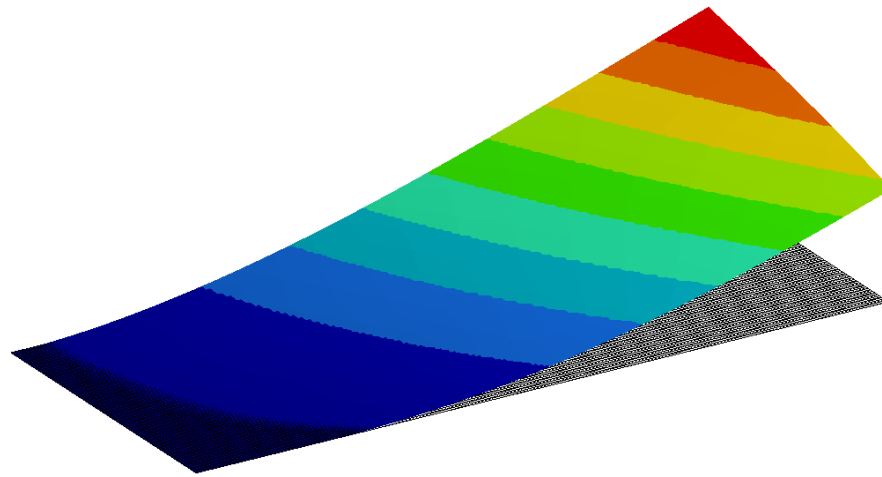
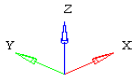


Figure 4-1. FEM of BT laminate plate bending displacement, with 25 N tip load

From the contour plot of the displacements of the laminate, the z -displacement of the free end of the plate varied in the y -plane. This is a clear indication of twist in the plate. With a 25 N load applied, the maximum tip displacement was 111.4 mm, with a tip twist of 10.64° , for this layup and laminate thickness.

Figure 4-2 and Figure 4-3 show results obtained for the $[30^\circ, 0^\circ, 30^\circ]$ laminate test samples compared to a FEM with an average thickness of 2.72 mm. The tip displacement is the maximum displacement of free end of the plate, relative to the initially unloaded plate.

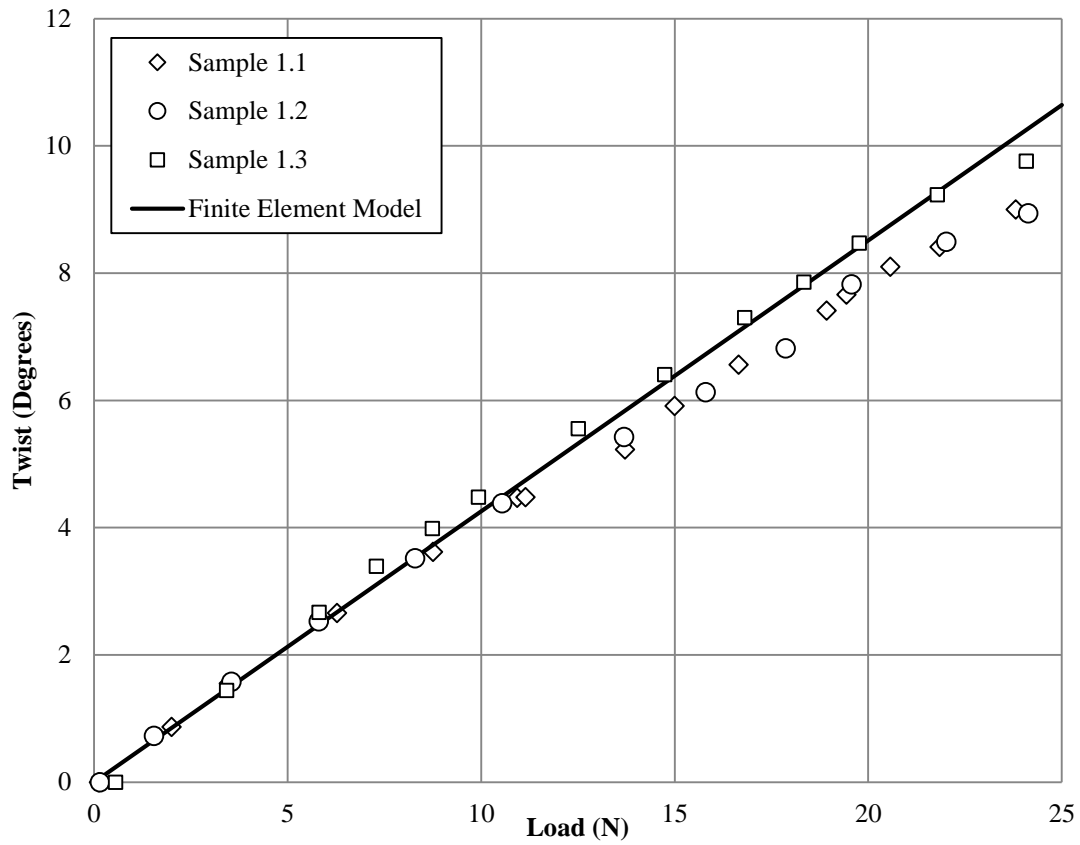


Figure 4-2. Twist vs. load for the experimental results

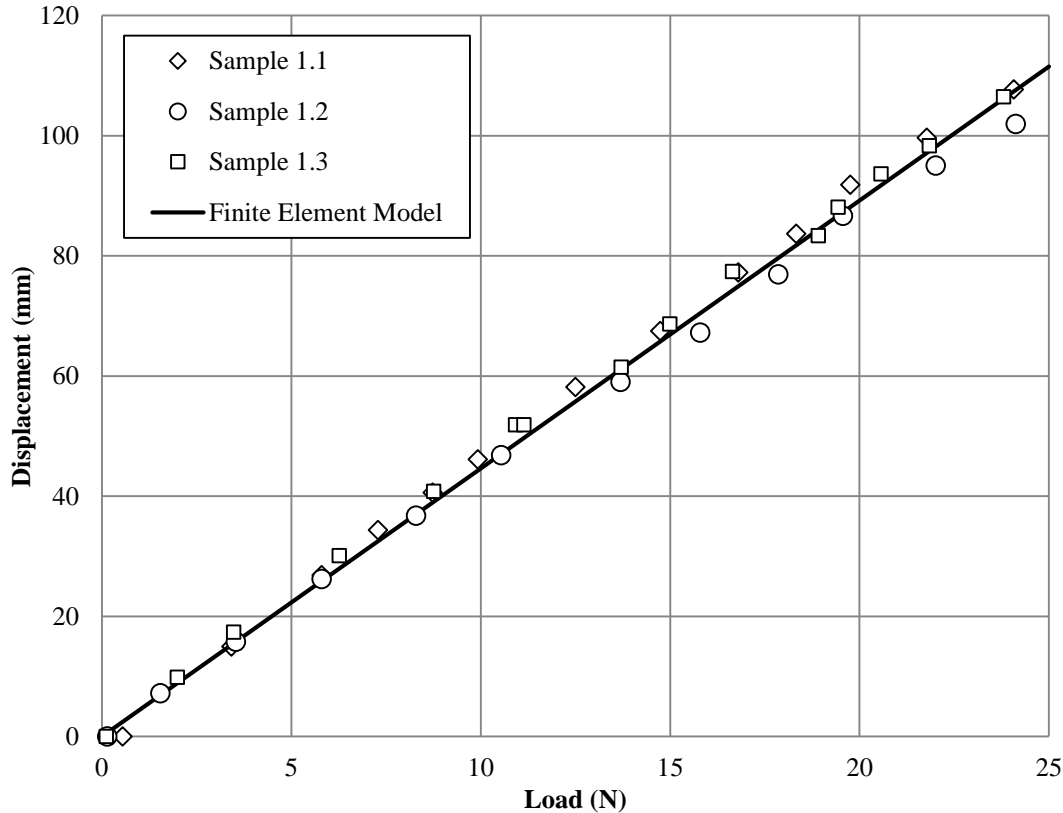


Figure 4-3. Load vs. displacement for the experimental results

The FEM was within 9% of the experimental results, at maximum load (worst case scenario), when predicting twist, and within 2% when predicting displacement. The uncertainty in all the components was found to be less than 5% over the range of loads applied in the experiment. However, possible additional sources of error between the test samples and the FEM include:

- Random uncertainty in the experimental setup; for example, imperfections in the clamping mechanisms and slight offsets in the location of the point load,
- Variations in the ply angles ($\pm 5\%$ in the ply angles significantly effects the sample deformation),
- Variations in the mean thickness of the plate samples (each sample has a slightly different measured mean thickness).

With the high level of accuracy in the experimental results and the close match between the FEM and experiment, the FEM was considered verified.

4.2 Composite blade

The implicit finite element code, Altair[®] Hyperworks RADIOSS[®] [47], was used to develop a FEM of the composite blade previously tested. This FEM software can be executed from within a Mathworks MATLAB[®] script, enabling the BEMT and FEM to run iteratively through a MATLAB[®] interface, as presented in Section 0.

The blade FEM was verified by the static test results given in Section 2.2. Results of these verifications are presented in this Section.

4.2.1 *Model setup*

It was assumed that there were no inter-laminar shear between ply layers, the ply thicknesses were perfect as given by the manufacturer and there was 0% void content. Tetrahedral 3D elements were used to mesh the blade core, and COMPG 2D quadrilateral shell elements were used to model the composite skin of the blade. The ply thickness and fiber angle of the composite blade skin were defined in the HyperLaminate module. It was assumed that no slipping occurred between the blade core and the composite surface, and the interface nodes between the 2D and 3D meshes were tied. The blade root, including attachments such as bolts and inserts, were not considered in the model as they were assumed to be rigid and not contribute to the BT response of the blade.

Material properties for the blade FEM are given in Table 2-4. An anisotropic constitutive material model, MAT8, was implemented in RADIOSS to model the composite skin. This material model considers the material properties in the longitudinal (fiber) and transverse (matrix) directions in both tension and compression. Modeling foam materials is more complex, as they exhibit non-linear stress-strain relations after an initial linear deformation period [48]. A preliminary FEM was used to estimate the maximum expected strain in the blade core at approximately 0.006 m/m. Based on typical stress-strain curves for epoxy foams [48], this strain level indicated that the epoxy foam core was entirely in the linear region of the stress-strain curve. Thus, the foam was modeled as an isotropic linear elastic material, MAT1. Foam materials also have properties which are a function of the material density [49]. Therefore, based on interpolation between the linear region of two epoxy foam stress-strain curves (one for a higher density foam [50], and one for a lower density foam [48]), the material properties were estimated for the 250 kg/m³ foam. It was also assumed that the density of the foam was constant over the entire blade.

The usage of thin shell elements can lead to limitations in capturing delamination effects and out-of-plane stresses for thick composite materials, which are important in fracture mechanics [51]. However, for the thin composite material used here, a shell element formulation was chosen for computational efficiency, since through-thickness effects are expected to be negligible.

4.2.2 *Mesh convergence study*

A mesh convergence study was performed to investigate the sensitivity of the model to element size, and to choose an element size that has good convergence but reasonable computational time. Figure 4-4 shows the computational time for the FEM as a function of the element size.

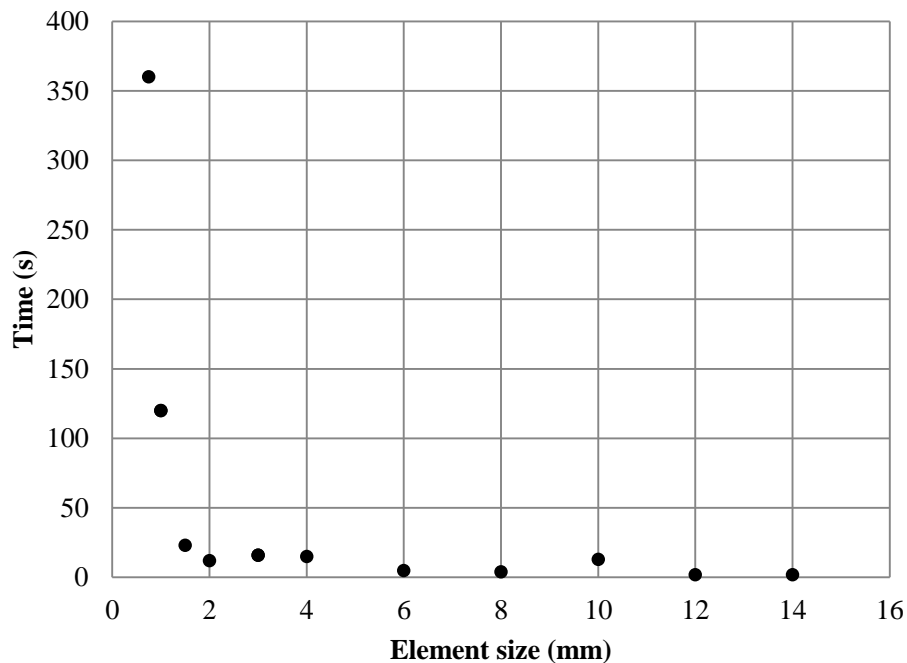


Figure 4-4 Finite element convergence study: Computational time

As the element size increases, the computational time decreases approximately exponentially. For elements of 1.0 mm and smaller, the computational time is over 2 minutes. Figure 4-5 shows the maximum bending displacement of the blade, and Figure 4-6 shows the normal tensile stress at a fixed geometrical location near the root of the blade as a function of element size.

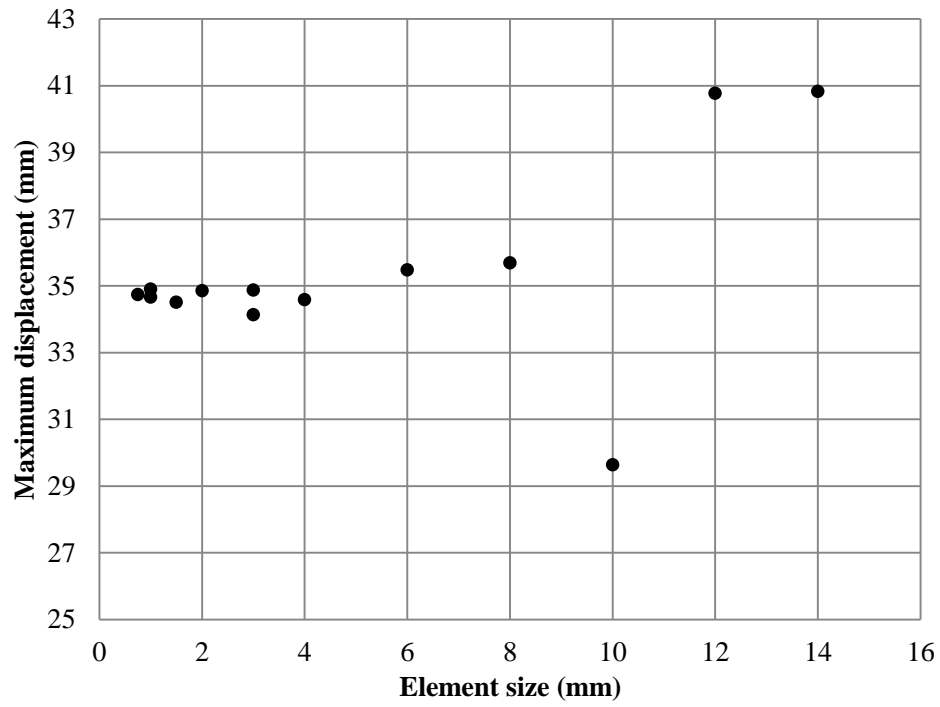


Figure 4-5 Finite element convergence study: Bending displacement

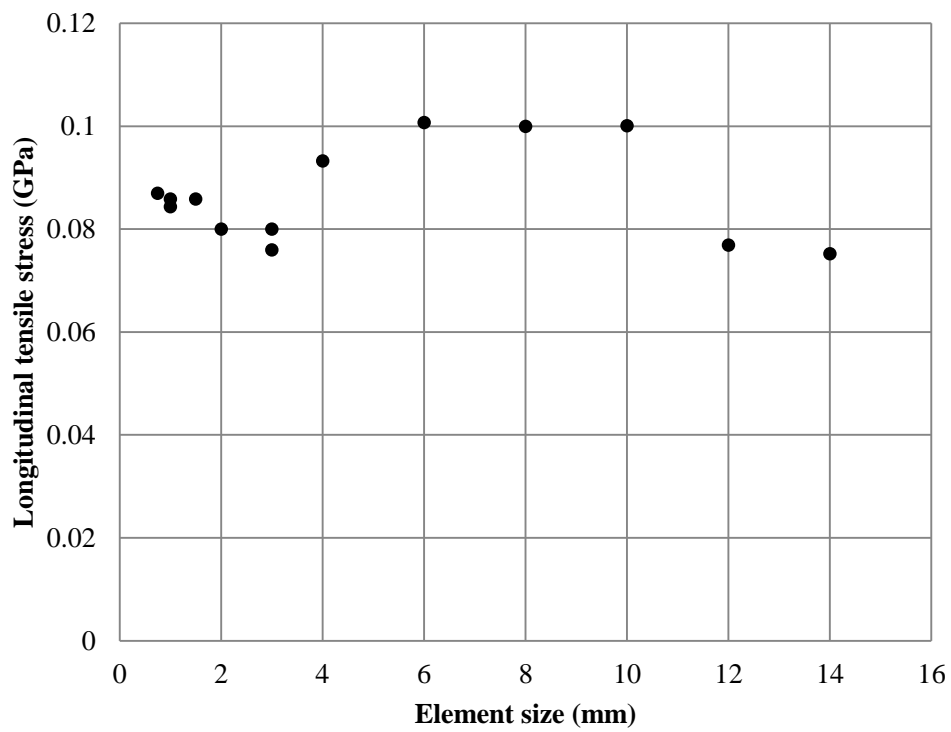


Figure 4-6 Finite element convergence study: Longitudinal tensile stress

For elements of 3 mm and smaller, the displacement and stress appear to converge. As the element size increases beyond 4 mm, the results become less stable. However, the model results are clearly not highly sensitive to element size, which means that the designer can have more flexibility over varying element size, to within reasonable bounds. In this case, 1.5 mm elements were chosen for the remainder of the work, as they require only 23 seconds for the model to run, and show converged results compared to smaller elements. Therefore, a total of 16,200 2D shell elements were used. The blade mesh is shown in Figure 4-7.

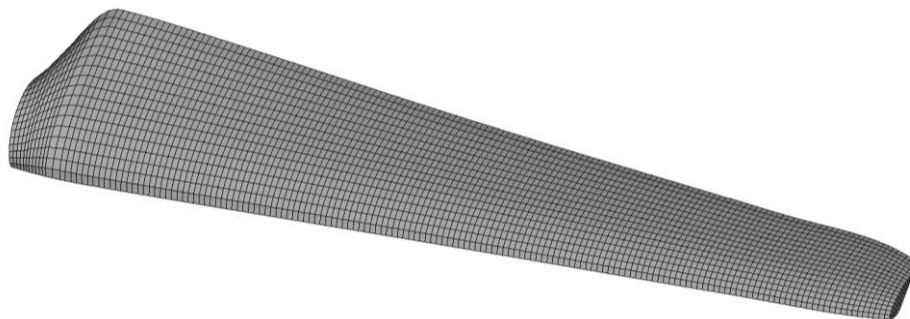


Figure 4-7 Blade mesh, 1.5 mm 2D quad elements

4.2.3 Results of verification

Figure 2-13 and Figure 2-14 show the blade bending displacement and tip twist, respectively, as a function of applied load.

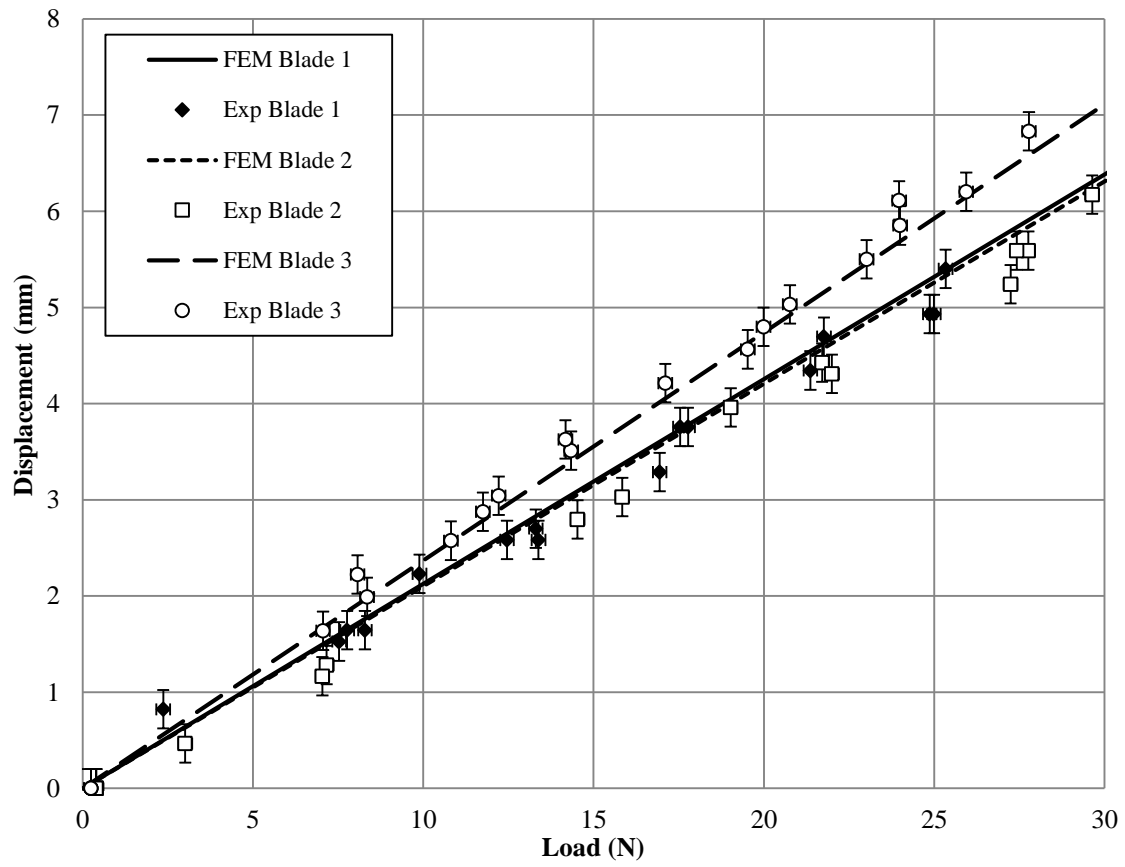


Figure 4-8 Load vs. displacement for composite blades compared to FEM

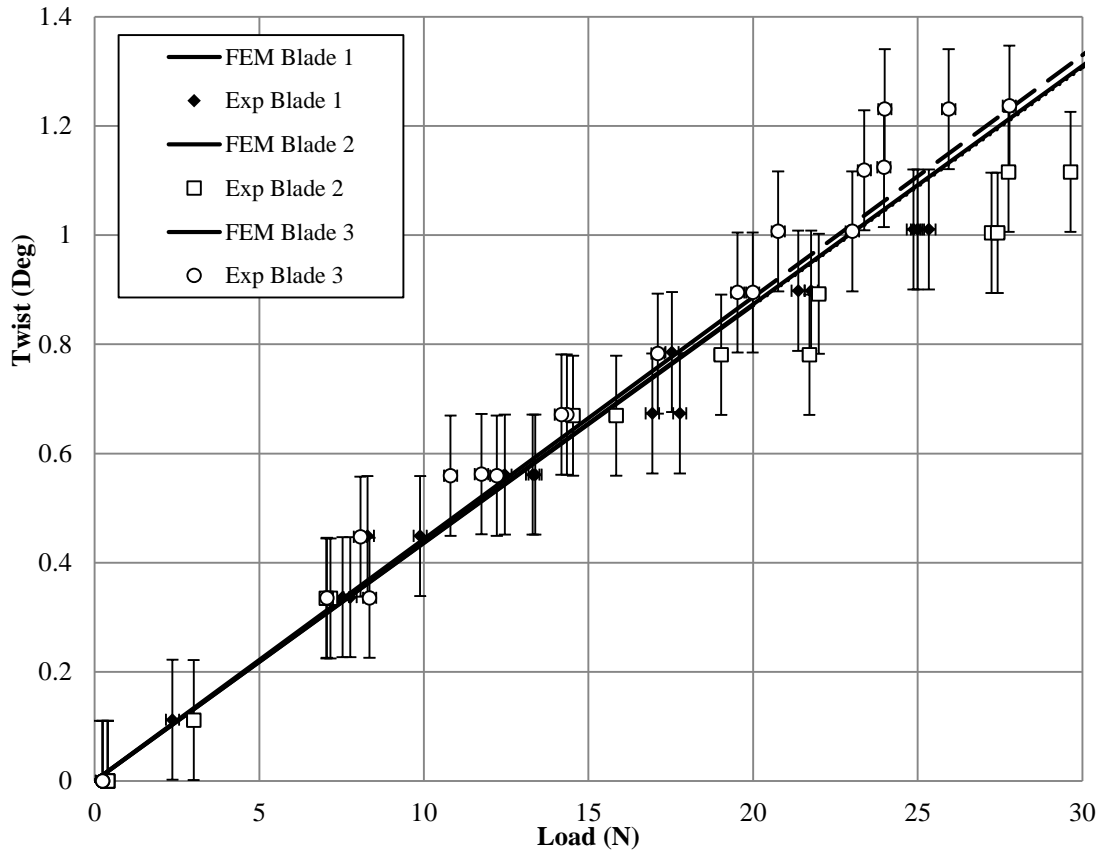


Figure 4-9 Load vs. twisting for composite blades compared to FEM

The bending displacement and tip twist of the composite blade were linear (see discussion in Section 2.2.5) and were in good agreement with the FEM; the FEM predicted the experimental blade bending response to within 5.8% and predicted the blade twisting response to within 10.7%, at maximum load (worst case scenario). The different deformation predictions for each blade were based on the slightly differing ply angles, as discussed in Section 2.2.5, which were included in each FEM.

Due to the small values of twist and the limitations in pixel accuracy (± 0.20 mm giving approximately $\pm 0.11^\circ$ uncertainty), the percent difference between the experiment and FEM was high, however, the agreement between the experiment and FEM bending displacement is considered acceptable. For larger blades, it is expected that the relative uncertainty in such experiments will be decreased as the measured twist values increase.

An aluminum 6061 blade of the same geometry was also tested in the structural test setup. Results of the aluminum blade experimental (four repeated test cases) and an aluminum blade FEM are given in Figure 4-10, and compared to the composite blade FEM.

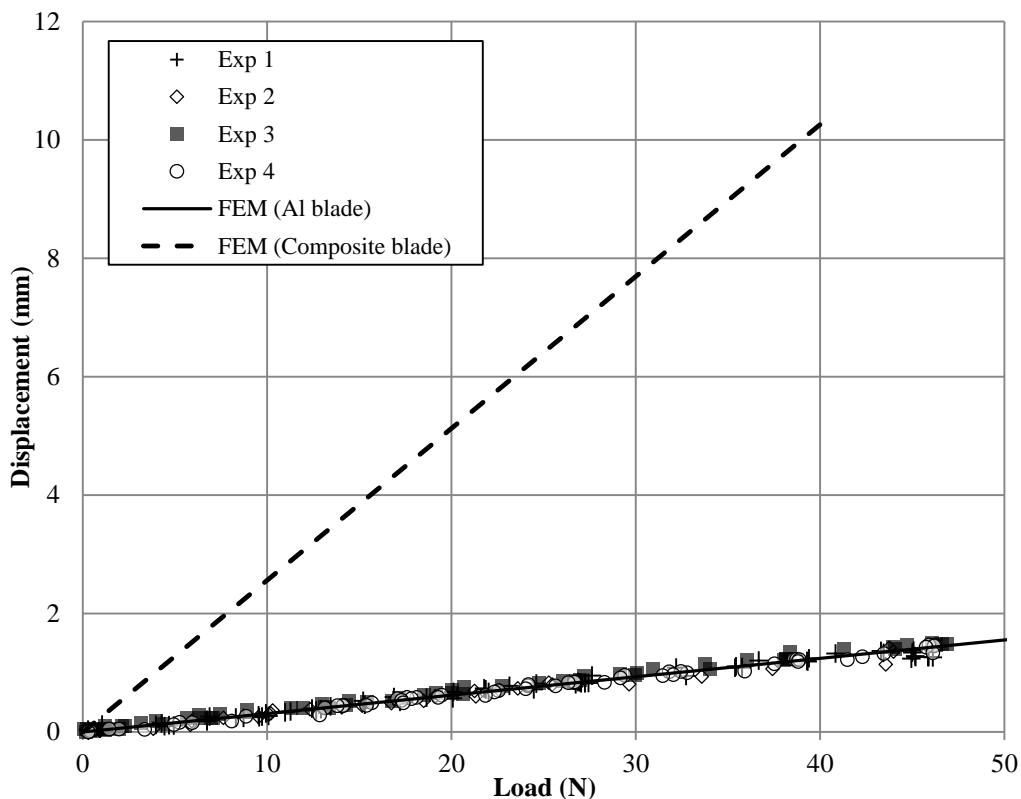


Figure 4-10 Aluminum blade displacement compared to composite displacement

The bending displacement of the aluminum blade was highly linear, with R^2 values > 0.98 , and was in good agreement a FEM using aluminum material [52].

The future tests outlined in Section 8.1 were designed to compare the hydrodynamic response of BT blades to rigid blades, and hence assumed that the aluminum blades did not deform. It was therefore important to verifying this assumption. For a maximum applied tip load of 45 N, the bending displacement of the aluminum blades was less than 1.5 mm. Compared to the FEM bending displacement of the composite blade under the same load (over 11 mm), the aluminum blade was effectively rigid (less than 15% of the bending displacement under the same applied load).

5 HYDRODYNAMIC MODEL

A BEMT code, developed for HATT by Nevalainen [53] in a similar method as Orme [54], was used to simulate the thrust and torque on a turbine blade. The BEMT was verified experimentally for rigid blades using several data sets, with results presented in this section.

5.1 Batten and Pinon verification

In order to use BEMT, it has to be shown to be capable of sufficiently predicting rotor performance. An initial verification for the BEMT developed by Nevalainen was undertaken using two datasets: Gaurier *et al.* [55] and Bahaj *et al.* [56]. Airfoil data for these models was obtained using XFOIL [57] at the appropriate Reynolds numbers (as was done by [58]), and the blade and turbine geometries are given in the respective publications. Both turbine blades were modeled with 100 blade elements to ensure converged results.

Figure 5-1 and Figure 5-2 show C_P and C_T as a function of λ for the Bahaj *et al.* experiment and BEMT, and Figure 5-3 shows C_P and C_T as a function of λ for the Gaurier *et al.* experiment and BEMT.

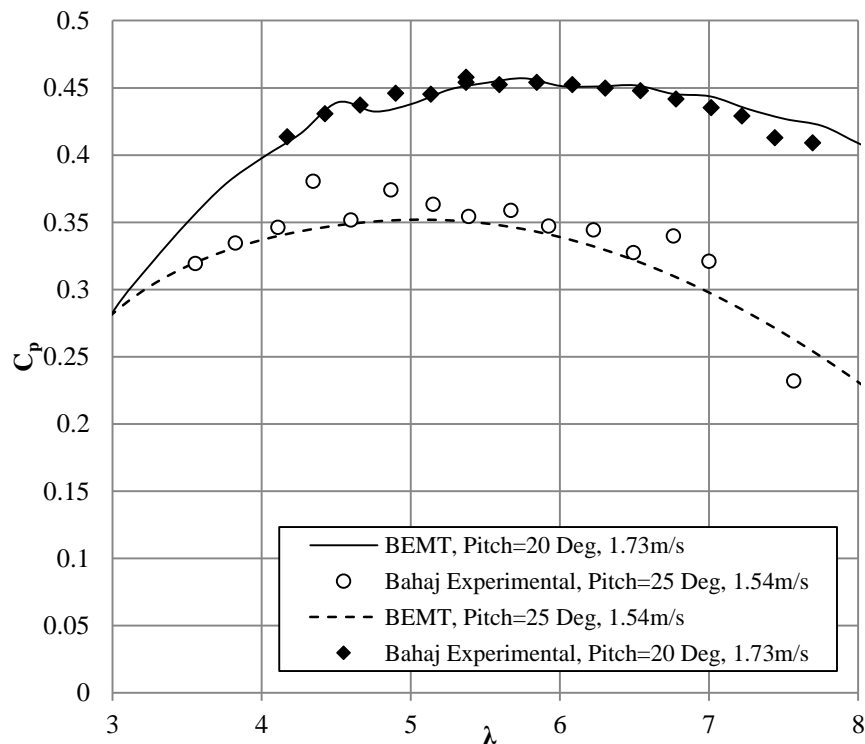


Figure 5-1. $C_p - \lambda$ curves for Bahaj *et al.* experiment and BEMT.

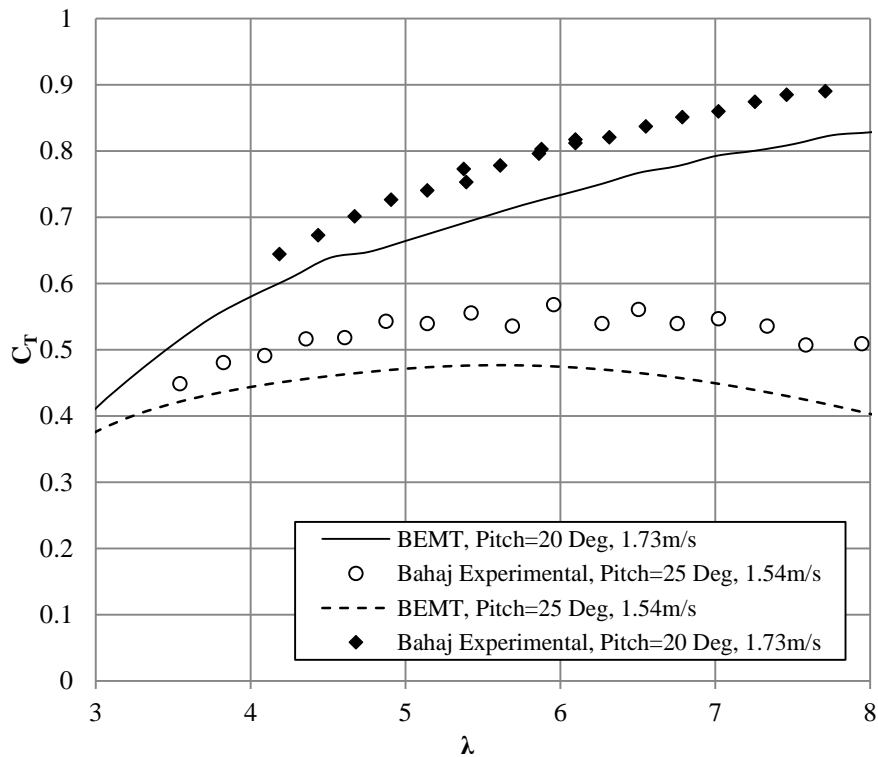


Figure 5-2. $C_T - \lambda$ curves for Bahaj et al. experiment and BEMT.

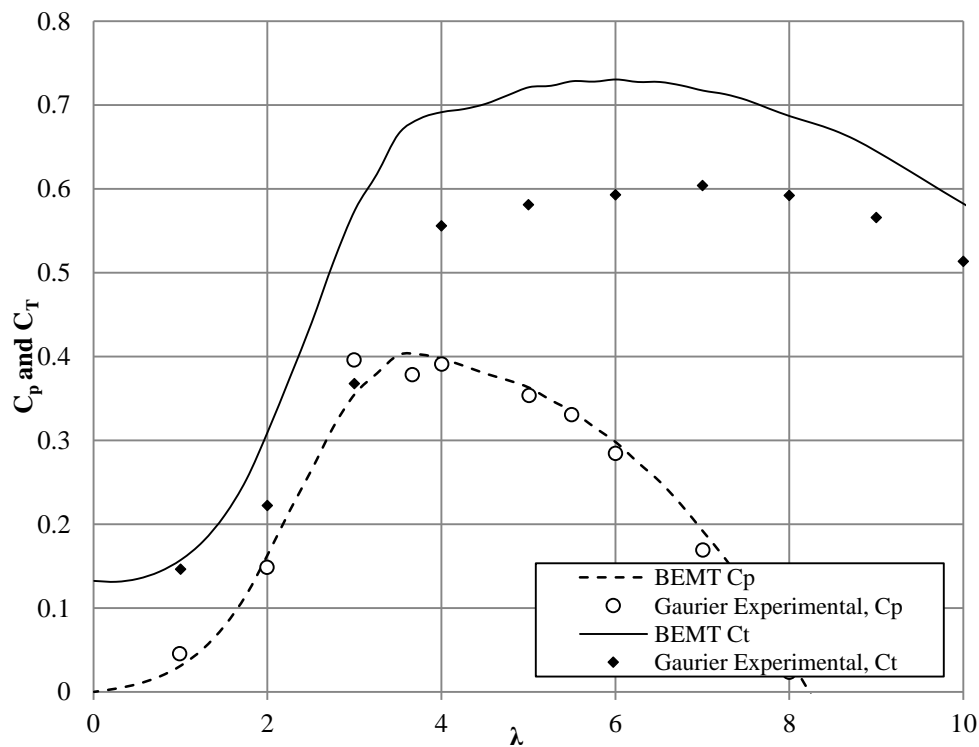


Figure 5-3. $C_p - \lambda$ and $C_T - \lambda$ curves for Gaurier et al. experiment (0.8 ms^{-1} and 5% turbulence) and BEMT results.

Verification of the BEMT with these data sets showed that it predicted the performance of the Batten *et al.* tidal turbine in steady flow conditions well, but showed a slight discrepancy between the Gaurier *et al.* experimental thrust data and the BEMT thrust which is thought to be due to a higher turbulence intensity in the IFREMER flume (with a turbulence intensity of 5%) than in the steady flow airfoil data calculated in XFOIL (airfoil data was estimated using XFOIL with an NCRIT value of 5, simulating a low turbulence test case) .

5.2 NREL S814 verification

This section presents a comparison of the BEMT tool to the rigid blades tested (381 mm rotor radius, 89 mm hub radius, and 292 mm blade length), with turbine geometry given in Figure 3-1. Togneri *et al.*, at Swansea University [59], obtained lift and drag data for the NREL S814 airfoil in a flume at a Reynolds number of 5×10^4 . This data was used to model the airfoil used in these tests.

5.2.1 Element convergence study

A convergence study was done to determine the minimum number of blade elements that produces a converged BEMT solution in minimal computational time. For an inflow velocity of 0.8 m/s, and TSR of 4, Figure 5-4 and Figure 5-5 show the results of the convergence study.

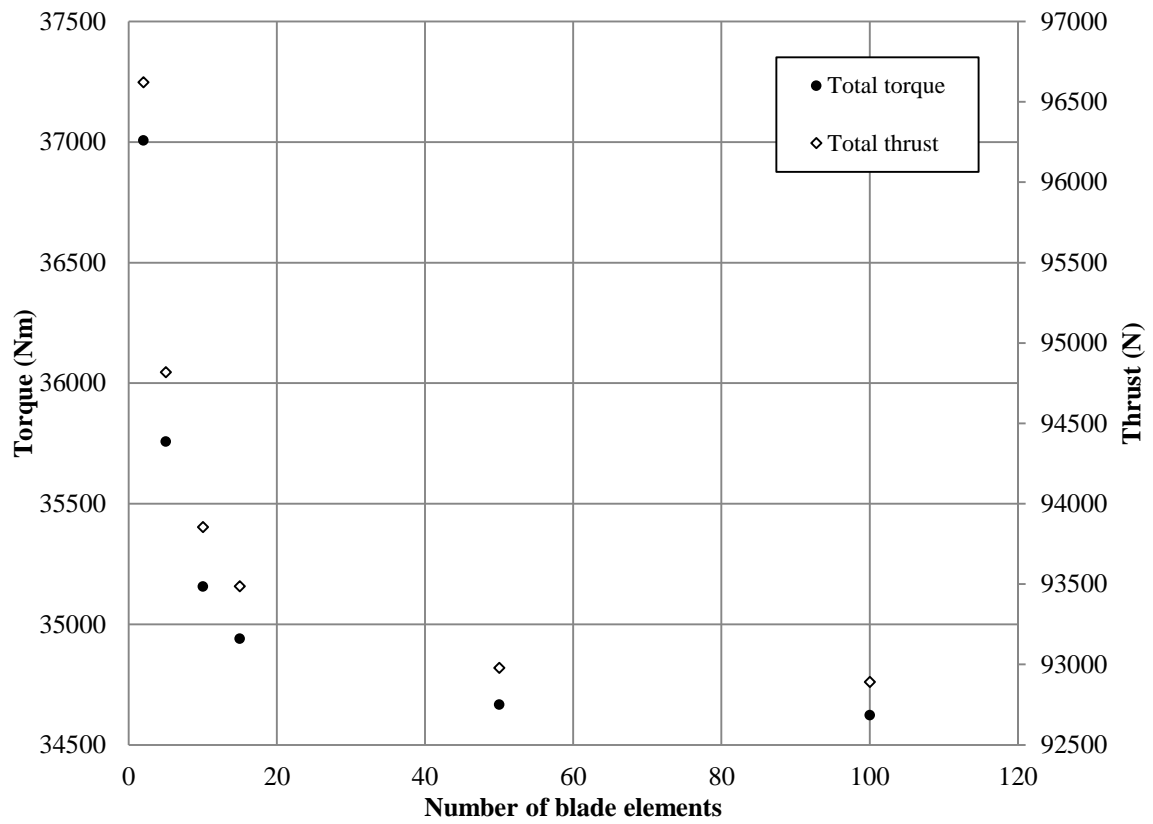


Figure 5-4 Thrust and torque on the turbine rotor as a function of number of blade elements

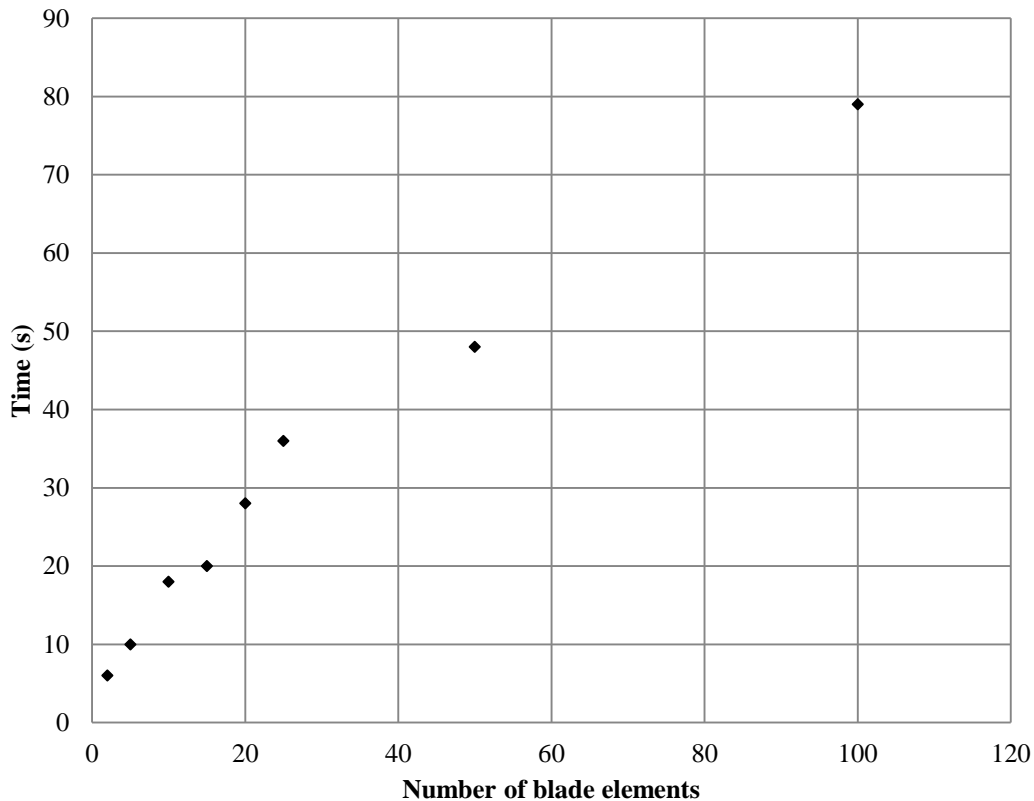


Figure 5-5 Computational time as a function of number of blade elements

The torque and thrust converged for more than 20 blade elements, with less $< 0.35\%$ difference in thrust between 20 and 100 blade elements. However, there was only a 0.87% difference in thrust results between 10 elements and 100 elements, and a 77% decrease in computational time using 10 blade elements compared to 100 elements. This 0.87% difference was considered to be insignificant, as it correlates to less than 1% difference in torque, which is within the normal measurement error.

5.2.2 NREL S814 verification

Using the Swansea airfoil data in the BEMT, with the inclusion of correction factors previously mentioned, Figure 5-6 and Figure 5-7 show the results of the towing tank tests for an inflow speed of 0.8 m/s with a pitch setting of 28.88° , compared to the BEMT results.

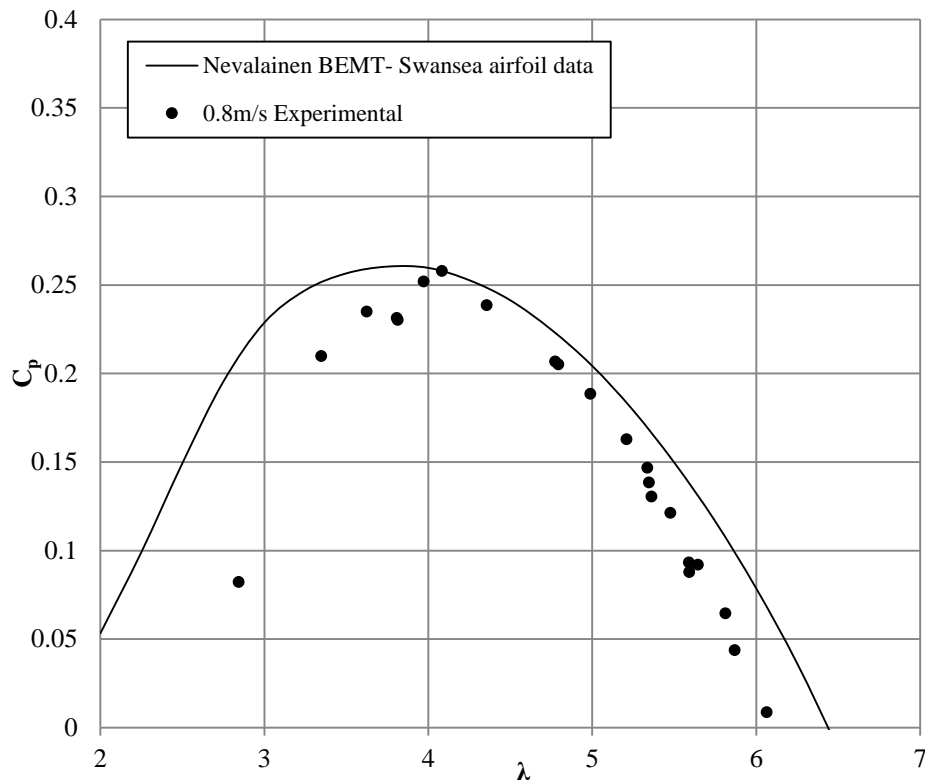


Figure 5-6. $C_p - \lambda$ curve for NREL S814 blades (0.8 m/s) and Nevalainen BEMT, Swansea airfoil data

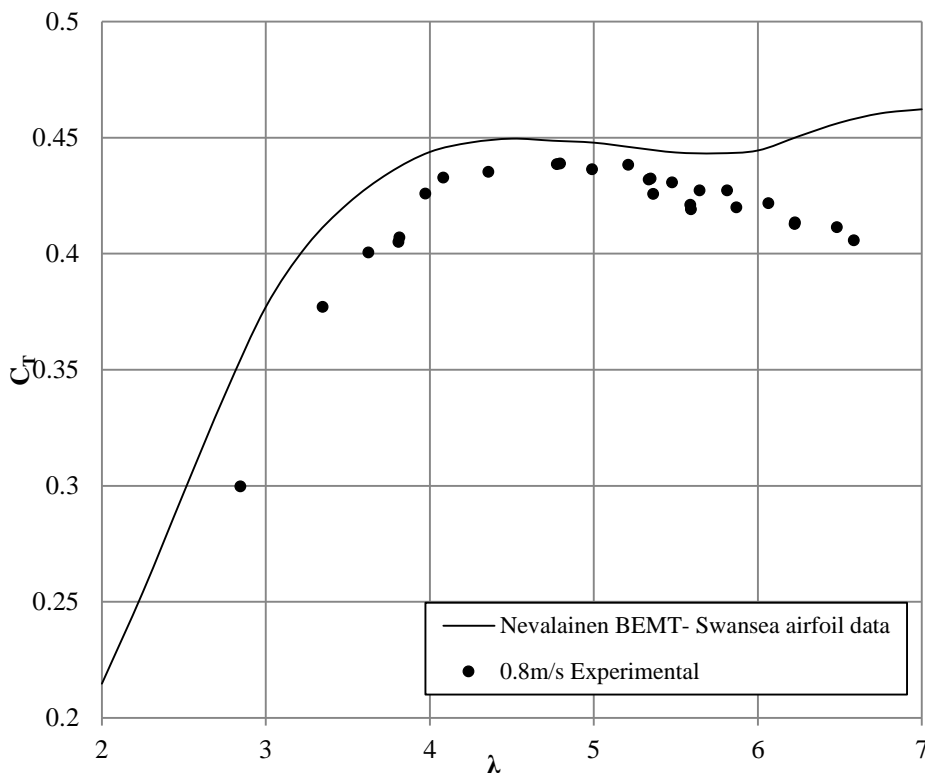


Figure 5-7. $C_T - \lambda$ curve for NREL S814 blades (0.8 m/s) and Nevalainen BEMT, Swansea airfoil data

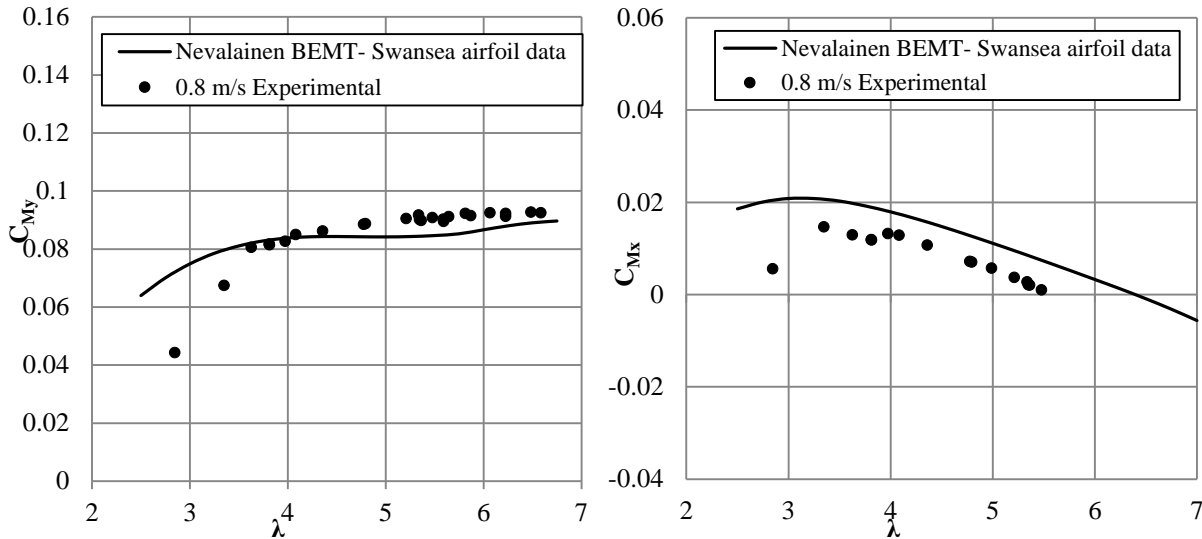


Figure 5-8. Left) $C_{My} - \lambda$ curve, right) $C_{Mx} - \lambda$ curve, for NREL S814 blades (0.8 m/s) and Nevalainen BEMT.

In general, although there were discrepancies at low λ , the BEMT tool was able to capture the physical trends and performed acceptably for λ greater than 3.5; the prediction of C_p was accurate for λ between 3.5 and 5.5, with less than 2% difference between the BEMT and experimental C_p at the optimum λ of 4. The C_T data was slightly over predicted by the BEMT code, and was at worst off by 9% for λ greater than 3.5. As well, the BEMT tool over-predicted the axial blade root bending moment, C_{My} , at low λ s, but was within 4.4% of the experimental results for λ greater than 3.5. In general, the BEMT tool under predicted the radial blade root bending moment, C_{Mx} , but followed the same general trend. The match achieved between the experiment and BEMT is comparable to similar verifications done in the tidal energy industry [60, 61]. The over-prediction of power capture and thrust loads as λ decreases is thought to be due to the BEMT code not capturing stall effects, which degrades the lift and increases the drag of the airfoil in the actual turbine.

6 FEM-BEMT DESIGN TOOL

The BEMT code previously discussed was able to predict the performance of rigid turbine blades. However, the increased flexibility of BT turbine blades makes BEMT alone unable to predict turbine performance and necessitates a fluid-structural interaction design methodology. This section outlines the development of a coupled FEM-BEMT tool for the design of BT coupled blades, considering both the structural and hydrodynamic performance of the blades. An iterative design tool allows for the design and optimization of both the local blade structure (stresses, failure criteria, blade deformation) and the turbine globally (power output and loads) [62]

The FEM, discussed in Section 0, and the BEMT code, discussed in Section 0, were coupled loosely using a MATLAB[®] interface.

6.1 Procedure

A MATLAB[®] interface was developed to iterate between the BEMT code and the FEM. Figure 6-1 shows the process flow chart for the FEM-BEMT coupled design tool for a single iteration.

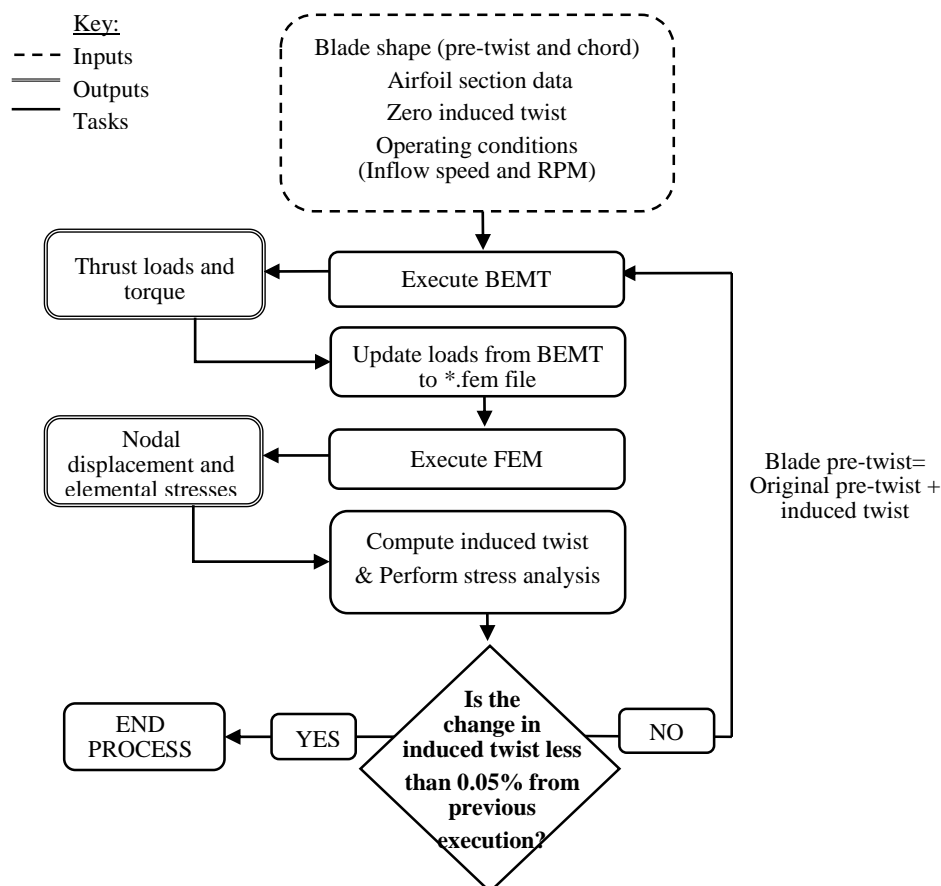


Figure 6-1 Flow chart of coupled iterative FEM-BEMT design tool.

Blade data (radial chord length and pre-twist geometry, airfoil data) and operating conditions (flow velocities and rotational velocities) were input to the design tool and the BEMT was executed to estimate the axial loads (thrust forces) and tangential loads (multiplied by radius to give torque) on each blade element along the blade span. These axial and tangential loads were then applied to nodes in the FEM. For the initial BEMT simulation, the blade had zero induced twist, $\phi_1 = 0$. The FEM was then run using the BEMT-predicted loads, and the induced twist and composite stresses were computed based on nodal and elemental outputs from the FEM in the form of ASCII files, which were processed in MATLAB[®].

HATT power capture and blade loads depend on how the lift and drag coefficients vary with α , and α depends on the flow conditions and the pre-twist geometry of the blade, β_0 . In this case, α also depends on the induced twist of the blade due to BT coupling, ϕ_1 . The induced twist predicted by the FEM was added to the pre-twist of the baseline blade, giving a new pre-twist blade geometry, $\beta_n = \beta_0 + \phi_1$, and altering α and the performance of the blade as predicted by the BEMT, leading to an iterative process between the FEM and BEMT.

It was found that convergence was well indicated by the induced twist as calculated based on the FEM displacement output. With the induced twist as the convergence criterion, a comparison to the last iteration's twist value was performed, and the iterations were executed until the induced twist of the current iteration was $< 0.05\%$ different from the previous iteration, as given by Eq. (6-1),

$$\frac{(\phi_{i,k} - \phi_{i,k-1})}{(\phi_{i,k} + \phi_{i,k-1})/2} = < 0.0005 \quad 6-1$$

where k is the iteration number. A 0.05% difference in the induced twist equates to less than 0.1% difference in the rotor thrust, which is considered within the sensitivity of the design tool.

To summarize, the following outlines the steps to running the code:

1. Input flow conditions, blade geometry, blade pitch setting, airfoil section data, and number of elements
2. Specify convergence criteria
3. Loop for velocity or TSR (do the following for each discrete flow condition)
4. Execute BEMT
5. Update *.fem file with nodal loads from BEMT analysis
6. Execute FEM
7. Analyze *.disp and *.cstr for nodal displacement, induced twist, and elemental stresses

8. Output results to *.txt file that include the following: “ Inflow speed, Rotational speed, Initial thrust, Final thrust, Initial torque, Final torque, Percent change thrust, Percent change torque, Initial C_p , Final C_p , Initial C_T , Final C_T , Maximum induced twist, Maximum bending displacement, Maximum normal-1 stress, Minimum normal-1 stress, Maximum normal-2 stress, Minimum normal-2 stress, Maximum shear stress.
9. Perform failure analysis and calculate SFs for composite stress.
10. Compare induced twist from this iteration to previous
11. If convergence criteria is not met, go back to Step 4
12. Once convergence criteria is met for this flow condition, repeat from Step 3 for all flow conditions

Although there are benefits of this design tool, there are also limitations such as:

- No aerodynamic moment considered
- Perfect VS control system
- Reynolds number effects not considered
- No dynamic simulations or fatigue analysis
- Interactions with other wind turbine parts are not simulated

6.2 Stress analysis

As a check on the durability of the composite blades, a failure analysis was implemented in the design tool. This failure analysis quantified the strength of the composite blade design based on elemental stresses in the composite material, which were output from the FEM after each iteration. Safety factors (SFs), which give the capacity of a structure to support loads before yielding, based on both the Maximum Stress failure theory and Tsai-Hill failure theory, were computed for each element in the composite FEM after each iteration. These SFs were used as an indication of the robustness of the material, with higher SFs predicting a more robust design, and SFs of less than one indicating a high likelihood of failure for that element. The design tool has an integrated alert system which identifies areas of the blade with unacceptably low SFs. At early stages of blade design, fatigue loads are typically unknown, and ultimate static loads are used in the design process [63]. In this case, SFs of greater than 1.3 for all elements were considered acceptable; this imposed a stress limit that was less than the composite ultimate strength to account for fatigue effects and other uncertainties, which must be considered later in the blade design process.

The two models used in this analysis were the Maximum Stress failure theory and the Tsai-Hill failure theory. The Maximum Stress failure theory predicts a laminae to fail if the compressive or tensile stresses in the longitudinal or transverse directions, or the shear stress, surpass the ultimate strength in the corresponding direction [64]. SFs in each of the material directions based on the Maximum Stress failure theory are the ratio of the ultimate strength to the stress computed by the FEM. This method of failure analysis is simple and direct but does not consider the interaction

between the stresses acting on the laminae (i.e. stresses in each material direction are considered independent of whether other components of the stress tensor are present). Therefore, it tends to over predict the likelihood of failure [42].

Tsai-Hill failure is based on the failure theory of von-Mises' distortional energy yield criterion as applied to anisotropic materials [42], and proposes, for a plane stress assumption, that a laminae fails if the SF given in Eq. (6-2) is less than 1:

$$\frac{1}{\text{SF}} = \left(\frac{\sigma_1}{\sigma_{1ult}^T} \right)^2 - \frac{\sigma_1 \sigma_2}{\sigma_{1ult}^T \sigma_{2ult}^T} + \left(\frac{\sigma_2}{\sigma_{2ult}^T} \right)^2 + \left(\frac{\tau_{12}}{\tau_{12ult}} \right)^2 \quad 6-2$$

The basic form of the Tsai-Hill failure theory does not consider compression loading, and since the transverse direction of a laminate is much stronger in compression, it tends to over predict the likelihood of failure. This was corrected for by adding a condition that if the transverse stress is negative (*i.e.* compression), Eq. (6-2) was updated by replacing the tensile transverse strength, σ_{2ult}^T , with the compressive transverse strength, σ_{2ult}^C .

7 CASE STUDY- 4 M BT BLADES

The FEM-BEMT design tool was used to perform a case study for a full-scale 10.4 m diameter hypothetical three-bladed turbine with 4 m passively adaptive BT composite blades. The total blade length was scaled linearly to 4 m with a hub radius of 1.0 m, with full-scale blade chord lengths scaled linearly (by a factor of 13.6986) from the values presented in Section 2.2.2. The pre-twist of the blade was adjusted slightly from the values given in Section 2.2.2, as discussed in Section 7.2.

Based on resource characteristics of the Northern Admiralty Inlet of Puget Sound [65], a cut-in flow velocity of 0.75 m/s, design (rated) flow velocity of 2.5 m/s, and extreme flow velocity of 3.25 m/s (approximately 1.5 times the design speed) were used, for an assumed hub height of approximately 30 m from the seabed. A rotational speed of 18 RPM was used to achieve the optimal TSR of 4 at design conditions, but was varied over the range of flow speeds to maintain this TSR.

At this scale, the turbine operated at Reynolds numbers ranging from 2×10^6 to 8×10^6 , and XFOIL was used to obtain airfoil section data over this range, in increments of 1×10^6 , for use in the BEMT code. A linear interpolation was performed to estimate the lift and drag coefficients at Reynolds numbers between these discrete curves. In XFOIL, the user-specified parameter NCRIT mimics the effects of free-stream disturbances, such as turbulence, on BL transition [57]. An NCRIT value of 9 is typically used for average wind tunnel conditions, and values of 4 to 8 for more turbulent wind tunnels. For the full-scale device assumed to be operating in a turbulent environment, an NCRIT value of 5 was used.

7.1 Blade element convergence study

Figure 7-1 shows the results of a blade element convergence study for the 4 m NREL S814 blades.

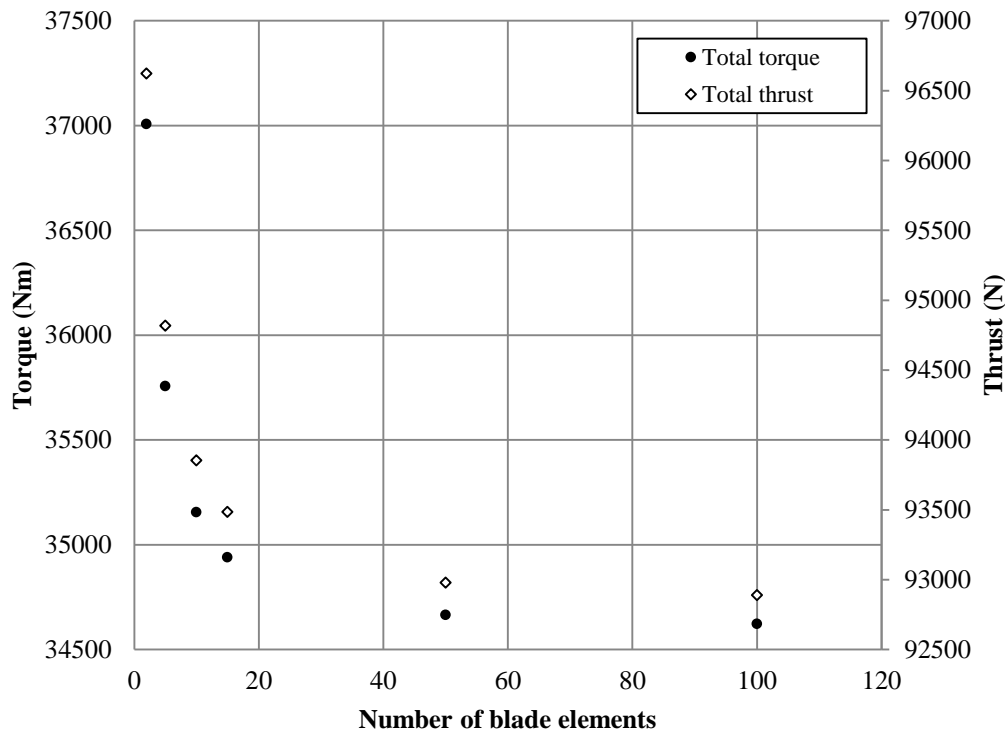


Figure 7-1 Blade element convergence for 4 m blade

For the 4 m blade, there is less than 4% difference between using 2 elements and using 100, and less than 1% difference between using 10 elements and 100 elements, which is within the normal measurement error. However, the trend clearly shows better convergence with increasing element numbers. In order to minimize computational time, 10 blade elements were used in the BEMT.

7.2 Pre-deformed blade geometry

With BT coupling alone, there was a reduction in torque (and hence power capture) at design conditions. To improve the blade performance (increase torque and power capture) at design conditions, a pre-deformed (pre-twisted) blade shape was investigated.

The pre-deformed BT blade was obtained by fine-tuning the pre-twist geometry (twist distribution along the span of an unloaded blade) of the baseline, and was designed to twist to the optimum shape at design conditions while mitigating loads and capping power at flow speeds above design conditions. The design criteria were:

$$\left. \begin{array}{l} \text{for } \text{TSR} < \text{TSR}_{\text{design}} \quad C_{p,d} > C_{p,o} \\ \text{for } \text{TSR} = \text{TSR}_{\text{design}} \quad C_{p,d} = C_{p,o} \\ \text{for } \text{TSR} > \text{TSR}_{\text{design}} \quad C_{p,d} < C_{p,o} \quad \& \quad C_{T,d} < C_{T,o} \end{array} \right\} \quad 7-1$$

where $C_{p,0}$ is the power conversion efficiency (power coefficient) and $C_{T,0}$ is the thrust coefficient of the original un-deformed blade geometry, prior to the influence of BT coupling. $C_{p,d}$ and $C_{T,d}$ are the power coefficient and thrust coefficient, respectively, of the converged deformed blade from the iterative FEM-BEMT process. Figure 7-2 shows the airfoil cross section at the tip of the blade for a rigid blade, BT blade, and pre-deformed BT blade for a range of loading scenarios.


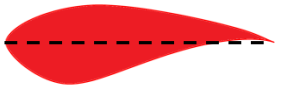
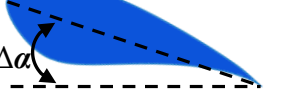





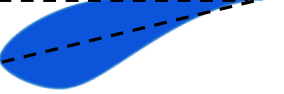
	Rigid blade	BT blade	Pre-twisted BT blade
Unloaded			
Design conditions			
Extreme conditions			

Figure 7-2 Schematic of rigid blade (black), BT blade (red), and pre-deformed BT blade (blue), The * denotes the optimum α for design conditions

where $C_{p,original}$ is the power coefficient of the original un-deformed blade geometry prior to the influence of BT coupling, and $C_{p,deformed}$ is the power coefficient of the converged deformed blade from the iterative FEM-BEMT process. The original pre-twist of the un-deformed blade is given by $\beta_{original}$, and the induced twist from BT coupling is given by $\phi_{induced}$. The new pre-twist blade geometry after it has been altered is given by $\beta_{new} = \beta_{original} - \beta_{change}$, where $\beta_{change} = \phi_{induced} + \phi_{change}$. For the first iteration, ϕ_{change} is equal to zero so that the blade is pre-deformed toward stall by the amount that it was predicted to feather by from BT coupling, so that it twists back toward the original blade shape with BT coupling. β_{change} is iterated for until the new blade pre-twist geometry, β_{new} , results in $C_{p,deformed} = C_{p,original}$ including the effect of BT coupling, at design conditions. Figure 7-3 shows a flow chart of this iterative process.

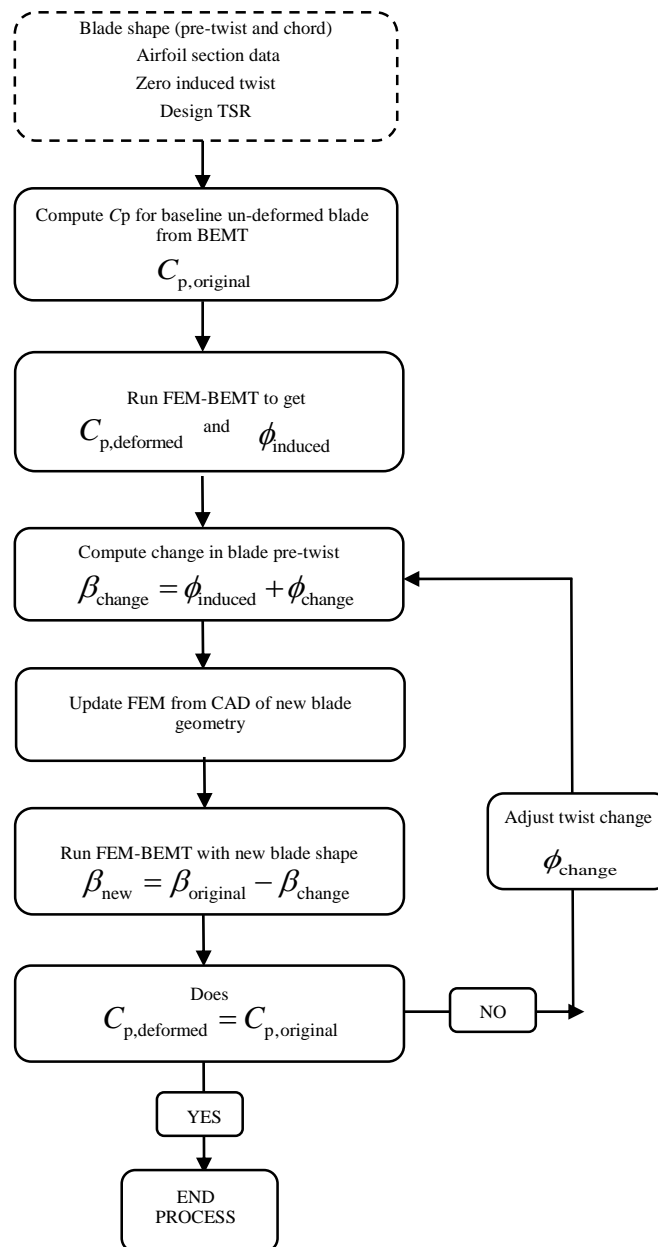


Figure 7-3 Flow chart for pre-deformed blade optimization

To do this, an iterative loop was included outside the induced twist loop of the design tool, to increase the pre-twist of the original blade incrementally after every iteration until the power coefficient of the un-deformed blade was obtained for the deformed BT blade at design conditions.

Initially this was done without updating the structural component of the FEM-BEMT tool, so that only the load changes were considered due to the change in the original blade shape. However, an additional step was included to re-create the structural FEM and re-mesh the blade to also consider

the slight change in pre-twist angle of the blade geometry. The final pre-twisted geometry of the 4 m blade compared to the original geometry is given in Figure 7-4.

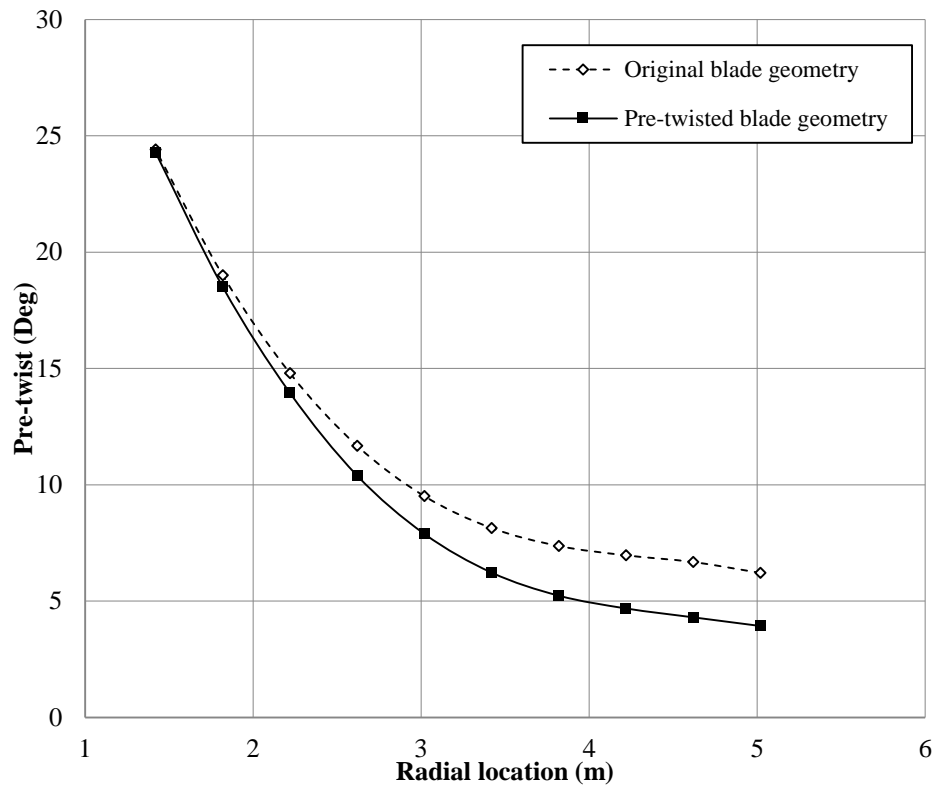


Figure 7-4 Original and pre-deformed blade pre-twist geometry.

The resulting pre-deformed geometry had slightly more pre-twist compared to the original blade shape, but twisted to the original shape upon loading due to BT coupling.

7.3 Design of experiment

Initial results of an analytical study indicated ply angles of 30° optimized the BT response of a laminate plate. However, to inform more detailed composite material design for the case-study blades, a design of experiment and optimization analysis was performed on the 4 m NREL S814 blades. The induced twist and stresses were used as criteria for material selection, and the ply thickness and layup were investigated in a design of experimental study. The design of experiment analysis investigated the full design space and found local minima and maxima in the composite design.

The angle of the off-axis plies was chosen to maximize the induced twist of the blade and constrain the composite stresses to uphold a minimum safety factor of 1.3. For a 15 mm thick composite skin, Figure 7-5 shows the induced twist and bending displacement at the blade tip for various ply angles (with 0° being oriented along the blade length). Figure 7-6 shows the associated minimum SFs in the transverse tensile and shear material directions based on the Maximum Stress failure

theory. The thrust and tangential loads applied in the FEM were determined by BEMT at design conditions of 2.5 m/s and 18 RPM.

From Figure 7-5, the bending displacement increased with increasing ply angle. Although the induced twist in the blade reached a maximum at a ply angle of 35°, the transverse tensile SF shown in Figure 7-6 continued to decrease with increasing ply angles. Correspondingly, the SFs in the longitudinal material direction were found to increase with increasing ply angle. As the blade undergoes flap-wise bending, the pressure surface of the blade skin was generally in tension, while the suction surface was in compression. For highly angled plies, as the blade bends, less of the tensile load on the pressure surface of the blade skin is carried by the fibers and more of the load is carried by the matrix material. The matrix material is significantly weaker than the fibers, particularly in tension, giving the composite material a lower ultimate strength in the transverse direction. For ply angles greater than 60°, the SF in the shear direction increased slightly with increasing ply angles. For large ply angles, the induced twist from BT coupling decreased, reducing the shear stress in the composite material and hence increasing the SF.

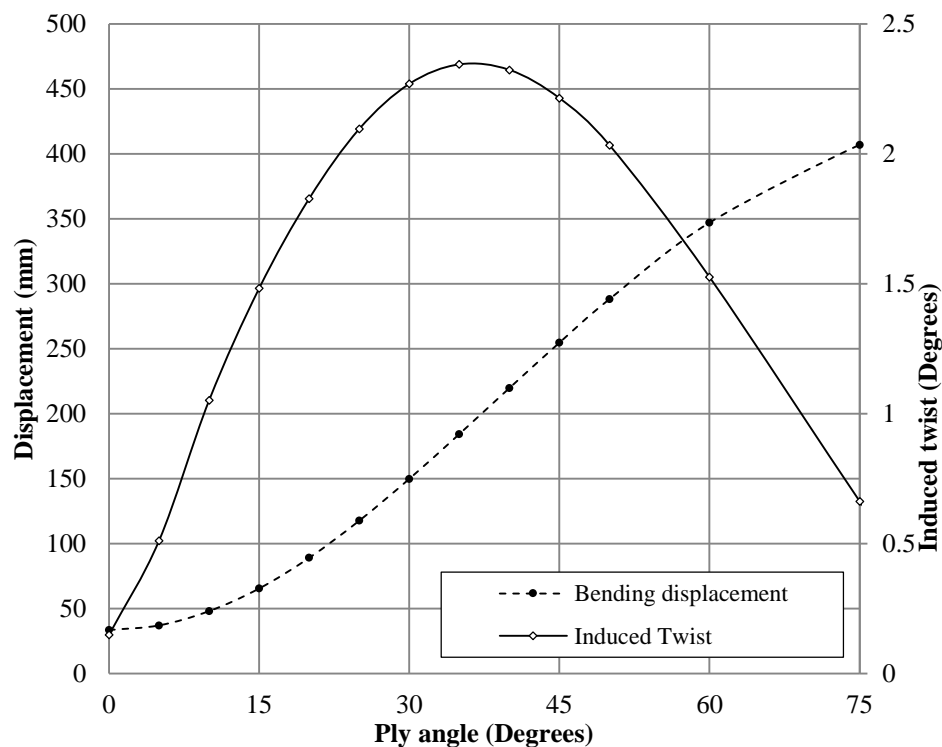


Figure 7-5 Induced tip twist and tip bending displacement of blade as a function of ply angle.

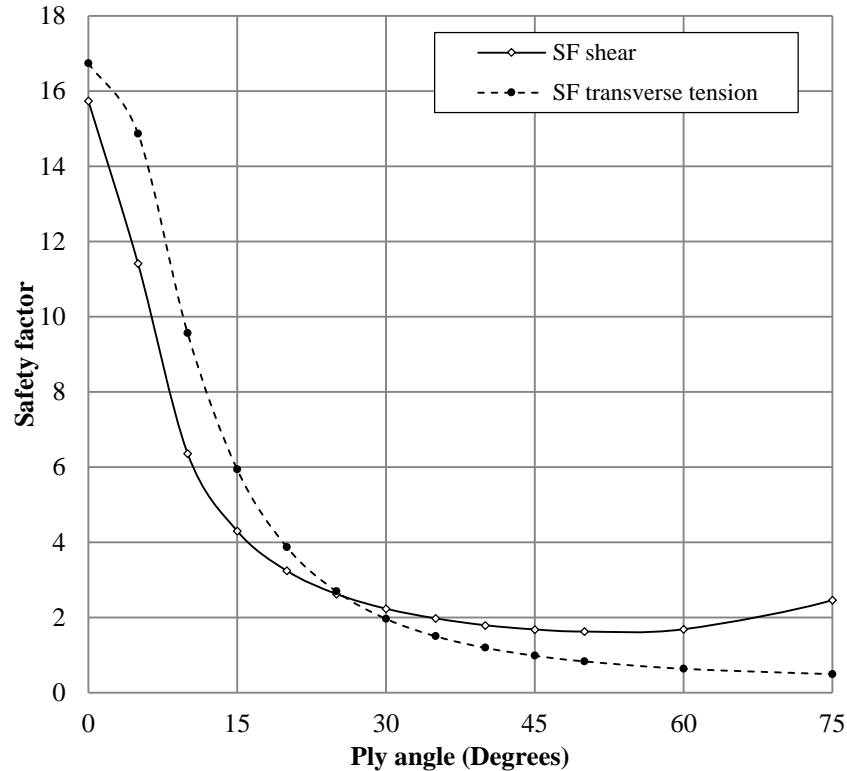


Figure 7-6 Material safety factors in the transverse tensile and shear directions as a function of ply angle.

For a ply angle of 35° and uniform composite skin thickness of 15 mm, at design conditions, the design tool predicted a SF of 1.5 in the transverse tensile direction and 2 in the shear direction.

An extreme flow velocity of 3.25 m/s (approximately 1.5 times the design speed) was used to approximate the extreme load case. The maximum transverse tensile stress in the composite blade was 4.67×10^{-2} GPa, which, compared to an ultimate transverse tensile strength of 4.0×10^{-2} GPa, gives a SF of 0.86 in the transverse tensile direction. At extreme flow conditions, for a ply angle of 35° , this blade design had 2.34° of tip twist and a 6.44% reduction in thrust loads from BT coupling. Based on the failure theories applied, it is expected that this design would not survive extreme conditions. The composite material was particularly highly stressed at the root of the blade.

To obtain a more robust design, the composite thickness needed to be increased. For an optimized and cost effective design, material costs can be reduced by tapering the composite thickness toward the blade tip using ply drops. However, although the maximum stress in a tapered composite blade design is lower, stress concentrations arise from the ply drops. Further designs improvements will be aimed at smoothing these drops, increasing the SFs, and increasing the induced twist for improved BT performance. However, for this investigation a constant composite thickness was used. The final composite layup is given in the following section.

7.4 FEM development

In the FEM, the blade skin was constructed of uniform 25 mm thick unidirectional graphite epoxy composite with 35° off-axis plies to induce BT coupling. Closed-cell foam was used to fill the blade for buoyancy, to prevent flooding, and for ease of manufacturing. Material properties are given in Section 0. Based on the result of a mesh convergence study, 30 mm tetrahedral 3D elements were used to mesh the blade core, and 30 mm 2D shell elements were used to model the composite skin of the blade. For a conservative design, it was assumed that the blade skin carried the full load and that additional layers such as a gelcoat would not be load-bearing and were not considered in the model. This no-spar design is aligned with the one-shot resin transfer molded manufacturing process which is currently being used in the industry [66]. The blade root, including attachments such as bolts and inserts, was not considered in the model at this time.

7.5 Results

Figure 7-7 and Figure 7-8 show the thrust and power coefficients (C_p and C_t , respectively), and Figure 7-9 shows the transverse tensile and shear SFs, for both the pre-twisted and original blade shapes with BT coupling. The initial C_p was predicted by BEMT for the un-deformed blade, and the final C_p was predicted by the iterative FEM-BEMT tool for the converged deformed blade.

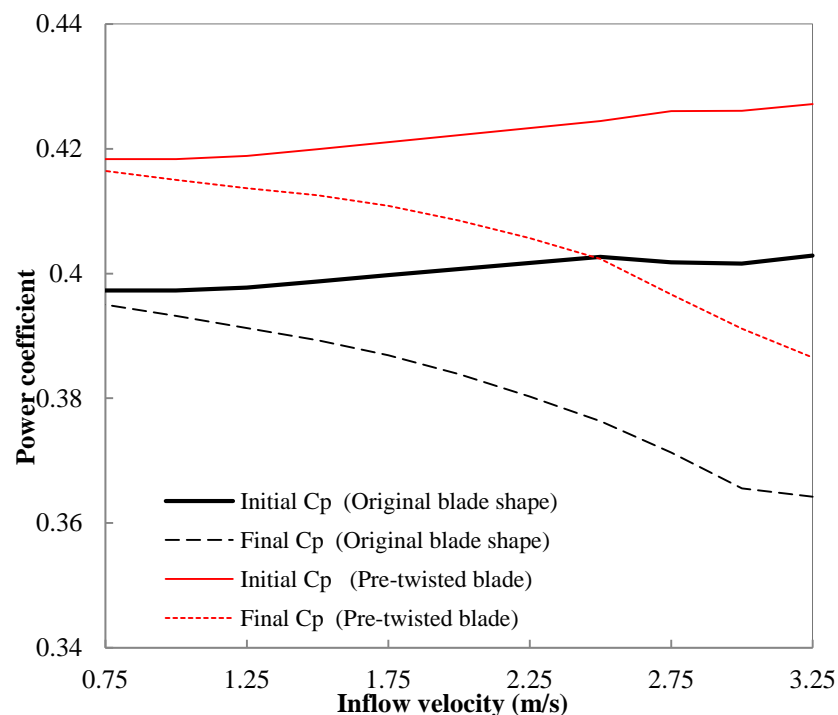


Figure 7-7 Power coefficient for pre-twisted and original blade shape.

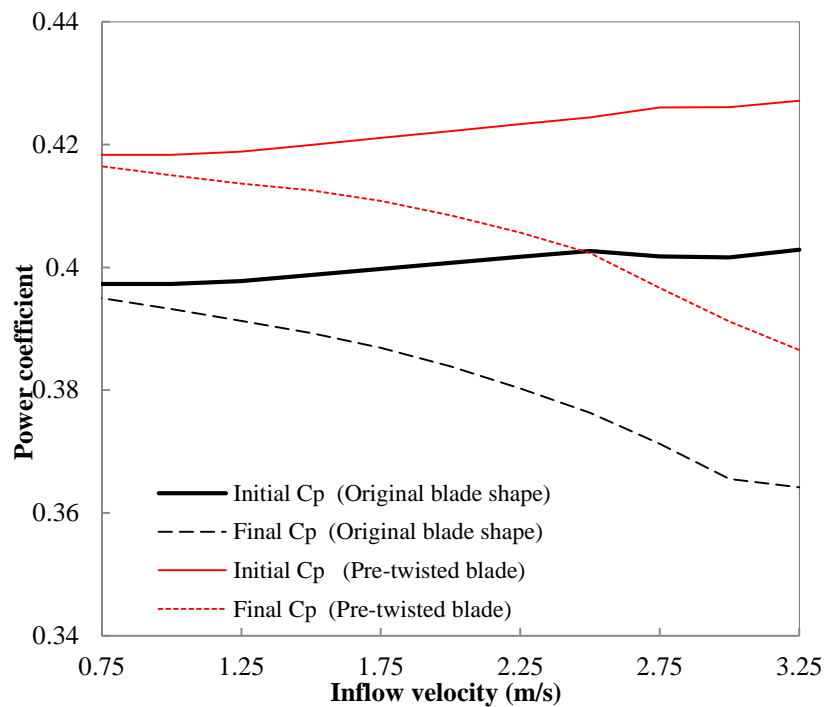


Figure 7-8 Power coefficient for pre-twisted and original blade shape.

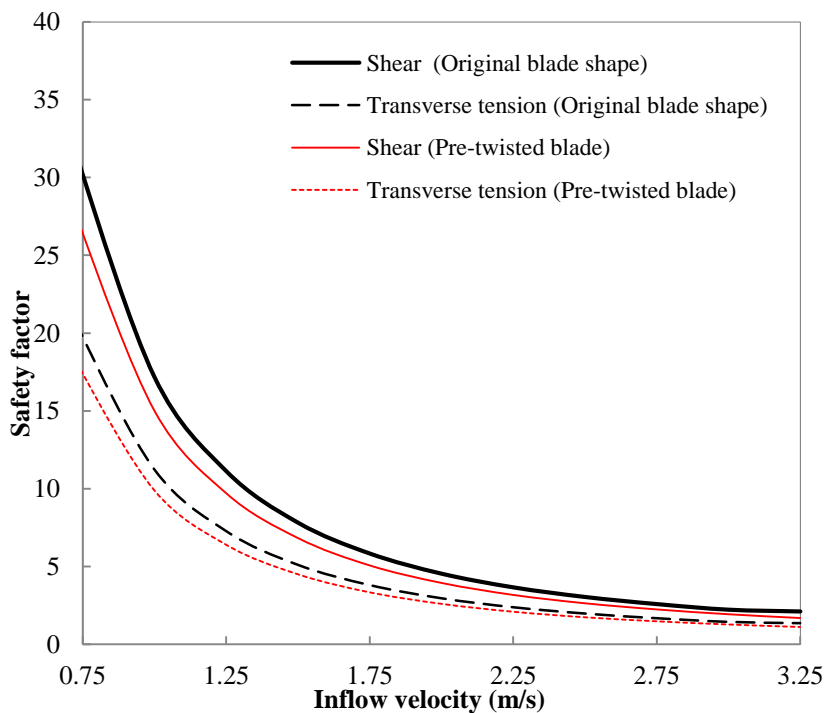


Figure 7-9 SFs for original and pre-twisted blades with BT coupling.

Using variable speed control, at design conditions of 2.5 m/s, the pre-twisted deformed (final-light dashed line) blade had close to the same power and thrust coefficients as the original undeformed blade (initial-thick solid line). However, at the maximum flow speed of 3.25 m/s, the pre-twisted deformed blade (final-light dashed line) had a 4.1% reduction in power and 7% reduction in thrust loads from the original blade shape (initial-thick solid line), with 3.72° of induced twist at the tip of the blade. As well, at the cut-in-speed of 0.75 m/s, there was a 4.9% increase in power capture, with an associated 10.1% increase in thrust loads. The thrust loads at this low flow speed were significantly smaller than at design conditions, so this percentage increase in thrust is not significant. However, this means more power is captured in the operational range of flow conditions of the turbine.

From Figure 7-9, for the pre-twisted blade shape at design conditions, the design tool predicted a SF of 1.73 in the transverse tensile direction and 2.64 in the shear direction, indicating an acceptable level of confidence in the composite design. However, at extreme conditions, there was a SF of 1.12 in the transverse tensile direction and 1.69 in the shear direction. Based on the failure theories discussed, this design is at risk of failure at extreme conditions.

To obtain a more robust design, material can be added to the blade root where the composite is highly stressed. For an optimized and cost effective design, material costs can be reduced by tapering the composite thickness toward the blade tip using ply drops. This will also increase the induced twist at the blade tip, resulting in more load mitigation at high flow speeds. Further development of this full scale blade design will include ply drops aimed at increasing induced twisting, load mitigation and composite SFs.

8 CONCLUSIONS

The purpose of this continued research was to determine the applicability of BT coupling of tidal turbine blades to the industry. This work has demonstrated the sensitivity of composite FEMs to manufacturing effects such as ply angles and thicknesses. Through structural testing of BT blades, it was shown that for thin laminates, the FEM requires a high level of accuracy for the thickness as well as the ply angles. At this point, smaller scale blades with thin ply layers are being used to demonstrate and prove the BT concept. Therefore, at this stage of the research the thickness and ply angles need to be accurately known. However, for larger-scale blades the relative effect of thickness will become less important.

The iterative FEM-BEMT design tool was shown to be effective in predicting the deformation and performance of a BT blade in a short computational time, making it useful for early stage design engineering where many design iterations are trialled. Based on a case study for a full scale turbine with BT blades, it was found that designing a BT blade with a pre-deformed geometry allows the turbine to operate optimally at design conditions, while reducing structural loads and power capture at flow speeds above design conditions. As well, a pre-deformed blade increases the overall power capture of the turbine between the cut-in flow speed and the design flow speed, increasing the overall annual energy capture. This increase in power within these flow conditions, as well as the decrease in structural loads, has significant effects on the overall cost of the turbine. For example, with lower peak power and thrust loads at extreme conditions, smaller, less expensive generators and support structures will be sufficient. As well, for existing turbine systems, BT blades can be lengthened without altering or increasing the existing support structure size, resulting in increased power capture.

8.1 Future work: Composite and Aluminum blades hydrodynamic testing

Composite and aluminum blades of the same geometry are going to be tested in the towing tank at Strathclyde University. The turbine will be set up in the Strathclyde towing tank similarly to test set 1, shown in Figure 3-2. The blade geometry, materials and composite layup of the composite blades are outlined in Section 2.2.1. Test results from these tests will be used for verification of the FSI design tool and also to prove the concept of BT adaptive blades by comparing their performance direction to rigid blades.

8.2 Acknowledgments

Thank you to OERA, UK SI, UK SDI and NSERC for funding this research, and Katie Gracie and Cameron Johnstone for their support in the Dalhousie-Strathclyde collaborative research. Thank you also to Airborne Composites for making high quality test samples and for their continued support of this project. Thank you as well to the team at the Kelvin Hydrodynamics at the

University of Strathclyde towing tank for their support during our dynamic testing, and thank you to the technical staff at Dalhousie University for their continued support and assistance.

REFERENCES

1. Province of Nova Scotia. *Renewable electricity regulations-renewable electricity standard 2020*. 2011; Available from: http://www.novascotia.ca/just/regulations/regs/electrenew.htm#TOC2_7.
2. Oera Offshore Energy Research Association of Nova Scotia. *Building a tidal energy industry in canada offers substantial opportunity according to study*. 2015; Available from: <http://www.oera.ca/OEER/StrategicEnvironmentalAssessment/BackgroundreportfortheFundyTidalEnergySEA/tabid/280/Default.aspx>
3. Junqiang Xia, *et al.*, *Estimation of annual energy output from a tidal barrage using two different methods*. Applied Energy, 2012. **93**: p. 327-336.
4. Ahmad Etemadi, *et al.*, *Electricity generation by the tidal barrages*. Energy Procedia, 2011. **12**: p. 928-935.
5. Julie Houde, *Cost-benefit analysis of tidal energy generation in nova scotia: A scenario for a tidal farm with 300mw of installed capacity in the minas passage in 2020*, in *Development Economics 2012*, Dalhousie University.
6. Miles Willis, *et al.*, *Tidal turbine deployment in the bristol channel: A case study*. Proceedings of the ICE - Energy, 2010. **163**(3): p. 93-105.
7. T. M. Delorm, D. Zappala, and P. J. Tavner, *Tidal stream device reliability comparison models*. Proceedings of the Institution of Mechanical Engineers, Part O: Journal of Risk and Reliability, 2011. **226**(1): p. 6-17.
8. Jeremy Thake, *Development, installation and testing of a large scale tidal current turbine*, C.I. Power, Editor 2005.
9. Province of Nova Scotia. *Developmental tidal feed-in tariff program*. 2015 Oct 29, 2015]; Available from: <http://energy.novascotia.ca/renewables/programs-and-projects/tidal-fit>.
10. Pengfei Liu and Brian Veitch, *Design and optimization for strength and integrity of tidal turbine rotor blades*. Energy, 2012. **46**: p. 393-404.
11. George Marsh, *Wave and tidal power – an emerging new market for composites*. Reinforced Plastics, 2009. **53**(5): p. 20-24.
12. J. King and T. Tryfonas. *Tidal stream power technology – state of the art*. in *Proc. Oceans*. 2009. Bremen.
13. *Failed tidal turbine explained at symposium*. CBC News [Online] 2014; Available from: <http://www.cbc.ca/news/canada/nova-scotia/failed-tidal-turbine-explained-at-symposium-1.1075510>.
14. Kittridge D Fowler M, Pemberton M, Litchfield, *Tidal turbine hub-blade connection design*, 2011: University of Maine.
15. Daniel Kittridge, *et al.*, *Computer modeling and analysis of tidal turbine hub-blade designs*, in *Project report 2009*: Crosby Laboratory, The University of Maine.
16. Dan White, *Tidal systems challenge - blade design!*, in *Ocean News & Technology* 2011. p. 38-39.
17. Marine Current Turbines. *Delay in commissioning one of seagen's rotors*. [Online] July 22, 2008; Available from: http://www.marineturbines.com/3/news/article/11/delay_in_commissioning_one_of_seagen_s_rotors.
18. Alberto Aliseda Danny Sale, Michael Motley, Ye Li, *Structural optimization of composite blades for wind and hydrokinetic turbines*, in *Global Marine Renewable Energy Conference* 2013.
19. Carbon Trust, *Tidal streams and tidal stream energy device design*, ?
20. Pradeep Suman Sujeet Swami, Dharmendra Kumar Jain, *Performance of pitch and stall regulated tidal stream turbines*. Int. Journal of Engineering Research and Applications, 2014. **4**(4): p. 50-53.
21. Peter J. Schubel and Richard J. Crossley, *Wind turbine blade design*. Energies, 2012. **5**(12): p. 3425-3449.

22. Rachel F. Nicholls-Lee, *Adaptive composite blades for horizontal axis tidal turbines*, in *School of Engineering Sciences* 2011, Southampton.
23. Y. L. Young, *Time-dependent hydroelastic analysis of cavitating propulsors*. *Journal of Fluids and Structures*, 2007. **23**(2): p. 269-295.
24. H.J.T. Kooijman, *Bending-torsion coupling of a wind turbine rotor blade*, T.D. Faculty of Aerospace Engineering, Editor 1996.
25. W. M. J. Batten, *et al.*, *The prediction of the hydrodynamic performance of marine current turbines*. *Renewable Energy*, 2008. **33**(5): p. 1085-1096.
26. John Callaghan and Richard Boud, *Future marine energy -results of the marine energy challenge: Cost competitiveness and growth of wave and tidal stream energy*, C. Trust and E.U. Ltd., Editors. 2007.
27. Wei Shi, *et al.*, *Feasibility study of offshore wind turbine substructures for southwest offshore wind farm project in korea*. *Renewable Energy*, 2015. **74**: p. 406-413.
28. Mark Capellaro, *Design challenges for bend-twist coupled blades for wind turbines: And application to standard blades*, <http://energy.sandia.gov/wp/wp-content/gallery/uploads/2B-B-1-Capellaro.pdf>, Editor 2012: University Stuttgart.
29. Schottel, *Schottel tidal generator- scalable power from currents stg – schottel tidal generator*, 2013.
30. Michael R. Motley and Ramona B. Barber, *Passive control of marine hydrokinetic turbine blades*. *Composite Structures*, 2014. **110**: p. 133-139.
31. S. Gowing, Coffin, P., and Dai, C. . *Hydrofoil cavitation improvements with elastically coupled composite materials*. in *25th American Towing Tank Conference*. 1998. Iowa City, USA.
32. Ramona B. Barber and Michael R. Motley. *A numerical study of the effect of passive control on cavitation for marine hydrokinetic turbines*. in *EWTEC*. 2015. Nantes, France.
33. Alireza Maheri, *et al.*, *Wtab, a computer program for predicting the performance of horizontal axis wind turbines with adaptive blades*. *Renewable Energy*, 2006. **31**(11): p. 1673-1685.
34. International Towing Tank Conference -Specialist Committee on Uncertainty Analysis, *Recommended procedures and guidelines uncertainty analysis and instrument calibration*, 2008.
35. R. E. Murray, D. A. Doman, and M. J. Pegg, *Finite element modeling and effects of material uncertainties in a composite laminate with bend-twist coupling*. *Composite Structures*, 2015. **121**: p. 362-376.
36. Zoltek, *Panex® 35 uni-directional fabrics*.
37. Gurit, *Prime™ 27 epoxy infusion system*.
38. Andrew Makeev and Erian Armanios, *On a higher order analysis of laminated composite strips with extension-twist coupling*. *International Journal of Solids and Structures*, 1999. **36**: p. 970-987.
39. J.A. Clarke, *et al.*, *Equimar deliverable 3.2 concept appraisal and tank testing practices for 1st stage prototype devices*, in *Equitable Testing and Evaluation of Marine Energy Extraction Devices in terms of Performance, Cost and Environmental Impact* 2009.
40. Sicomin, *Sicomin foaming epoxy: Pb 170, pb 250, pb 400, pb 600 cellular epoxy foam production system*, 2009.
41. N. Karaolis, P. Mussgrove, and G. Jeronimidis. *Active and passive aeroelastic power control using asymmetric fibre reinforced laminates for wind turbine blades*. in *10th British Wind Energy Conference*. 1988. London, U.K.
42. Autar K. Kaw, *Mechanics of composite materials*. Second ed, ed. T.F. Group. 2006: CRC Press Taylor & Francis Group.
43. *Torayca t1700s data sheet*.
44. B. Gaurier, *et al.*, *Tidal energy “round robin” tests comparisons between towing tank and circulating tank results*. *International Journal of Marine Energy*, 2015.

45. T. McCombes, *et al.*, *Equimar deliverable 3.4 best practice for tank testing of small marine energy devices*, in *Equitable Testing and Evaluation of Marine Energy Extraction Devices in terms of Performance, Cost and Environmental Impact* 2010.
46. Tony Burton, *et al.*, *Wind energy handbook*. 2001, The Atrium, Southern Gate, Chichester, West Sussex PO 19 8SQ, England: JOHN WILEY & SONS, LTD.
47. Altair Engineering, *Altair radioss 12.0 user guide*, 2013.
48. B. Song, W. Chen, and W. Y. Lu, *Compressive mechanical response of a low-density epoxy foam at various strain rates*. *Journal of Materials Science*, 2007. **42**(17): p. 7502-7507.
49. Dan Zenkert and Magnus Burman, *Tension, compression and shear fatigue of a closed cell polymer foam*. *Composites Science and Technology*, 2009. **69**(6): p. 785-792.
50. M. V. Alonso, M. L. Auad, and S. Nutt, *Short-fiber-reinforced epoxy foams*. *Composites Part A: Applied Science and Manufacturing*, 2006. **37**(11): p. 1952-1960.
51. Marcus Andersson and Petter Liedberg, *Crash behavior of composite structures: A case benchmarking study*, in *Applied Mechanics* 2014, Division of Material and Computational Mechanics, Chalmers University of Technology.
52. Asm International, *Metals handbook - properties and selection: Nonferrous alloys and special-purpose materials*, 1990.
53. Thomas Nevalainen, Cameron Johnstone, and Andrew Grant. *Characterising unsteady eccentric loads on tidal stream turbines using a dynamic blade element momentum theory*. in *EWTEC*. 2015. Nantes, France.
54. I. Masters and J a C Orme, *A robust blade element momentum theory model for tidal stream turbines including tip and hub loss corrections*. *Marine Engineering and Technology*, 2011. **10**(1): p. 25–36.
55. Benoît Gaurier, *et al.*, *Flume tank characterization of marine current turbine blade behaviour under current and wave loading*. *Renewable Energy*, 2013. **59**: p. 1-12.
56. A. S. Bahaj, *et al.*, *Power and thrust measurements of marine current turbines under various hydrodynamic flow conditions in a cavitation tunnel and a towing tank*. *Renewable Energy*, 2007. **32**(3): p. 407-426.
57. Mark Drela, *Xfoil 6.94 user guide*, 2001.
58. A. S. Bahaj, W. M. J. Batten, and G. Mccann, *Experimental verifications of numerical predictions for the hydrodynamic performance of horizontal axis marine current turbines*. *Renewable Energy*, 2007. **32**(15): p. 2479-2490.
59. M. Togneri, *et al.*, *Flume measurements of lift and drag for selected tidal turbine blade sections*. Under review., 2015.
60. W. M. J. Batten, *et al.*, *Experimentally validated numerical method for the hydrodynamic design of horizontal axis tidal turbines*. *Ocean Engineering*, 2007. **34**(7): p. 1013-1020.
61. A.S. Bahaj G. Germain, C.Huxley-Reynard, P.Roberts. *Facilities for marine current energy converter characterization*. in *7th EWTEC*. 2007. Portugal.
62. David Verelst, *Flexible wind turbine blades: A fem-bem coupled model approach*, 2009, Delft University of Technology
63. G.S. Bir, M.J. Lawson, and Y. Li. *Structural design of a horizontal-axis tidal current turbine composite blade*. in *ASME 30th International Conference on Ocean, Offshore, and Arctic Engineering*. 2011.
64. Isaac M. Daniel and Ori Ishai, *Engineering mechanics of composite materials* 1994: Oxford University Press.
65. B. Polagye and J. Thomson, *Tidal energy resource characterization: Methodology and field study in admiralty inlet, puget sound, wa (USA)*. *Proceedings of the Institution of Mechanical Engineers, Part A: Journal of Power and Energy*, 2013. **227**(3): p. 352-367.
66. Airborne Marine, *Nautricity goes emec with airborne marine tidal blades*, 2013.

